Investigating the Early Universe with Lyman-alpha Emission: Galactic Winds and Stellar Populations at $z \sim 3.1$

by

Emily McLinden

A Dissertation Presented in Partial Fulfillment
of the Requirement for the Degree
Doctor of Philosophy

Approved June 2012 by the
Graduate Supervisory Committee:

James Rhoads, Chair
Sangeeta Malhotra
Frank Timmes
Paul Scowen
Patrick Young

ARIZONA STATE UNIVERSITY

August 2012

ABSTRACT

Lyman-alpha (Lyα) galaxies (LAEs) and Lyα blobs (LABs) are objects identified and studied due to their bright Lyα emission lines. This bright emission allows LAEs and LABs to be studied in the distant universe, providing a glimpse into the physical processes occuring in the early universe. This dissertation presents three complementary studies of LAEs and LABs at $z \sim 3.1$. The two main foci of this work are (1) to understand the gas kinematics in both classes of objects and (2) to improve spectral energy distribution (SED) fitting processes to better determine the physical characteristics of LAEs. Gas kinematics in this dissertation means looking for signatures of large-scale winds. This is an exciting astrophysical endeavor, because the results can provide insight into how Lyα photons escape distant galaxies and traverse the IGM, and the results have implications for how the epoch of reionization can be studied with the Lyα line and because winds can be a signature of powerful star formation events. In the first two studies we find signatures of winds in three LAEs by measuring the velocity offset between the redshifts of [O III] and Lyα in these galaxies. The first two LAEs presented here represent the first ever measurements of [O III] in Lyα-selected field galaxies. The third study reports no velocity offset between [O III] and Lyα when the methodology is transferred to a $z \sim 3.1$ LAB. This lack of velocity offset is an interesting result, however, as powerful outflows and star formation events, which should impart a velocity offset, have been hypothesized as power sources for LABs. In addition to understanding the kinematics of these objects, we introduce a new parameter into the SED fitting process typically used to characterize LAEs. This new parameter enables better determination of characteristics like the age, mass, metallicity, dust content and star formation history of the galaxies in our sample.

These characteristics provide a snapshot of galaxies in the universe $\sim$ 11 billion years ago and also provide insight into how these characteristics compare to galaxies at other epochs.

DEDICATION

I dedicate this to my dad, the first Dr. McLinden, whose simple question helped me take the leap into physics. Thanks for the trips to Fermilab, your support and excitement, and the burritos as big as your head.

ACKNOWLEDGEMENTS

I have to start by thanking my parents. You've provided unbelievable support for me to be able to get here. My words can't quite express what I want - but thanks for always telling me I could be whatever I wanted to be and go wherever I wanted to go. From ballerina to astrophysicist, I've always known I had your full support. Thanks to my brothers for hugs, beers, support, love, laughs, and for always making me feel like you were proud of your little sister. I could not do it without you guys.

A really important acknowledgement goes to my advisor, James Rhoads, as well as Sangeeta Malhotra. Thank you for the opportunity to work on this project in the first place. Thank you for your help with all my work, proposals, papers, conferences, job searching, and much more. Thanks for supporting me, but also for challenging and pushing me.

Thanks to the rest of my committee, Frank Timmes, Paul Scowen, and Patrick Young for your time and input. Paul, thanks for your always encouraging words and for your job search help. Frank, thanks for your support on my secondary project and some conversations that were really important to me.

And thanks to my amazing friends that have supported beyond my wildest imagination during my time in AZ. Thanks Katie, Robert, Rosa, Marci, Kate, Cat, Hwi, Seth, Matt, Michael, Alka, Alex, Tray and my marriage equality people. I know I've surely forgotten someone crucial, but I hope all of you know how much you mean to me and I hope you know how much I appreciate your support and how certain I am I couldn't have done it without. Thanks for science discussions, discussions on anything but science, adventures and for becoming my family here. I never new I would get to have friends as amazing as this. Thanks y'all!

TABLE OF CONTENTS

CHAPTER Page

CHAPTER Page

CHAPTER Page

CHAPTER Page

LIST OF TABLES

LIST OF FIGURES

Figure Page

Chapter 1

INTRODUCTION

1.1 What is Lyman-alpha Emission?

Lyman-alpha (Lyα) is an emission line of hydrogen. It is also an invaluable tool for probing galaxies in the early universe. A Lyman-alpha photon is produced when an electron falls from an excited state (n=2) to the ground state (n=1) in a hydrogen atom. The difference in energy between those two states produces a photon whose wavelength (λ) is 1215.67 Å (vacuum). Photons like these are produced in the presence of young, hot, massive stars (O and B-type stars) that are surrounded by spheres of ionized hydrogen, and further out, neutral hydrogen. When a photon emitted by a star strikes a neutral hydrogen atom, if the energy of the photon is greater than 13.6 eV (or $\lambda \leq 912$ Å), the photon will ionize the hydrogen atom and expel an electron from the atom. In the region where this ionization is occurring, free electrons and ionized hydrogen atoms will find each other again, in a process known as recombination, and they will rejoin, once again creating a neutral hydrogen atoms. However, if the newly re-joined electron remains in an excited state, it will eventually cascade down to the ground state, emitting a photon. Two out of every three electrons that recombine will recombine to an n $\geq$ 2 state, and will produce a Lyα photon at the end of their cascade. This means that for every three ionizing photons emitted, two Lyα photons are produced. Consequently, galaxies and regions with intense star formation, where O and B-type stars are numerous, should produce large Lyα photon fluxes.

1.2 Lyα as a Probe of the Early Universe

Given the technical information above, how is all of this useful for learning about the early universe? The rest-frame wavelength of Lyα, mentioned above, is 1215.67 Å, meaning it is in the ultra-violet (UV) regime of the electromagnetic spectrum. Earth's atmosphere blocks essentially all UV light, meaning one cannot easily observe light of this wavelength from the ground. However, when Lyα photons travel to the observer across great distances from far-away galaxies, their wavelength is altered. While a Lyα photon leaves its galaxy with $\lambda = 1215.67$, when it reaches earth it will have $\lambda > 1215.67$. This is due to the fact that the wavelength stretches with the expansion of the universe. If a galaxy is sufficiently far away, the wavelength of Lyα will stretch enough to reach the optical portion of the electromagnetic spectrum ($4000 \lesssim \lambda \lesssim 10000$ Å). Light in the optical regime can easily penetrate Earth's atmosphere, so light in this regime can be studied with ground-based telescopes. This means that galaxies, whose distances from the observer will result in Lyα photons with wavelengths $4000 \lesssim \lambda \lesssim 10000$ Å, can be readily studied with ground-based telescopes. This phenomenon makes Lyα photons, an abundant marker of star forming regions in early galaxies, readily accessible when they travel to us from such distances. The lengthening, or reddening of the wavelength of light is called redshifting. Cosmological redshift, z, reveals how much a line has lengthened with respect to its rest-frame wavelength. This also shows how far away the galaxy is that produced the light and/or how far back in time (lookback time) one is looking to see that galaxy. To be precise, the actual range of redshifts one can probe from the lengthening of Lyα wavelength to the optical from ground-based telescopes is $z \sim 2.2$ to $z \sim 7$, corresponding to proper distances of $\sim 17000 - 71000$ megaparsecs (Mpc), or lookback times of 10.5

– 12.9 gigayears (Gyr) (for $H_o = 71 \mathrm{km\,s^{-1}\,Mpc^{-1}}, \Omega_M = 0.27, \Omega_{vac} = 0.73$).[1] So the simple recombination of an electron and an ionized hydrogen atom provides one with a way to collect light from and study ancient galaxies. For instance, combining preliminary detections of these Lyα photons with additional techniques like optical and near-infrared (NIR) spectroscopy allows one to understand details about the movement of gas within these galaxies, the kinds of stars present in such galaxies and much more. In addition, one can compare such results from one redshift to results at other redshifts to study the evolution of galaxies from one epoch to another and even compare them to present-day galaxies - all such topics available for study via Lyα are exciting astrophysical subjects today.

1.3 Detecting Lyman-alpha Emitting Objects

1.3.1 Lyman-alpha Emitting Galaxies

Given the abundance of hydrogen in the universe, many objects can emit Lyα. This work, however, focuses on two classes of objects identified by their Lyα emission: Lyman-alpha emitting galaxies (LAEs) and Lyman-alpha blobs (LABs). LAEs are galaxies detected by the strength of their Lyα emission - i.e. they must have very abundant Lyα emission. LAEs are typically discovered via narrowband (NB) imaging. This technique uses observations from a narrow filter ($\Delta\lambda \lesssim 100$Å) centered on the expected wavelength of Lyα, which depends on which redshift one is probing. In addition, one uses a much wider broadband filter, whose bandpass fully encompasses the narrowband. Figure 1.1 demonstrates this filter arrangement, with a narrowband filter residing in the bandbass of the broad g′ filter. This filter arrangement allows one to compare the flux an object has in the

[1] http://www.astro.ucla.edu/ wright/CosmoCalc.html

broadband to the flux it has in the narrowband, where the narrowband captures the line emission (if present) and the broadband captures the continuum emission from the galaxy. If the object has an emission line, the object should have a greater flux density in the narrowband than in the broadband. One can also include a filter blue-ward of the Lyα line for additional confirmation that the detected object is, in fact, an LAE at the desired redshift. The filter blue-ward of the Lyα line is used as a 'drop-out' filter and one expects to find less flux in this filter than in the main broadband filter, as photons with $\lambda < 1215.67$ Å are preferentially attenuated by neutral hydrogen in the intergalactic medium (IGM) between the source and the observer. One can subsequently use optical spectroscopy to confirm the presence of the Lyα line and the redshift of the objects detected via narrowband imaging.

The narrowband technique was first successful at finding LAEs at the turn of the last century, even though the existence of distant galaxies with strong Lyα lines had first been predicted in 1967 (Partridge & Peebles, 1967). A combination of initially overestimated Lyα luminosities, combined with a long wait for more sensitive detectors and larger telescopes, led to the long period between prediction and first observations of LAEs. Cowie & Hu (1998), Hu et al. (1998), and Rhoads (2000), were among the first successful surveys for LAEs. The present work uses the now routine and well-tested narrowband imaging technique to search for LAEs at z $\sim$ 3.1. To do this a narrowband filter with $\Delta\lambda = 55$ Å was centered at $\lambda = 5025$ Å. This narrowband filter therefore selects Lyα emission from $3.11 \leq$ z ≤ 3.16. A redshift of z $\sim$ 3.1 means one is looking at light from $\sim$ 2.1 Gyr after the Big Bang.

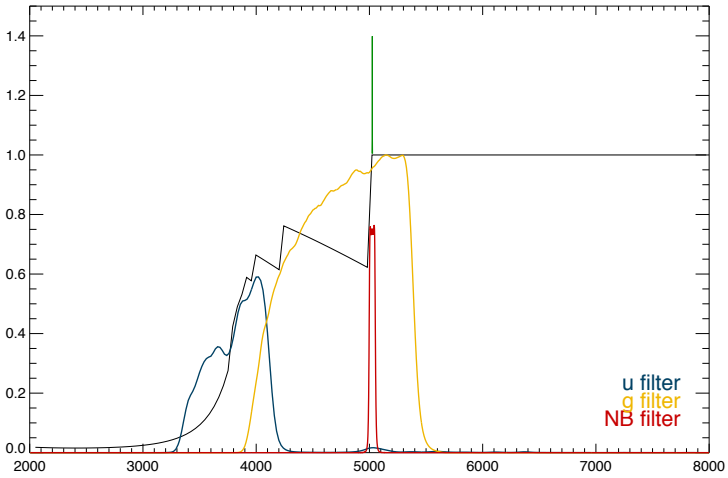

Figure 1.1 Arrangement of filters for LAE selection - blue curve is transmission curve for u^* filter, yellow is transmission curve for g' filter, red is transmission curve for [O III] narrowband filter. Green line represents the location of the Lyα emission line (not to scale) which lies within the bandpass of the narrowband filter, black curve shows how flux is transmitted through the IGM from a $z \sim 3.1$ galaxy (Madau, 1995).

1.3.2 Lyman-alpha Blobs

Lyα blobs are a related class of objects in that they too are detected via their strong Lyα flux and can also be detected via the narrowband selection process. There are, however, a number of large differences between the objects. Whereas LAEs are typically compact, star-forming galaxies, LABs are enormous, extended regions of Lyα emission. Typical sizes are 30–200 kiloparsecs (kpc). While the Lyα emission typical of LAEs is believed to be powered by intense star-formation, it is not yet known what exactly powers the large Lyα luminosity of LABs ($\sim 10^{43-44}$ ergs s^{-1}) or what leads to their expansive sizes. Further observational study, as presented in this work, may help shed light on what process(es) in the early universe created these enigmatic objects.

1.4 Outflows and the Visibility of Lyα Emission

1.4.1 Resonant scattering of Lyα photons

Lyα photons are produced in LAEs or LABs, travel great distances, and are collected at telescopes here on earth so that we might study the objects from whence they came. Unfortunately, it is not quite that straightforward. The fact that Lyα photons even escape the galaxies in which they were produced and successfully navigate the IGM to reach our telescopes is somewhat surprising. This is because Lyα photons are subject to resonant scattering by neutral hydrogen and can also be very susceptible to attenuation by dust. Resonant scattering occurs with Lyα photons because their energy (10.2 eV) matches the energy difference between the ground state and first excited state of a hydrogen atom (as discussed in Section 1.1). This means that every time a Lyα photon emitted from one hydrogen atom encounters another (unexcited) hydrogen atom, it will be readily

absorbed, sending the new atom's electron to the n=2 excited state. Given the abundance of neutral hydrogen in galaxies and the IGM, this occurs extremely frequently. The excited hydrogen atom will eventually relax to its ground state, emitting yet another Lyα photon. That photon can, however, be emitted in any direction, meaning it may scatter out of the observer's line of sight, and additionally, the frequency of the photon may be altered. The process will repeat over and over again, thereby hugely increasing the optical depth of neutral hydrogen the photon sees and altering the photon's path. This can occur both as the Lyα photon tries to escape the galaxy and when it encounters neutral hydrogen in the IGM. A simplified view of this process is presented in Figure 1.2, which shows how Lyα photons see an increased optical depth due to resonant scattering and how photons may scatter out of the line of sight. Additionally, given the increased path length from resonant scattering, Lyα photons can be vulnerable to even small amounts of dust (Neufeld, 1991; Kunth et al., 1998) since the photon will be more likely to encounter the dust during its long random walk through neutral hydrogen. This scattering of Lyα photons by neutral hydrogen can clearly reduce the amount of Lyα flux one can successfully observe from a distant source and can change the expected wavelength of the Lyα line center.

1.4.2 How Outflows Aid Lyα Escape

One mechanism that can aid the escape of Lyα photons from a galaxy and make them less susceptible to absorption and scattering in the IGM is the presence of winds. Winds are reasonable to expect in star-forming galaxies, as intense star-formation and subsequent supernovae can drive substantial winds. This phenomena has been seen in nearby starbursting galaxies (Heckman et al., 1990; Heckman, 2002).

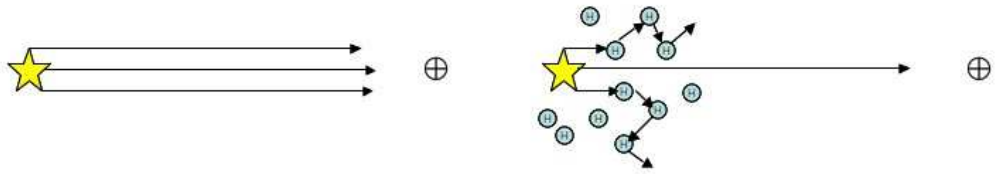

Figure 1.2 Comparison of the path of Lyα photons in the absence or presence of neutral hydrogen. In the panel at left, the path of the photons, represented by black arrows, is unaltered if the photons do not encounter neutral hydrogen - the location of the observer is represented by the small circle and cross, a source of Lyα photons is represented by the star. In the right panel, the path of the Lyα photons is diverted by resonant scattering when the photons encounter neutral hydrogen (small circles).

Winds, or outflows, are typically modeled as spherical shells of neutral hydrogen that are expanding away, with speed V, from a central source of Lyα photons. This is a simplified schematic for a real star-forming region. A real star-forming region is surrounded by a volume of gas that has been ionized by continuum photons from O and B stars (an HII region) in which Lyα photons can freely propagate. The ionized HII region is in turn surrounded by still neutral hydrogen, which is material that can be driven outward by intense star formation and supernovae. Such expanding shell models (e.g., Ahn et al., 2003; Verhamme et al., 2006; Dijkstra & Wyithe, 2010) have demonstrated how winds can help boost Lyα photons away from resonance, which eases their escape from their galaxy and aids their transmission through the IGM. Most of the photons that escape in this scenario are those photons that underwent one or more backscatterings in the portion of the shell that is receding with respect to the observer (Verhamme et al., 2006; Hansen & Oh, 2006). As such, the emergent Lyα line profile is red-

shifted with respect to the actual systemic redshift of the galaxy and the profile is asymmetric, demonstrating the favored escape of redder photons. Signatures of the wind can then be seen both in the shape of Lyα line profile itself and in an offset between the Lyα line and the systemic redshift of the source.

An outflowing neutral medium can impart Lyα photons with a frequency shift, aiding in their escape from the galaxy and their subsequent journey through the IGM. This frequency shift moves the photons away from the central resonant frequency. This is a frequency shift the photons would not get if they encountered, for instance, a surrounding static shell of neutral hydrogen instead of an expanding shell. Because the photons see the surface moving away, their interaction with the receding surfaces imparts a net redshift (Hansen & Oh, 2006).

The photons that will get the biggest frequency shift from a single interaction with the shell are those that that 'backscatter' or are reflected off the receding back side of the shell, with respect to the observer. The maximum frequency shift this interaction can impart in a single scattering event is proportional to two times the expansion velocity of the shell, depending on the angle of incidence and scattering. Those photons that get that maximum boost have the highest probability of reaching the observer because they are the furthest off resonance and see the smallest HI optical depth - so these photons build up the dominant spectral feature of Lyα emitting galaxy with an outflow - a significantly red-shifted Lyα line profile. See Figure 1.3, adapted from Verhamme et al. (2006), for a model emergent Lyα line profile from interaction with an expanding shell. Some additional photons can benefit from the moving shell, even without backscattering. These are photons that diffuse to either the red or blue wing of the Lyα line in the oncoming portion of the shell (with respect to the observer) before escape or those that sneak through the oncoming shell with no interaction - the probability

of which increases with increasing shell velocity (Verhamme et al., 2006). Clearly, if the neutral material in the galaxy is not at rest, there are multiple channels by which the material's movement can aid in shifting Lyα photons away from the line center and can improve the observer's chance of seeing the photons.

Measuring the systemic redshift of the source then becomes a crucial component in looking for signatures of winds and in understanding how Lyα escapes and reaches the observer from high-z sources. This is because one expects the redshift measured from Lyα to be altered by the interactions described above - so one needs another emission line (one that is not subject to deformation and complex radiative transfer effects as described above) from the galaxy with which to measure the systemic redshift of the system. In this work, the systemic redshift of the Lyα source is measured using [O III], or a forbidden transition of doubly ionized oxygen. [O III] is created in HII regions around ionizing stars and is not subject to resonant scattering and complicated radiative transfer effects as Lyα is - so the measured line center of the [O III] line should represent the actual systemic redshift of the star-forming region. This systemic redshift can be compared to that of Lyα - and any offset between the two redshift measurements is a signature of the presence of bulk motion or winds in the system. Comparing the redshifts of these two lines can provide insight into the kinematics of the gas in the sources and explain how Lyα photons can successfully navigate their way to the observer. This work discusses how this technique was first applied to LAEs and later used to investigate the kinematics of LABs.

1.5 Studying galaxies via Spectral Energy Distribution Fitting

In addition to learning about the gas kinematics in Lyα sources, and how this aids the visibility of Lyα, this work also aims to understand more about the

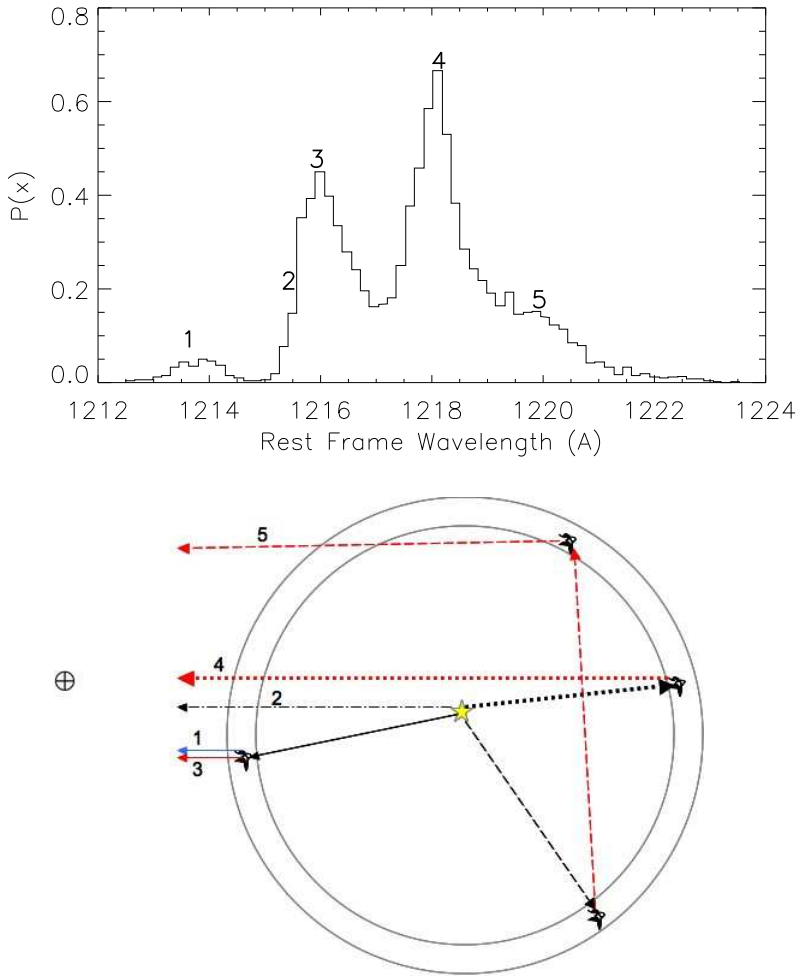

Figure 1.3 Top and bottom panel both adapted from Figure 12 of Verhamme et al. (2006) - top panel is model Lyα line profile in the presence of a shell of neutral hydrogen expanding radially outward with a constant speed (V), with each feature of interest labeled 1 – 5 - bottom panel illustrates how photons in each part of profile (features 1 – 5) are frequency shifted. In bottom panel, the color of each line after emergence from shell indicates whether photons were redshifted or blueshifted by interaction with the shell, the black line of feature 2 emerges at line center, the location of observer is indicated by the cross at left. The dominant feature of the spectrum is feature 4, composed of atoms that have backscattered once and had their original frequency (f) shifted by $\sim \frac{2V}{c}$f.

physical characteristics of LAEs at high-z. Deriving physical characteristics of the galaxies - characteristics like age, mass, metallicity (Z), dust content, and star-formation history is typically done by comparing the flux of the galaxy from a wide spectral range to the flux from model stellar populations. The model stellar populations have varying values for age, mass, metallicity (Z), dust content, and star-formation history, and the stellar population model that best fits the observed spectral energy distribution (SED) of the galaxy is considered representative of the actual physical characteristics of the galaxy.

One of the latest developments in this field has been the attention paid to how nebular emission lines, such as [O II], [O III], and Hβ can affect the ages and masses determined from SED fitting (Schaerer & de Barros, 2009). Nebular emission lines affect the mass and age determinations because the flux these lines contribute can be misinterpreted by the model fitting process as signatures of the 4000 Å/Balmer break which leads to solutions with older ages and larger masses. Schaerer & de Barros (2009) have demonstrated that not accounting for contributions from nebular emission can result in ages that are up to four times older and masses that are 1.5 times larger.

This work presents a novel and simplified way to handle contributions from nebular emission during the SED fitting process. In particular, a new fitted parameter is introduced to account for any contributions to the galaxy spectrum from the [O III] line. This allows for more accurate determination of ages and masses for the LAEs by properly attributing excess flux to a nebular emission line, instead of misinterpreting the flux as evidence for the 4000 Å/Balmer break. Adding a parameter for [O III] to the SED fitting process is a particularly exciting approach because it means the best-fit models that include this new parameter can predict the strength of the [O III] line in an LAE spectrum - a prediction that can

be tested and compared to actual [O III] line strength measurements in galaxies where [O III] has been measured (McLinden et al., 2011). Such a comparison is useful in testing the accuracy of the new approach, and it could also be used to best allocate future NIR telescope time to observe LAEs most likely to yield [O III] detections.

1.6 This Work

This work aims to understand the kinematics of Lyα emitting objects in the early universe, with a particular emphasis on understanding how Lyα escapes from these objects and how Lyα photons are able to traverse the IGM. As discussed above, outflows may provide crucial reprocessing of Lyα photons - allowing such photons to escape from the objects in which they were created and may explain how Lyα photons can traverse the IGM. The following chapters focus on looking for signatures of such outflows in LAEs and then transferring successful techniques to also study LABs. Contrasting results from LAEs and LABs provides some understanding of whether outflows are a ubiquitous characterstic of high-z Lyα sources. Chapter 2 introduces the first reported [O III] measurements from two Lyα-selected field galaxies. The velocity offsets derived from the [O III] and Lyα lines in these two LAEs are discussed, as well as the implications of the derived offsets. Chapter 3 provides a detailed overview of our entire sample of 33 LAEs - describing the narrowband survey, LAE selection techniques, and optical spectroscopic observations. An additional [O III] measurement, and subsequent [O III]-Lyα offset in one additional LAE is presented. The main focus of Chapter 3, however, is a detailed analysis of the physical characteristics of the entire LAE sample via SED fitting, including discussion of our new [O III] line fitting technique. Chapter 4 describes how we expanded our [O III] measurements and

search for wind signatures from LAEs to LABs. A review of the main results is given in Chapter 5 in addition to final conclusions.

Chapter 2

FIRST SPECTROSCOPIC MEASUREMENTS OF [O III] EMISSION FROM FIELD LYMAN-ALPHA SELECTED GALAXIES AT Z $\sim$ 3.1

2.1 Abstract

We present the first spectroscopic measurements of the [O III] 5007Å line in two z $\sim$ 3.1 Lyman-alpha emitting galaxies (LAEs) using the new near-infrared instrument LUCIFER1 on the 8.4m Large Binocular Telescope (LBT). We also describe the optical imaging and spectroscopic observations used to identify these Lyα emitting galaxies. Using the [O III] line we have measured accurate systemic redshifts for these two galaxies, and discovered a velocity offset between the [O III] and Ly-α lines in both, with the Lyα line peaking 342 and 125 km s^{-1} redward of the systemic velocity. These velocity offsets imply that there are powerful outflows in high-redshift LAEs. They also ease the transmission of Lyα photons through the interstellar medium and intergalactic medium around the galaxies. By measuring these offsets directly, we can refine both Lyα-based tests for reionization, and Lyα luminosity function measurements where the Lyα forest affects the blue wing of the line. Our work also provides the first direct constraints on the strength of the [O III] line in high-redshift LAEs. We find [O III] fluxes of 7 and 36 $\times 10^{-17}$ erg s^{-1} cm^{-2} in two z $\sim$ 3.1 LAEs. These lines are strong enough to dominate broad-band flux measurements that include the line (in this case, K_s band photometry). Spectral energy distribution fits that do not account for the lines would therefore overestimate the 4000Å (and/or Balmer) break strength in such galaxies, and hence also the ages and stellar masses of such high-z galaxies.

2.2 Introduction

The Lyman-α emission line is a highly efficient tool for identifying and studying star forming galaxies at high redshifts. This line can carry up to 6% of the bolometric luminosity of a young stellar population (Partridge & Peebles, 1967) and is conveniently placed for observations by ground-based optical observatories for $2 \leq z \leq 7$. However, the transmission of Lyα emission is complicated by its resonant scattering interaction with neutral hydrogen, both within the galaxy emitting the line and in the surrounding intergalactic medium (IGM). The Lyα line is observed in about 25% of $z \sim 3 - 5$ Lyman-break galaxies (LBGs) (e.g., Steidel et al., 2000; Dow-Hygelund et al., 2007; Rhoads et al., 2009), a percentage that may increase with increasing redshift (Shimasaku et al., 2006; Stark et al., 2010). The opposite trend is seen at redshifts less than two, meaning the fraction of galaxies exhibiting Lyα emission decreases at these lower redshifts (Reddy et al., 2008; Hayes et al., 2010; Cowie et al., 2010). The Lyα line is observed to have a characteristically asymmetric profile, with a sharp cutoff on the blue side and a more extended wing on the red side (e.g., Rhoads et al., 2003). In Lyman-break selected galaxies, the peak of the Lyα line is typically redshifted by several hundred km s^{-1} with respect to interstellar absorption lines and/or nebular emission lines (Shapley et al., 2003; Steidel et al., 2010), whereas this measurement has not been made in Lyα selected galaxies until this paper.

Besides being a useful tool for studying galaxy properties, Lyα galaxies also offer unique and powerful probes of cosmological reionization (e.g., Rhoads & Malhotra, 2001; Malhotra & Rhoads, 2004, 2006; Kashikawa et al., 2006; McCandliss, 2009; Dayal et al., 2010) The detailed interpretation of these tests can be substantially affected by velocity offsets between Lyα and the systemic redshift,

because a redshifted line is less affected by the damping wing of Lyα absorption from the IGM (Santos, 2004; Malhotra & Rhoads, 2006; Dijkstra & Wyithe, 2010).

It is not sufficient to assume that the velocity offsets seen in LBG samples hold for Lyα selected samples. LAEs are typically less massive than presently available Lyman-break selected samples at similar redshifts (Venemans et al., 2005; Gawiser et al., 2006; Finkelstein et al., 2007; Pirzkal et al., 2007; Nilsson et al., 2007). They should have correspondingly lower escape speeds, provided that stellar mass correlates broadly with dark matter halo mass. Such a trend is discussed by Gawiser et al. (2007), where their sample of $z \sim 3.1$ LAEs have typical stellar masses of 1×10^9 $M_\odot$ and median halo masses of $7.9 \times 10^(10)$ $M_\odot$. Gawiser et al. point out that these values are significantly smaller than those values for LBGs at $z \sim 3.1$, which have stellar masses of $\sim 2 \times 10^{10}$ $M_\odot$ and halo masses of $\sim 3 \times 10^{11}$ $M_\odot$ (Shapley et al., 2001; Adelberger et al., 2005). Galactic winds (and indeed many other astrophysical outflows) typically have flow speeds near the escape speed for the object, and the observed velocity offset of a Lyα line is roughly double the wind speed (Verhamme et al., 2006). Additionally, the velocity offsets in Lyman-break samples are inversely correlated with the Lyα emission strength, as characterized by equivalent width (Shapley et al., 2001), and the equivalent widths of the Lyα selected samples are much larger on average than those of LBG samples. Finally, Lyα selected galaxies are typically small in physical size (Bond et al., 2009, 2010; Malhotra et al., 2010).

We present here the first direct measurements of the velocity offset between Lyα and nebular emission lines for typical Lyα selected galaxies. Our measurements are based on a combination of near-infrared spectroscopy with the new LUCIFER instrument on the Large Binocular Telescope, and optical spectroscopy using Hectospec on the MMT. We selected targets for the study from a

large area narrowband survey conducted with the 90Prime camera on the 2.3m Bok telescope of the Steward Observatory.

In section 2.3 we describe our observations and data analysis methods. We present our observational results in section 2.4, and discuss their implications in section 2.5. Where relevant, we adopt $H_0 = 70$ km s^{-1} Mpc^{-1}, $\Omega_m = 0.3$, $\Omega_\Lambda = 0.7$ (Spergel et al., 2007). Also we use the following vacuum wavelengths, 1215.67 Å for Lyα, 3729.875 Å for [O II], 4862.683 Å for Hβ and 4960.295/5008.240 for [O III] from the Atomic Line List v2.04[1]. All magnitudes quoted are AB magnitudes unless otherwise specified.

2.3 Observations and Data Processing

2.3.1 Narrowband Survey - Observations and Data Reduction

We completed a deep narrowband survey for LAEs at z $\sim$ 3.1 using the 90Prime Camera on the 2.3m Bok telescope at the Steward Observatory (Williams et al., 2004). The survey was completed in the COSMOS field centered at RA 10:00:28.6 and DEC +02:12:21.0 (J2000) (Capak et al., 2007). The KPNO MOSAIC[O III] filter, centered at 5025 Å, with a bandwidth of 55 Å, was used to select Lyman alpha emission at redshifts z $\sim$ 3.1. The data was obtained through time allocated by Steward Observatory in February 2007 (PI Finkelstein) and February and March 2009 (PI McLinden). We have created a 1.96 deg^2 image, representing a total integration time of 16.67 hours. The complete details of this survey and the data reduction process will be highlighted in a forthcoming paper.

[1] http://www.pa.uky.edu/~peter/atomic/index.html

2.3.2 Broadband Data

We obtained publicly available broadband imaging data in CFHT u^* and SDSS g^+ bands from the NASA/IPAC Infrared Science Archive[2] to complement our narrowband survey. The g^+ imaging data (v2.0) comes from Suprime-Cam (Miyazaki et al., 2002) on the Subaru 8.3m telescope. The u^* band imaging data (v5.0) comes from the MegaPrime/MegaCam[3] on the Canada-France-Hawaii 3.6m Telescope. The 5σ depth in a $3''$ aperture in each band is 26.4 and 27.0 for the u^* and g^+ bands, respectively (Capak et al., 2007). These broadband images were registered to our narrowband image using the IRAF tasks WCSMAP and GEOTRAN, which resamples the broadband images to match the coordinate system of the narrowband image (0.45 $''$pixel).

2.3.3 Candidate selection from Narrowband and Broadband Data

We used the SExtractor package (Bertin & Arnouts, 1996) to perform source detection in the narrowband and broadband images. SExtractor was run in dual-image mode, first with narrowband image as both the detection and measurement image, and a second time with the narrowband as the detection image and broadband image as the measurement image. We selected LAE candidates based on the strength of their narrowband versus broadband excess as well as their colors as outlined in Rhoads & Malhotra (2001).

[2]http://irsa.ipac.caltech.edu/data/COSMOS/datasets.html

[3]Based on observations obtained with MegaPrime/MegaCam, a joint project of CFHT and CEA/DAPNIA, at the Canada-France-Hawaii Telescope (CFHT) which is operated by the National Research Council (NRC) of Canada, the Institut National des Science de l'Univers of the Centre National de la Recherche Scientifique (CNRS) of France, and the University of Hawaii.

Namely, LAE candidates must be detected in the narrowband at the 6σ level, their flux in the narrowband must exceed that in the broadband (g^+ band) by at least a factor of 2 and their narrowband flux must exceed their g^+ band flux at the 4σ level. Finally, candidates must have flux in the filter bluward of of the Lyα line (u^* band) consistent with expected Lyα forest absorption blueward of the Lyα line and consistent with a u^* - g^+ color ≥ 2. Selection criteria are shown below in equations 1–4.

$$f_{nb}/\delta f_{nb} \geq 6 \tag{2.1}$$

$$f_{nb}/f_g \geq 2 \tag{2.2}$$

$$f_{nb} - f_g \geq 4\left(\delta f_{nb}^2 + \delta f_g^2\right)^{1/2} \tag{2.3}$$

$$f_u \leq 10^{-4/5} f_g + \left(3 \times \delta f_u\right) \tag{2.4}$$

Here f_{nb} is the narrowband flux, f_g is the g band flux, f_u is the u band flux, δf_{nb} is the flux error in the narrowband, δf_g is the flux error in the g band, and δf_u is the flux error in the u band. The second criterion requires that objects have Lyα equivalent widths ≥ 57.5 Å. The decision to require a 6σ detection in the narrowband and to require a 3σ non-detection blueward of the Lyman-break indicates that these are stringent selection criteria, meant to exclude false detections and low redshift interlopers. We used isophotal magnitudes (MAG_ISO) from SExtractor to measure the magnitudes and fluxes of each object. Isophotal magnitudes were chosen because they have been found to produce the most accurate colors when SExtractor is run in dual-image mode (Holwerda, 2005). Isophotal magnitudes are not measured within a fixed aperture for each object, but rather determines the magnitude from the number of counts in pixels above the user defined threshold and hence each object has a unique 'aperture' in which its flux is measured. For instance, the two LAEs with detected [O III] emission have ex-

tracted narrowband isophotal areas of 20.86 arcsecond^2 and 8.71 arcsecond^2 (later referred to as objects LAE40844 and LAE27878, respectively). Similar selection criteria used at z=4.5 have typically yielded a spectroscopic success rate of 80% (Dawson et al. 2004, 2007, Rhoads et al. 2003, 2005, Wang et al. 2009).

2.3.4 Optical Spectroscopy - Observations and Data Reduction

We obtained optical spectra of LAE candidates in January, February and April 2009, using the Hectospec multi-fiber spectrograph at the 6.5m MMT Observatory (a joint facility of the Smithsonian Astrophysical Observatory and the University of Arizona). Hectospec has a 1 deg^2 field of view and spectral coverage from 3650 - 9200 Å. The resolution of the instrument is $\sim$ 6 Å. Optical spectra are crucial for confirming that candidates are in fact LAEs at the correct redshift and not lower redshift interlopers and for determining the exact wavelength for the Lyα line.

We reduced the Hectospec data and extracted 1D spectra using the External SPECROAD[4] pipeline developed by Juan Cabanela. The External SPECROAD pipeline applies bias, dark and flat field corrections as well as wavelength calibration using He-Ne-Ar arc lamps. Typical residuals from the wavelength calibration are 0.15 Å.

The optical spectra of the three objects chosen for near-infrared followup are shown in Figure 2.1. These optical spectra confirm that these objects are in fact LAEs. The spectra show strong Lyα emission at the expected wavelength and the line displays the characteristic asymmetry expected for this line when emitted from a high-z source (Rhoads et al., 2003; Dawson et al., 2004; Kashikawa et al., 2006). See section 3.1 for further discussion of this asymmetry. Finally the

[4]http://iparrizar.mnstate.edu/$\sim$juan/research/ESPECROAD/index.php

spectra were checked for the presence of any other optical lines. No additional emission lines were observed at the wavelengths where they might be expected for foreground [O II] or [O III] emission line objects.

2.3.5 Near-Infrared Spectroscopy - Observations and Data Reduction

Three of our brightest confirmed LAEs after Hectospec observations were observed in the near-infrared (NIR) using the new near-infrared instrument LUCIFER (LBT NIR Spectrograph Utility with Camera and Integral-Field Unit for Extragalactic Research) on the 8.4m LBT (Seifert et al., 2003; Ageorges et al., 2010) The Lyα line flux of these objects chosen for NIR followup, derived from their narrowband and broadband magnitudes, ranges from 0.94 – 3.6×10^{-16} erg s^{-1} cm^{-2}. LUCIFER1 is the first of two planned NIR instruments for the two 8.4m mirrors of the LBT. LUCIFER1 currently operates on one mirror of the LBT and is capable of spectroscopy and imaging in the wavelength range 0.85μm – 2.5μm. Our observations were performed in queue mode during LUCIFER's Science Demonstration Time in December 2009 and continued during the Arizona Queue in January and February 2010.

We used the longslit mode of LUCIFER with a 1$''$ slit utilizing the H+K grating with 200 lines/mm and the N1.8 camera. The image scale of the N1.8 camera is 0.25$''$pixel. We obtained 10 two-minute integrations for our brightest LAE (henceforth LAE40844). Our second object (henceforth LAE27878) was observed over 20 four-minute integrations. Our final object (henceforth LAE14310) was observed over 25 four-minute integrations. The central wavelength in this setup is 1.93 μm and the spectral coverage spans essentially the full H and K band windows. The spectral resolving power with the 4 pixel slit ranges from 940 near 1.6μm to 1286 near 2.2 μm or a resolution of $\sim$ 4.3 Å/pixel.

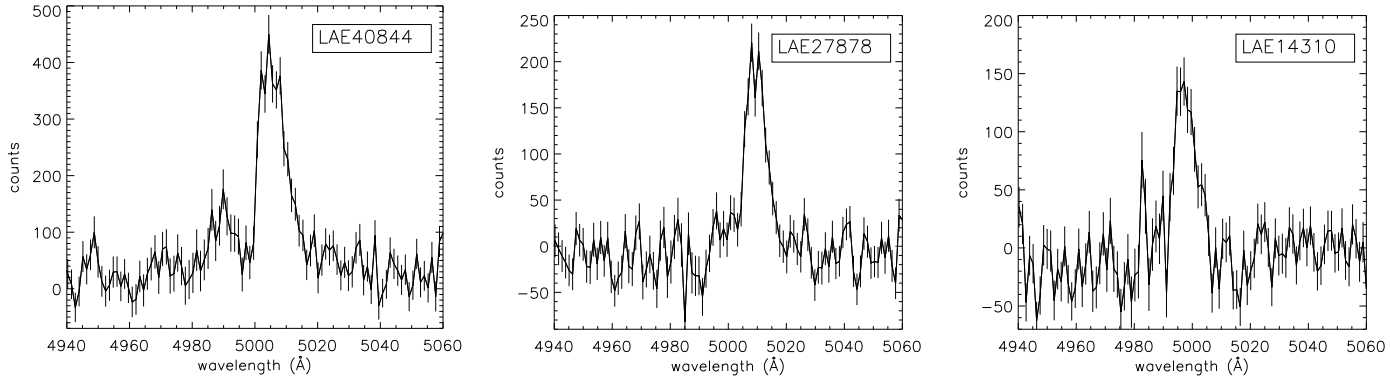

Figure 2.1 Hectospec optical spectra - used for confirmation of the objects as Lyα emitting galaxies at z $\sim$ 3.1. LAE40844 has an additional feature, a 'blue bump', at $\lambda \sim 4990$ Å, which is discussed in section 3.4. The spike seen near 4982 Å is noise and not an additional feature.

We utilized the DOSLIT routine in IRAF (Valdes, 1993) to reduce the 2D spectra. To simplify reduction, our observations were designed so that a bright (R $\sim$ 12–18) continuum source also shared the slit with each LAE. This allows for a trace to be created using the bright continuum object. The trace was then shifted along the spatial axis to extract the much fainter LAE, whose continuum emission is undetectably faint in individual exposures. We performed flat fielding and dark correction before aperture extraction. An aperture of 6 pixels was used for extraction. Wavelength calibration, also performed as part of the DOSLIT task, was done using an argon lamp spectrum observed in the same setup as our science observations. After reduction, we averaged individual frames using the IRAF task SCOMBINE to produce a single averaged spectrum for each object. Average RMS uncertainties from wavelength calibration for the two spectra with [O III] detection were 0.64 Å and 0.48 Å for LAE40844 and LAE27878, respectively. Residual bright night sky lines, a problem when extracting faint sources, were interpolated over in each night's averaged spectrum using the SKYINTERP task found in the WMKONSPEC package designed for Keck NIRSPEC reduction[5].

Flux calibration proceeded using the bright continuum sources that shared the slit with our LAEs as described in the paragraph above. Henceforth these continuum objects will be called calibration stars. This process corrected for telluric absorption and transformed our flux to F_λ units. LAE40844 was calibrated using SDSS J100126.08+021902.2 and LAE27878 was calibrated using SDSS J100025.10+022552.0. We flux calibrated each night's calibration star spectrum using an appropriate Pickles model spectrum (Pickles, 1998), scaled in flux to match the apparent V magnitude of the observed calibration star. The appropriate Pickles model was chosen based on the spectral type of the calibration star

[5]http://www2.keck.hawaii.edu/inst/nirspec/wmkonspec.html

and spectral type was determined from SDSS u-g and g-r colors of the calibration stars as outlined in Fukugita et al. (2003). The SDSS u, g and r magnitudes come from SDSS DR7. The V magnitude of the observed of the calibration star was determined from its SDSS colors and the Lupton (2005) color transformation from SDSS g-r color to V magnitude[6]. We then created a sensitivity curve by dividing the scaled down Pickles model by the calibration star's stellar spectrum in counts. We then multiplied each night's LAE spectrum (in counts) by that night's sensitivity curve to produce a final flux-calibrated LAE spectrum.

2.3.6 Cross check of photometric redshift

We cross checked the coordinates of each LAE with the sources in the COSMOS Photometric Redshift Catalog Version 1.5 (Ilbert, Capak & Salvato et al., 2009). We found a unique match for each object, within $1''$ in all cases. The photometric redshift of LAE40844 is $z_{phot} = 3.094$, with a 68% confidence range of $3.08 < z_{phot} < 3.11$. The photometric redshift of LAE27898 is 3.086, with a 68% confidence range of $3.02 < z_{phot} < 3.12$. Finally, the photometric redshift of LAE14310 is 3.035, with a 68% confidence range of $2.98 < z_{phot} < 3.11$.

2.3.7 Cross check with Chandra COSMOS X-ray Sources

We also compared the locations of our LAEs with the Chandra COSMOS Survey Point Source Catalog (Elvis et al., 2009) to exclude contamination from AGNs. The Chandra COSMOS Survey Point Source Catalog contains 1761 X-ray sources in the full 0.5–10keV band with a limiting depth of 5.7×10^{-16} erg s^{-1} cm^{-2}. The survey covers the central ~ 0.9 deg^2 of the COSMOS field. We find no X-ray sources matching the coordinates of any of our LAEs within $12.8''$ which is

[6]http://www.sdss.org/dr6/algorithms/sdssUBVRITransform.html

much larger than the combined positional uncertainties of the narrowband and X-ray catalogs. This gives upper limits $f_x/f_{\mathrm{Ly}\alpha} \leq 1.6 - 6.0$ for the three sources with LUCIFER spectra— below the typical ratio $f_x/f_{\mathrm{Ly}\alpha} \sim 8$ for type I quasars, and overlapping the range ($f_x/f_{\mathrm{Ly}\alpha} \sim 3$–4) observed for type II quasars (e.g., Zheng & Miralda-Escude, 2010). Thus the X-ray observations suggest that the Lyα in these objects is indeed powered by star formation rather than AGN activity, though the present X-ray data are not deep enough to prove this case by themselves. Also we note that the modest [O III] velocity widths of $\sim$ 200–300 km s^{-1} seen in our two LAEs are much lower than the typical velocity widths of around 1000 km s^{-1} expected for Type 1 AGN.

2.4 Results

2.4.1 Gaussian fits to the [O III] and Lyα lines

To determine the central wavelength and line flux of each emission line we fit a Gaussian plus constant to each emission line. In the case of the [O III] line, we fit a symmetric Gaussian to the line using the MPFITEXPR IDL routine, which is part of the MPFIT package.[7] For the Lyα line we fit an asymmetric Gaussian by modifying the ARM_ASYMGAUSSFIT IDL routine[8], which also utilizes the MPFITEXPR routine. In its unmodified form, ARM_ASYMGAUSSFIT basically fits the left and right sides of the central wavelength with different Gaussians and then requires that in the final fit the left and right curves must have the same center and same amplitude where they meet, meaning there are eight parameters, four for each side of the curve (amplitude, center, sigma, constant) but only six of these are free parameters. This allows for a single curve to be fit, but the curve can

[7] developed by Craig Markwardt http://www.physics.wisc.edu/ craigm/idl/idl.html

[8] developed by Andrew Marble http://hubble.as.arizona.edu/idl/arm/

have different sigma values for the right and left sides of curve, making it ideal for fitting a Lyα line with a truncated blue side and extended red wing. We modified ARM_ASYMGAUSSFIT by fixing the constant on the left side of the Lyα emission line to a pre-determined constant measured as the average continuum level from 4000 – 5000 Å. This reduces the number of free parameters from 6 to 5 when fitting the Lyα line. The constant on the right side of the Lyα line is allowed to vary, as one can expect a slightly higher continuum level redward of rest-frame Lyα.

We quantified the asymmetry of the Lyα peaks by defining the ratio of the red side best-fit sigma to the blue side best-fit sigma, or asymmetry= $\sigma_{red}/\sigma_{blue}$. Using this definition, any line with an asymmetry measure $>$ 1.0 is considered asymmetric. From this definition of we find asymmetry measurements of 1.1 $\pm$ 0.1 , 1.7 $\pm$ 0.2 and 1.0 $\pm$ 0.1 for LAE14310, LAE40844 and LAE27878, respectively, meaning the Lyα line in LAE40844 is highly asymmetric, whereas the Lyα lines in LAE14310 and LAE27878 appear to be symmetric within the errors. For comparison with other asymmetry measurements in the literature we also calculated asymmetry using a_λ and a_f (Rhoads et al., 2003) from the best fit asymmetric Gaussians. a_λ is 1.2, 2.2 and 1.2 and a_f is 1.2, 1.8 and 1.1 for LAE14310, LAE40844 and LAE27878, respectively.

We defined the redshift of the emission line using the central wavelengths determined from these fits (from z =$(\lambda_{obs}/\lambda_{em}) - 1$ where λ_{em} is the rest-frame vacuum wavelength and λ_{obs} is the central wavelength of the best fit). Line flux for the [O III] line was determined from the area under the best fit symmetric Gaussian. Line flux for the Lyα line was determined from the narrowband line flux and the area under the best fit asymmetric Gaussian was scaled to match this flux, where the passband of the filter transmission curve was taken into account

to assign the appropriate amount of flux to the main Lyα peak in LAE40844 and this object's secondary 'blue bump' discussed in more detail in section 3.4. Errors on the area were determined directly from the PERROR output from the MPFITEXPR routine, which returns the one-sigma error on fitted parameters. PERROR output values were also used to quantify the error on the best fit central wavelength, but an additional error term was included here to account for wavelength calibration errors from the Hectospec and LUCIFER spectra. Errors on calculated values for redshift and velocity offsets between the Lyα line and the [O III] line were derived from best fit central wavelength and its associated error as described directly above. Best fits are calculated from unsmoothed spectra, while the spectra in Figure 2.2 and 2.3 are plotted after 3-pixel boxcar smoothing.

2.4.2 [O III] detection with LUCIFER

We detect the [O III] 5008.240/4960.295 Å doublet in two of the three LAEs, LAE40844 and LAE27878. For the stronger [O III] line (rest frame vacuum wavelength of 5008.240 Å), we measure a line flux of $35.48 \pm 1.15 \times 10^{-17}$ erg s^{-1} cm^{-2} in LAE40844 and $6.96 \pm 0.33 \times 10^{-17}$ erg s^{-1} cm^{-2} in LAE27878.

The second strongest [O III] line (rest frame vacuum wavelength of 4960.295 Å) was also found in the same two LAEs. The line fluxes measured for this line from best fit Gaussians were $14.82 \pm 2.24 \times 10^{-17}$erg s^{-1} cm^{-2} and $1.47 \pm 0.37 \times 10^{-17}$erg s^{-1} cm^{-2} for LAE40844, LAE27878, respectively. The ratio of this secondary [O III] line to the stronger [O III] line is within 2σ of the theoretical value (1/3) in both galaxies. This provides a check of the data analysis and increases confidence that this is the 4960.295 Å line. Table 2.1 summarizes the [O III] and Lyα line fluxes for each LAE, along with relevant broadband and narrowband characteristics.

LAE14310 showed no detectable [O III] emission. This could be explained if LAE14310 was in fact a lower redshift interloper, but a visual inspection of the optical spectrum has ruled out the object as an [O II] emitter at z $\sim$ 0.34 or an [O III] emitter at z $\sim$ 0. In the case of an [O II] emitter at z $\sim$ 0.34 we would expect to see [O III] at $\lambda \sim 6710$ Å, which we do not see. If the object were a z $\sim$ 0 [O III] emitter, we would expect to see the $\lambda = 4960.295$ Å[O III] line with a line flux of $\sim 1.8 \times 10^{-16}$, which we also don't see. The more likely scenarios are then that the [O III] emission in this object is weak, or the [O III] line is being covered by strong OH lines/H_2O absorption in this region.

We are unable to detect Hβ and/or determine upper limits for Hβ emission, likely because the redshift of each object has placed the Hβ line under strong OH lines and/or under H_2O absorption features. We do not detect the [O II] (3729.875 Å) line by visual inspection in either LAE27878 or LAE40844. Determining an upper limit for this line by fixing the expected [O II] wavelength based on the redshift measured from the [O III] line did not yield a significant upper limit.

2.4.3 Systemic Redshifts and Velocity offsets between [O III] and Lyα

Using the Gaussian fits described above, we measured systemic redshifts from the strongest [O III] line in the two objects with detections, finding redshifts of 3.11170 ± 0.00014 and 3.11879 ± 0.00011 for LAE40844 and LAE27878, respectively.

Measuring the redshift of each object using the Lyα line instead of the [O III], yields redshifts of 3.11639 ± 0.00021 and 3.12051 ± 0.00021 for LAE40844 and LAE27878, respectively, after corrections for the Earth's motion. To correct

Galaxy Characteristics	LAE14310	LAE27878	LAE40844
u^* Magnitude	25.46 ± 0.29	26.54 ± 0.50	25.56 ± 0.32
Narrowband KPNO MOSAIC[O III] Magnitude	22.56 ± 0.11	23.34 ± 0.15	21.82 ± 0.06
g^+ Magnitude	24.49 ± 0.13	25.47 ± 0.19	23.66 ± 0.06
$z_{Ly\alpha}$ [1]	3.11043 ± 0.00021	3.12051 ± 0.00021	3.11639 ± 0.00021
z_{OIII}		3.11879 ± 0.00011	3.11170 ± 0.00014
Lyα Equivalent Width[2,6]	89^{+17}_{-20}	118^{+34}_{-40}	78^{+8}_{-8}
Lyα Line Flux from Narrowband[3,4]	$18.7^{+2.25}_{-2.51}$	$9.41^{+1.42}_{-1.63}$	$36.1^{+2.35}_{-2.47}$
Upper limit on xray / Lyα Flux Ratio	3.0	6.1	1.6
O III line flux ($\lambda = 5008.240$ Å)[3]		6.96 ± 0.33	35.48 ± 1.15
O III line flux ($\lambda = 4960.295$ Å)[3]		1.47 ± 0.37	14.82 ± 2.24
O III velocity width($\lambda = 5008.240$ Å)[5]		189.3 ± 10.3	281.1 ± 9.8
O III FWHM ($\lambda = 5008.240$ Å)[6]		13.0 ± 0.7	19.3 ± 0.7
v_{offset} of O III from Lyα [5]		$+125 \pm 17.3$	$+342 \pm 18.3$

Table 2.1 Narrowband, broadband, and emission line characteristics of LAE14310, LAE27878, and LAE40844.

[1] corrected for Earth's motion

[2] Rest Frame, from Narrowband flux, calculated as $(F_{NB} - F_g)/(F_g/55 - F_{NB}/1265)$ where 55 Å is bandpass of KPNO MOSAIC[O III] filter and 1265 Å is bandpass of Subaru g^+ filter, F_{NB} is flux in narrowband, F_g is flux in g^+ band.

[3] 10^{-17} erg s^{-1}cm^{-2}

[4] Calculated as $(F_{NB} - F_g)(c/\lambda_c^2)d\lambda$ where λ_c central wavelength and dλ is bandpass of KPNO MOSAIC[O III] filter

[5] km s^{-1}

[6] Å

for the Earth's motion we calculated topocentric radial velocities[9] for the two observing locations (MMT and LBT) for the nights the objects were observed at each location. The generally accepted interpretation of this discrepancy in redshift measurements from interstellar emission lines and Lyα is that there is a kinematic offset between the lines caused by a large scale outflow, an outflow likely driven by active star formation.

Assuming that the emission lines originate from a single redshift, we pin the lines to the redshift of the [O III] line and use this frame to calculate a velocity offset between the two lines. We justify using the nebular emission to define the systemic redshift of the galaxy since the [O III] emission originates from H II regions surrounding ionizing stars. These regions ought to be at the systemic redshift of the galaxy. While the Lyα initially departs from the same regions, resonant scattering, which effects Lyα and not [O III], changes the observed location of Lyα emission.

We derived velocity offset between the 5008.240 Å [O III] line and Lyα line based on the central wavelength of each line, determined by the best fit asymmetric and symmetric Gaussians for the Lyα and [O III] lines, respectively. We find velocity offsets of $+342 \pm 18.3$ km s^{-1} and $+125 \pm 17.3$ km s^{-1} for LAE40844 and LAE27878, respectively. The velocity offsets between the [O III] and Lyα lines are shown in Figure 2.2.

Steidel et al. (2010) note that their redshift determinations for z $\simeq$ 2 –3 galaxies based on NIR Hα measurements have an inherent uncertainty of $\sim$ 60 km s^{-1}. This estimate is based on repeated observations of the same galaxy with their 0.76″ slit in different positions. The uncertainty is explained as arising from the fact that in each measurement they are only measuring the velocity of the

[9] http://fuse.pha.jhu.edu/support/tools/vlsr.html

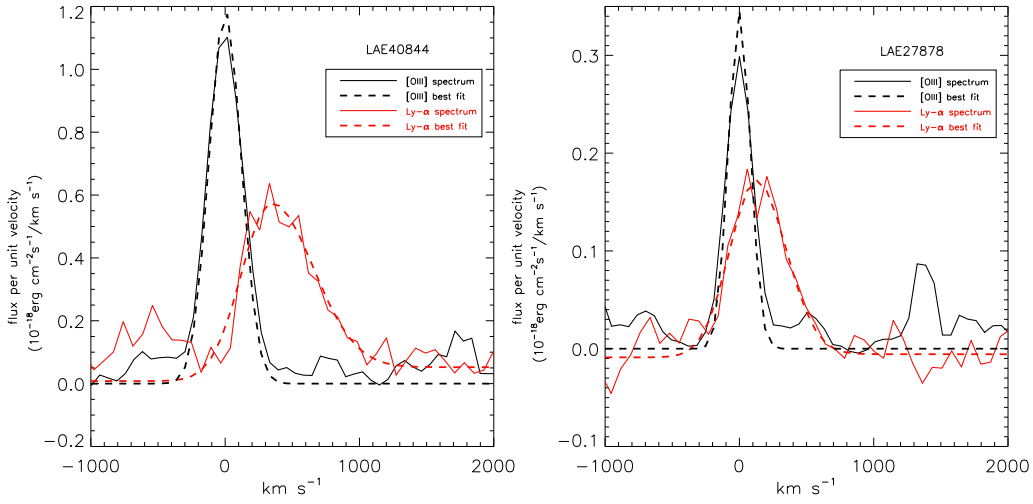

Figure 2.2 [O III] line and Lyα lines with their corresponding best-fit Gaussians. Velocity offset between [O III] and Lyα line for LAE40844 is 342 km s^{-1} and the velocity offset for LAE27878 is 125 km s^{-1}. The feature near +1400 km s^{-1} in LAE27878 is a residual night sky line at $\sim$ 20728.17 / 20729.859 Å (Rousselot et al., 2000).

fraction of the flux that entered the slit. We find that our [O III] measurements for our z $\sim$ 3.1 galaxies should not be subject to such a large uncertainty from this effect due to our larger slit width (1″) and small galaxy sizes. The sizes of our galaxies, from ACS i-band half light radii, are 1.1 and 1.3 kpc, for LAE40844, LAE27878, respectively (Malhotra et al., 2010). The corresponding half-light angular diameters are still less than half the slit width. The 1.5″ diameter fibers should also minimize flux losses for our Lyα observations, however, we concede that our error bars may be lower limits due to such systematics we may not be fully taking into account.

2.4.4 'Blue bump' in LAE40844 - Velocity offset of secondary Lyα feature

LAE40844 has another feature of interest in its optical spectrum, namely a smaller, secondary Lyα peak blueward of the systemic velocity of the object. See Figure 2.3 for a detailed view of this feature. This feature is fit with an asymmetric Gaussian as described for the main Lyα line in section 3.1, but the constants on the left and right sides of the Gaussian are required to be equal (and to be equal to the pre-determined constant level also described in section 3.1) to ensure that the main Lyα peak did not interfere with our best fit measurements of this secondary peak. This essentially reduces the number of fitted parameters for the blue bump from 5 to 4, meaning that when both the main Lyα line and the blue bump are fit, a total of 9 parameters are returned (5 for main Lyα peak, 4 for blue bump). Our method yields a velocity offset from the [O III] line of -453.7 $\pm$ 50.7 km s^{-1}, after correction for the Earth's motion. From this measurement we determine that the two Lyα peaks are offset from one another by +796.2 $\pm$ 53.9 km s^{-1}.

Additionally, using the flux calibration we derived from the narrowband line flux, we find that this blue Lyα peak has a line flux of $\sim$ 1.08 $\times 10^{-16}$ erg s^{-1} cm^{-2}. When determining this calibration we found that based on the transmission curve of the narrowband filter, the blue bump contributed at most $\sim$ 9.4 % of the total narrowband line flux (3.61 $\times 10^{-16}$ erg s^{-1} cm^{-2}). Comparing this to a line flux of $\sim$ 3.27 $\times 10^{-16}$ erg s^{-1} cm^{-2} for the red Lyα peak we find an approximate flux ratio, red:blue, for the two lines of 3.0. In other words, the strength of secondary (blue) peak is roughly 33% that of the main (red) peak. In section 2.5 we discuss a scenario that can give rise to this blue bump and compare the velocity offset we find between the two Lyα lines to velocity offsets that have been presented in the literature on Lyα radiative transfer.

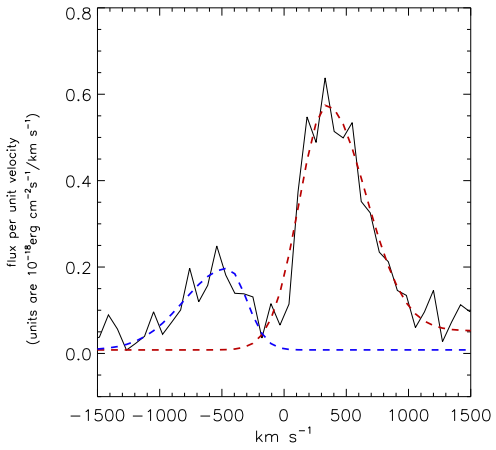

Figure 2.3 LAE40844, best fit asymmetric Gaussian to redshifted Lyα emission in red, best fit asymmetric Gaussian to blue shifted Lyα emission in blue, optical spectrum in black. Velocity offset between the Lyα two peaks is $+796.2 \pm 53.9$ km s^{-1}.

2.4.5 Effect of the [O III] Emission Line on Mass and Age Estimates

The COSMOS field has a deep K_s-band (centered at 21460Å, $\Delta\lambda = 3250$ Å) coverage from CFHT WIRCAM, with a 5σ depth of ~ 23.8 mag in a $3''$ aperture on a PSF matched image. For our z $\sim$ 3.1 LAEs, this band will encompass both the continuum and [O III] emission. The 2008 COSMOS Intermediate and Broad Band Photometry Catalog (Capak et al., 2007) has K_s band magnitudes of 22.61 ± 0.07 for LAE40844, and 24.91 ± 0.62 for LAE27878 (MAG_AUTO measurements from a $3''$ aperture). Our measured [O III] line fluxes can account for the entire K_s band fluxes, where we find K_s-band magnitudes of 23.09 ± 0.036 and 24.79 ± 0.053 for LAE40844 and LAE27878, respectively, using just the [O III] line fluxes. This shows that our detected [O III] emission lines alone can be

responsible for all or nearly all the flux measured in the K_s band for both of these LAEs.

This has important implications for mass and age estimates of high redshift galaxies. These estimates typically rely on the size of the Balmer break to determine the age of the galaxy. If, as is the case for our two LAEs, there is a dominant emission line polluting the location red ward of the Balmer / 4000 Å break, then the size of the break may be overestimated and the subsequently derived ages and stellar masses may be overestimated. Schaerer & de Barros (2009) found that when nebular emission lines were included, SED fitting of the Eyles et al. (2007) sample of 10 $z \sim 6$ galaxies yielded an average age ~ 4 times younger than what was found without the emission lines included. The average stellar mass estimate also decreased from 1.2×10^{10} $M_\odot$ without emission lines to 7.8×10^{9} $M_\odot$ when nebular emission was included. Some studies of Lyα emission in Lyman-break selected populations have found that the strongest Lyα emitters have blue UV spectral slopes but red optical slopes (Shapley et al., 2003; Kornei et al., 2010), and have concluded that Lyα emission is strongest in LBGs that are older but relatively dust-free. If strong nebular line emission contributes to the observations of red rest-optical slope, it might be possible to reinterpret such observations in terms of young, strongly line emitting galaxies, although Kornei et al. (2010) argue that their observed correlations between Lyα strength and stellar population age are unchanged when they select objects only at redshifts where the optical continuum filters are line-free. Previous work on stellar populations of Lyα-selected galaxies has found that nebular line emission is required to explain observed rest-optical colors (Finkelstein et al., 2008). Recently, at the highest redshifts, Ono et al. (2010) have shown that either old stellar populations or young ones with strong nebular emission can reproduce the composite SEDs of Lyα selected galaxies. The older

models have correspondingly higher stellar masses, since mass to light ratio increases strongly with age. Our observations provide *direct* observational evidence that nebular line flux dominates the rest optical in analogous objects at $z \approx 3$, and hence supports the interpretation of the high redshift Lyα selected populations as young and low-mass objects.

2.5 Discussion

2.5.1 [O III] luminosities

The [O III] line has been measured in other objects at similar redshifts. Pettini et al. (2001, henceforth P01) find [O III] (5007 Å) luminosities of 3.5 – 15.6 $\times$ 10^{42} erg s^{-1} in four individual z $\sim$ 3.1 LBGs observed with VLT1/ISAAC and/or Keck II/NIRSPEC. Comparing this to our range of luminosities for the 5007 Å line for two z $\sim$ 3.1 LAEs of 6.1 – 31.0 $\times$ 10^{42} erg s^{-1}, it appears that our fainter 5007 Å measurement falls in the P01 range, while the stronger of our two 5007 Å lines is almost double that of the brightest luminosity in the P01 sample. Luminosities for the 4959 Å line in the P01 sample are 1.4 – 6.5 $\times$ 10^{42} erg s^{-1}. This yields the same trend we see in the 5007 Å line; where our fainter 4959 Å measurement falls in the P01 range, and our brighter 4959 Å line is approximately twice that of the brightest 4959 Å measurement in the P01 sample.

[O III] luminosities from lensed galaxies around z $\sim$ 3 have also been documented. Fosbury et al. (2003) measured the [O III] line in a lensed H II galaxy, also known as the Lynx arc (Holden et al., 2001), at a redshift of z $\sim$ 3.36. Using NIRSPEC K-band spectra they find an [O III] luminosity of 28.3 $\pm$ 0.3 $\times$ 10^{42} erg s^{-1} for the 5007 Å line and 9.8 $\pm$ 0.3 $\times$ 10^{42} erg s^{-1} for the 4959 Å line. These luminosities (which have been corrected for magnification) are quite comparable

to our measurements for the 5007 Å and 4959 Å lines. Finkelstein et al. (2009b) measured the [O III] line in a lensed ultraviolet-luminous z = 2.73 galaxy known as the 8 o'clock arc. For the 4959 Å line they find a luminosity of $8.9 \pm 0.4 \times 10^{42}$ erg s^{-1} (after correction for magnification). This again falls right in the range reported for our two LAEs. The 5007 Å line was not reported by Finkelstein et al. (2009b) because it fell in an area of low atmospheric transmission which required a correspondingly large tellluric correction and led to large uncertainties in any measurements from the line.

Looking at our sample of two galaxies, the [O III] luminosities in LAE27878 are most similar to the P01 LBGs while the more luminous [O III] lines in LAE40844 are more comparable to more luminous [O III] lines found in galaxies studied via lensing. A larger sample of NIR spectra with [O III] line measurements for LAEs will help us understand the range of [O III] luminosity in LAEs and its implications.

2.5.2 Lyα line profiles and outflow models

In addition to the information that can be gleaned from the line fluxes of nebular emission lines such as [O III], the asymmetric profiles of Lyα emission lines themselves carry information on the physical conditions and processes in these objects. Resonant scattering can lead to asymmetric profiles through radiative transfer processes operating either within the Lyα emitting galaxy, or in the surrounding intergalactic medium. Establishing the systemic velocity with the [O III] line sheds new light on those processes and conditions.

We find that the Lyα line profiles seen in LAE40844 and LAE27878, and the velocity offset of the Lyα line from systemic in both objects is in good agreement with what is predicted by outflow models, where the Lyα is redshifted

through interaction with receding gas on the far side of the galaxy, and transmitted through approaching gas on the near side due to the line's kinematic redshift. Two particular types of outflow models are discussed here due to their apparent agreement with our results - the case where the outflow is in a coherent shell (Tenorio-Tagle et al., 1999; Dawson et al., 2002; Zheng & Miralda-Escude, 2010; Verhamme et al., 2006, 2008) and the case of a clumpy outflow (Neufeld, 1991; Hansen & Oh, 2006; Steidel et al., 2010).

Understanding our results in the context of an outflow is justified in that high-redshift LAEs are typically young (age $\simeq 10^7$ years) with vigorous star formation (e.g., Finkelstein et al., 2007, 2009; Pirzkal et al., 2007; Gawiser et al., 2007; Lai et al., 2008). Their typical star formation intensities are well above the threshold required to drive galactic winds (Malhotra et al., 2010). Similar winds are seen in nearby starbursting galaxies, with velocities of order 10^2-10^3 km s^{-1} (Heckman et al., 1990; Heckman, 2002), numbers that encompass our measured velocity offsets.

In the model with a single expanding shell, with a central monochromatic source (Verhamme et al. 2006, henceforth V06), the redshifted Lyα line is built up of photons that underwent one or more backscatterings off the expanding shell. The more scatterings the photon undergoes, the further it is redshifted, giving rise to the prominent red wing that is seen in the redshifted Lyα line. Photons that are emitted from the blue wing of the Lyα line in the part of the shell that is approaching the observer can give rise to the blue bump we see in LAE40844. See Figure 12 of V06 for a detailed description of photons escaping from an expanding shell.

For the parameter space examined in the V06 simulations, velocity offsets of a few 100 km s^{-1} are predicted for the redshifted Lyα line. The magnitude of

the Lyα velocity offset depends on the velocity of the expanding shell, the column density of neutral hydrogen and the Doppler parameter (see V06 for details on these parameters). Our velocity offsets of 125 km s^{-1} and 342 km s^{-1} appear to be at the low end of this range. When the blue bump is seen in these simulations it is offset from the redshifted Lyα line by $\sim$ 1000 km s^{-1}, in agreement with our measured offset in LAE40844 between the red and blue peaks of 796 km s^{-1}. Thus there is good general agreement between our observations and the V06 models, which have not been tuned specifically to fit our data. It seems likely that an expanding shell model could fit our data well with some adjustment of the input parameters. Additionally, while our total offset between the blue and red Lyα peaks in LAE40844 agree with the total offsets seen in their simulations, we find that $v_{blue\ peak} \sim$ -2$v_{red\ peak}$ in LAE40844. In V06 the velocity offset between these two peaks is nearly symmetric in the cases where both peaks are present and the expansion velocity of the shell is small ($<$ 200 km s^{-1}). Where the expansion velocity of the shell is large (300 -400 km s^{-1}) the blue peak is nearly -1/2 the velocity shift of the red peak. In either case, these predictions do not directly match our observations presented here. Further work is needed to understand the discrepancy between the velocities of the redshifted and blue-shifted peaks in models and observations. Deviations from spherical symmetry of the expanding shell model could help account for this difference, as was noted in Schaerer & Verhamme (2008).

These same authors further investigate their model in a later paper (Verhamme et al. 2008, henceforth V08) by applying it to actual observations. In V08, the 3D Lyα radiation transfer code was used to fit the the Lyα emission of Tapken's aforementioned LBGs with Lyα emission 2007) with redshifts in the range 2.8 –5. Varying model parameters including the Doppler parameter, V_{exp}, col-

umn density of N_{HI}, dust optical depth τ_a and the intrinsic EW and FWHM of the input Lyα line, 9 of the 11 LBGs investigated were found to have $V_{exp} \sim 150$ – 200 km s^{-1}. Two LBGs, similar to our LAE40844 in that they have a feature that can be considered a blue bump, can be fit wither with larger velocities, of order 300 – 400 km s^{-1} or a with a quasi-static medium with V_{exp} of order 10 – 25 km s^{-1} where the authors of V08 prefer the quasi-static explanation. We note that our results of $v_{offset} = 125$ and 342 km s^{-1} is fully consistent with the V08 results. However, we emphasize that our measurement is of the velocity offset or velocity shift between Lyα redshift and the systemic redshift as defined by [O III] whereas V06 and V08 are quantifying V_{exp}, or the velocity of the spherically expanding shell around the central Lyα source. We also note that it is possible that LAE40844 with it's blue bump and v_{offset} of 342 km s^{-1} may imply that the quasi-static interpretation favored in objects with secondary peaks may not be preferred over the higher velocity interpretation. This is something to be investigated further because, of course, this cannot be confirmed or refuted with only one new object.

Steidel et al. (2010, henceforth S10) consider outflows to be an important component of the mechanism that shapes the observed Lyα profile, but they prefer a scenario in which the structure and kinematics of the circum-galactic medium can produce our observed profiles, instead of relying on Lyα radiative transfer in an expanding shell to create the profiles we see. In the S10 scenario, a clumpy outflowing gas will allow some Lyα photons to escape from a galaxy producing the redshifted Lyα line we have observed. This same scenario is also capable of producing the faint 'blue bump' we have discussed in section 3.4. S10 find an average velocity offset of 445 km s^{-1} in a sample of 42 z $\simeq$ 2 - 3 LBGs with Lyα emission. The velocity offset measurement in this case was made with respect to the redshift defined by Hα emission. As is the case when we compare

our results to the Verhamme model, our velocity offsets of 125 km s^{-1} and 342 km s^{-1} for our observed LAEs are below these values. This conclusion includes consideration of the fact that S10 measures the centroid of a single function whereas we measure the peak of Ly-alpha through an asymmetric function composed of two Gauss functions; which inherently causes the S10 measurements to be higher. This causes a 10 – 15% difference in the velocity offsets calculated, and hence we stil find our velocity offset values to be lower than those in the S10 sample evn after this consideration.

At present, our sample of two z $\sim$ 3.1 LAEs reported in this paper does not allow us to distinguish between the expanding shell scenario or the S10 interpretation, as both are able to produce profiles and velocity offsets in reasonable agreement with our observations. Whichever of the scenarios discussed here (V06 or S10) is producing the observed velocity offsets, we emphasize that winds/outflows are important in either case.

The additional observational samples to which we can best compare our current results are z $\sim$ 3 LBGs. P01 and Shapley et al. (2003, henceforth S03) have both measured the velocity offset of the Lyα line from systemic in a population of z $\sim$ 3 LBGs. P01 find velocity offsets for the Lyα line of 200 - 1100 km s^{-1} in a sample of 13 LBGs that also show Lyα in emission. The velocity offset is measured compared to the redshift of nebular HII emission. S03 find a velocity offset of 360 km s^{-1} from a composite spectrum of 811 z $\sim$ 3 LBGs. The Lyα velocity offset measurement in S03 was made with respect to interstellar absorption lines. (Tapken et al., 2007) measured a velocity offset between LIS lines and Lyα in seven LBGs with Lyα emission at redshifts of 2.7 – 5. Including the 445 km s^{-1} offset measurement from the S10 sample discussed above, we note that in all cases our observed velocity offsets of 125 - 342 km s^{-1} in two z $\sim$ 3.1 LAEs are

at the low end of the values reported for the various LBG samples, although the velocity offset measurements have thus far been made via different methods.

An alternative explanation of the observed Lyα profiles, not based on galactic scale outflows, is that they arise through resonant scattering in the intergalactic gas surrounding an LAE. Zheng et al. (2010) have explored such a mechanism in detail for redshift $z = 5.7$. Their models can produce Lyα lines that qualitatively resemble our observations both in the line asymmetry and in the redshift of the Lyα line. However, some caution is needed in applying these results to our data set, given that the IGM density at redshift $z = 3.14$ is $\sim 1/4$ that at $z = 5.7$, and the ratio of neutral gas density between these two redshifts is still more extreme. Overall, we consider it more likely that winds play an important role in Lyα escape, given that winds are generically expected for galaxies with the high specific star formation rates typical of LAEs.

2.5.3 Implications of detected outflows

Detection and characterization of galaxy scale outflows at high redshift is important because these outflows have important consequences for the evolution of individual galaxies as well as the evolution of the IGM. Large scale galactic outflows are capable of driving materials out of the galaxy and may therefore contribute to metal enrichment of the IGM at high-z by introducing materials produced from starbursts into the IGM. In addition, galactic winds likely provide a crucial channel by which ionizing photons can escape from a galaxy (Steidel et al., 2001; Heckman et al., 2001). This has important implications for the contribution of high-z galaxies to the reionization of the IGM. In terms of shaping an individual galaxy, superwinds are responsible for driving dust from a starbursting

galaxy (Ferrara et al., 1991; Heckman et al., 2000; Shapley et al., 2001; Bianchi & Ferrara, 2005) and the mass loss from a galaxy due to an outflow may be capable of suppressing star formation (Somerville & Primack, 1999; Heckman, 2002). While our work presented in this paper has now demonstrated that that our sample of two Lyα selected galaxies at z $\sim$ 3.1 are driving winds, further characterization of these winds from a larger sample will help us understand and test some of the broader implications of winds detailed above.

The observed velocity offsets between the Lyα line and systemic velocity also have important implications for Lyα based tests of reionization (Malhotra & Rhoads, 2004; Santos, 2004; Malhotra & Rhoads, 2006; Dijkstra & Wyithe, 2010). In particular, the ionized volume test proposed by Malhotra & Rhoads (2006) (hereafter MR06) is much more sensitive if Δv (Lyα peak vs. systemic) is typically small. That test works by noting that substantial transmission of Lyα through a generally neutral IGM requires a locally ionized region around each observed LAE. The product of the bubble volume V and the LAE number density n is then a filling factor of ionized gas, from which the volume fraction of the ionized phase is $\approx 1 - exp(-nV)$ (MR06). The relevant bubble volume V is sensitive to the velocity offset, since Lyα photons that are already redshifted before leaving the emitting galaxy are less strongly scattered by the damping wing of neutral hydrogen in the surrounding intergalactic gas. The effect is explored in detail in Figure 1 of MR06. Replacing the range $0 \leq \Delta$ v $\leq$ 350 km s^{-1}from that paper with our average measurement, Δ v $\approx$ 235 km s^{-1}, would narrow the range of permitted volume ionized fractions from the 20% – 50% range derived in MR06 to $\sim$ 35 – 40%. While this discussion is subject to refinement as the sample of LAEs with a measured velocity offset grows, it shows the importance of measuring Δ v for studying reionization with Lyα lines.

Finally, even at redshifts where the IGM is predominantly ionized and affects the Lyα line only through the Lyα forest, our systemic redshift measurements have important implications. Several groups have shown that the observed Lyα luminosity function is largely unchanged from $z \approx 3$ to $z \approx 6$ (e.g., Dawson et al., 2004; Stern et al., 2005; Ouchi et al., 2008; Cassata et al., 2010). Recently, Cassata et al. (2010) have combined this observation with the expected optical depth evolution of the Lyα forest (Madau, 1995; Fan et al., 2008) to infer that the Lyα luminosity function is in fact evolving towards higher luminosities at higher redshifts. The key assumption in this argument is that the line emitted by the LAE is symmetric and centered on the systemic velocity, so that the fraction scattered by the IGM approaches 50% by $z \approx 6$. This implies that the fraction of Lyα flux observed would decline by a factor of ≈ 0.6 between redshift $z \approx 3$ and $z \approx 6$. However, for the two objects where we observe [O III], we know that only those photons observed blueward of the systemic velocity would be subject to additional Lyα forest absorption at higher redshift. For LAE40844, the blue bump would be progressively obscured by the forest at higher redshift, resulting in a flux loss of a factor $\approx 3.0/4.0 = 0.75$ or so at most. For LAE27878, there is no significant flux blueward of the systemic velocity, and the fraction of its Lyα emission that we can see should remain nearly unchanged from $z = 3.1$ until the IGM neutral fraction becomes so large that the red damping wing of the IGM becomes optically thick— i.e., until we reach the central stages of reionization.

Presently, our sample consists of two galaxies, each of which has a ratio of blue flux to red flux $\leq 1/3.0 \approx 0.33$. We can estimate the chance of such an occurrence under the assumption of Cassata et al (i.e., that 50% of the flux is emitted blueward of the systemic velocity). McDonald et al (2000) give probability distributions for transmission through the Lyman α forest at $z = 3.00$ and $z = 3.89$.

Interpolating to our redshift, $z = 3.14$, we estimate a chance of 24% for each observed galaxy to show $\leq 30\%$ transmission through the IGM. The likelihood that we would measure a ratio of blue to red flux that is $\leq 30\%$ in two objects, assuming an intrinsic ratio of 1:1, is then $0.24^2 = 0.06$. So, our present results disfavor this assumption of an intrinsic 1:1 ratio of blue:red flux, suggesting that the luminosity function evolution inferred in Cassata et al. (2010) is a consequence of their implicit assumption $\Delta v = 0$ and not a strong conclusion about the true evolution of Lyα galaxy populations. For now, this is a 2σ result. Observations of a few more Lyα emitters with systemic velocity measurements could resolve this question firmly.

2.6 Conclusions

We have detected [O III] emission in two Lyα selected galaxies at $z \sim 3.1$ using the new NIR spectrograph LUCIFER on the LBT. This is a successful demonstration that the [O III] line can be detected in high-z Lyα selected galaxies and that this line can be used to investigate the characteristics of these galaxies.

In both LAEs we measured a velocity offset between the Lyα emission and the systemic redshift of the galaxy as defined by the [O III] emission. These velocity offsets range from 125 - 342 km s^{-1}. We find that these velocity offsets and the observed profile of the Lyα line both indicate that our measurements are the result of Lyα emission emerging in the presence of a galactic outflow. In addition we have measured Lyα flux blueward of systemic in a 'blue bump' in one of our objects. This is another phenomenon one can expect when observing Lyα emission in the presence of an outflow. We find that a scenario in which radiative transfer effects of Lyα emission emerging from an expanding shell (V06) is able to reproduce reasonably well our observed Lyα profiles and velocity offsets. We

also find that a scenario in which Lyα photons escape from a circumgalactic gas as described by Steidel et al. (2010) is capable of reproducing our results reasonably well.

ACKNOWLEDGEMENTS

We thank the LUCIFER Instrument team and the LUCIFER SDT team for their hard work and for exciting science with this new instrument. This work was supported by NSF grant AST-0808165. In addition we thank the referee for insightful comments that have improved this paper.A larger sample of measured velocity offsets will better constrain the range of velocity offsets we can expect for z $\sim$ 3.1 LAEs and will allow for better understanding of how these offsets compare to those observed in Lyman-break selected samples. These comparisons should shed light on the relationship between crucial characteristics like galaxy mass, star formation rates and the magnitude of the observed velocity offsets. Finally, larger samples of velocity offsets will further improve our ability to infer constraints on cosmological reionization from observations of Lyα galaxies at high redshifts.

Chapter 3

GALACTIC WINDS AND STELLAR POPULATIONS IN LYMAN-ALPHA EMITTING GALAXIES AT Z $\sim$ 3.1

3.1 Abstract

We present a sample of 33 spectroscopically confirmed z $\sim$ 3.1 Lyα emitting galaxies (LAEs) in the COSMOS field. We present detailed constraints on the physical characteristics of the entire LAE sample from spectral energy distribution (SED) fitting. These characteristics include mass, age, star-formation history, dust content and metallicity. We also detail a novel approach to account for nebular emission lines in the SED fitting process - wherein our models can predict the strength of the [O III] line in an LAE spectrum. We are in an excellent position to study the success of this prediction because we can compare the model predictions to our actual NIR observations both in observed galaxies that have [O III] detections and those that do not. So far our approach has been successful, with agreement between our model [O III] lines and observed [O III] lines between $\sim$ 3 – 40%. We find a median stellar mass of 1.5×10^9 $M_\odot$ and a median star formation rate weighted stellar population age of 4.8×10^8 years. We also report on a new spectroscopic detection of the [O III] 5008.24 Å line in one of these LAEs. This detection is in addition to two [O III] detections in two z $\sim$ 3.1 LAEs we have reported on previously (McLinden et al., 2011). In addition, this paper details the narrowband survey we conducted to detect the entire LAE sample, the optical spectroscopy data we collected to confirm the nature of these LAEs, and the near-infrared (NIR) spectroscopic observations that were made that led to this

additional [O III] detection. We once again quantify the velocity offset between the [O III] and Lyα lines in the galaxy with the [O III] detection, finding that in the newest object, the Lyα line is shifted 52 km s^{-1} redward of the [O III] line that defines the systemic velocity of the galaxy.

3.2 Introduction

High redshift Lyman alpha emitting galaxies (LAEs) are now routinely detected via narrowband detection methods (e.g. Cowie & Hu, 1998, Malhotra & Rhoads, 2002, 2004, Ouchi et al. 2003, Gawiser et al. 2006, and many others). Now that samples of these galaxies can be more easily compiled at a variety of redshifts, attention has turned to deriving the physical characteristics of these galaxies from fitting Spectral Energy Distributions (SEDs) to the observed photometry of these galaxies (Gawiser et al., 2006, 2007; Pirzkal et al., 2007; Nilsson et al., 2007, 2011; Finkelstein et al., 2007, 2008, 2009, 2011b; Lai et al., 2007, 2008; Ono et al., 2010; Acquaviva et al., 2012).

The majority of early work in SED fitting relied on deriving average LAE characteristics from stacked LAE samples, but stacked analyses may not reveal the full distribution of LAE characteristics. Most efforts to date have found LAEs to be largely young or of intermediate ages and having characteristically small masses (Pirzkal et al., 2007; Gawiser et al., 2007; Finkelstein et al., 2009; Cowie et al., 2011), but SED fitting procedures tend to vary from author to author, making direct comparisons of derived characteristics difficult from sample to sample. In addition, SED fitting procedures for starbursting galaxies have been evolving recently to account for contamination of observed photometry from rest-frame nebular emission lines. Schaerer & de Barros (2009) and others have demonstrated

that failure to include these lines, produced from hot gas in star forming regions, can drastically alter the ages and masses derived from SED fitting.

In this paper we present a new and simple way to account for nebular emission during SED fitting, specifically in z $\sim$ 3.1 LAEs. We will demonstrate the efficacy of this new approach on a sample of 33 spectroscopically confirmed z $\sim$ 3.1 LAEs that we discovered from a narrowband survey of the COSMOS field (Capak et al., 2007). The technique we outline in this paper allows us to predict the strength of the [O III] nebular emission line, which we can compare to the NIR detections and upper limits we have made of this line in six z $\sim$ 3.1 LAEs.

In Section 3.3 we present the extensive observations that form the foundation of this paper, including a narrowband survey to find LAE candidates, optical spectroscopy to confirm LAE candidates and NIR spectroscopy to look for rest-frame optical nebular emission lines in these LAEs. We also present our data reduction techniques in this section. In Section 3.4 we present our results from optical and NIR spectroscopy, including a new [O III] measurement in one new LAE and the subsequent velocity offset between [O III] and Lyα that we measure in this object. Section 3.5 outlines our methods for SED fitting, including the introduction of a new method to account for nebular emission lines in the SED fitting process. We present our results from SED fitting in Section 3.6. Finally, in Section 3.7 we discuss the success of our SED fitting process to match our observations of the [O III] line in LAEs. We also compare our SED results to those presented by other authors.

Where relevant, we adopt the standard cosmological parameters $H_0 = 70$ km s^{-1} Mpc^{-1}, $\Omega_m = 0.3$, and $\Omega_\Lambda = 0.7$ (Spergel et al., 2007). Also we use the following vacuum wavelengths, 1215.67 Å for Lyα, 3727.092/3729.875 Å for [O II],

4862.683 Å for Hβ and 4960.295/5008.240 for [O III] from the Atomic Line List v2.04[1]. All quoted magnitudes are AB magnitudes.

3.3 Observations and Data

3.3.1 Narrowband survey

We collected data for our narrowband (NB) survey in 2007 (PI Finkelstein) and 2009 (PI McLinden) using the 90-inch Bok telescope with the 90Prime Camera (Williams et al., 2004) at Steward Observatory. The survey was completed in the COSMOS field centered at R.A. 10:00:28.6 and decl. +02:12:21.0 (J2000) (Capak et al., 2007). The NB data was collected on UT February 21 and 22 in 2007. The rest of the data, described below, was collected on UT February 27, 28 and March 1 2009. We used the KPNO [O III] filter, centered at 5025 Å, with a narrow bandpass of 55Å, to select Lyα emission from z = 3.11 – 3.16. The 90Prime instrument was originally outfitted with a 1 deg^2 field of view from four 4096 pixel x 4096 pixel CCDs. This was the instrument setup for our 2007 observations. Due to instrument failure however, our 2009 observations were made with only a single 4064 pixel x 4064 pixel CCD, providing less coverage and therefore less depth than we had initially anticipated. The pixel scale for 90Prime is 0.45″ pixel^{-1}.

To reduce the narrowband data we used the MSCRED package in IRAF. The data reduction process included bias subtraction, overscan subtraction, flatfielding and cross talk correction using CCDPROC. We applied astrometry corrections using the USNO B1.0 catalog with the IRAF tasks MSCTPEAK and MSCCMATCH. Cosmic ray rejection proceeded using the JMCCREJ algorithm

[1] http://www.pa.uky.edu/∼peter/atomic/index.html

developed by Rhoads (2000). Complete bad pixel masks, including manually added satellite trails, were created and applied to each frame before stacking. MSCIMAGE was used to resample individual exposures onto a common pixel grid. Scaling was determined using MSCIMATCH. Before stacking the images, we applied skyflats in CCDPROC and did a sky subtraction using MSCSKYSUB. Finally, we used MSCSTACK to stack each individual frame into a single final exposure. A total of 50 frames, representing 16.67 hours of integration, were stacked to create this final 1.96 deg^2 image. We find a 5σ depth of 23.2 magnitudes in a 3″ diameter aperture, which corresponds to a line flux lower limit of $\sim 1.2 \times 10^{-16}$ erg cm^{-2} s^{-1} for pure emission line sources. The point spread function FWHM in our final stack is $\sim$ 3.62 pixels, corresponding to 1.63″.

3.3.2 Broadband data for Candidate Selection

Our narrowband survey is complemented by a plethora of publicly available data in the COSMOS field. In particular, we used u* and g′ band images from the NASA/IPAC archive[2] in concert with our narrowband survey to select LAEs as described in Section 3.3.3 below. The u* band images come from the MegaPrime instrument (Boulade et al., 2003) on the 3.6 m Canada-France-Hawaii Telescope. The u* images have a 5σ depth in a 3″ aperture of 26.4 (Capak et al., 2007). The u* filter is centered at 3798 Å and has a bandpass of 720 Å. The g′ images come from Suprime-Cam on the 8.3 m Subaru telescope. The 5σ depth in a 3″ aperture for the g′ images is 27.0 (Capak et al., 2007). The g′ filter is centered at 4780 Å and has a bandpass of 1265 Å. The filter transmission curves for the u*, g′, and narrowband are shown in Figure 3.1. Note that one of the wide broadband filters, the g′ filter, encompasses the [O III] narrowband and the other

[2] http://irsa.ipac.caltech.edu/data/COSMOS/datasets.html

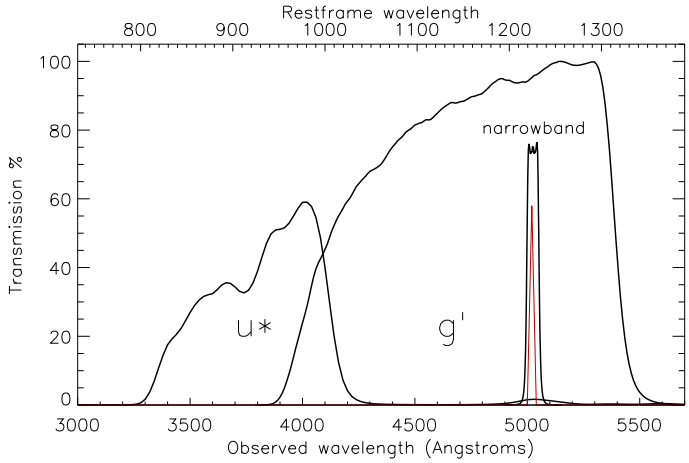

Figure 3.1 Transmission curves for the u*, g′ and narrowband filters. The CFHT u* filter is centered at 3798 Å(dλ = 720Å), the Subaru g′ filter is centered at 4780 Å(dλ = 1265Å), and the KPNO [O III] narrowband filter (λ = 5025 Å, dλ = 720Å) used for our narrowband survey lies within the g′ filter. Also shown is an mock Lyα line (not to scale) in red, inside the narrowband filter.

broadband filter, the u* band, is fully blue-ward of the narrowband filter and Lyα line. This filter setup is essential for selection of LAEs at z $\sim$ 3.1 via narrowband imaging because an LAE ought to have an excess of flux in the narrowband when compared to the g′ band, due to the location of the Lyα line. The LAE spectrum should also be attenuated blue-ward of the Lyα line due to Lyα forest absorption. Our use of the u* and g′ filters with our narrowband data allows us to detect both this flux excess and attenuation as detailed in Section 3.3.3 below.

3.3.3 LAE Candidate Selection via SExtractor

We selected LAE candidates based on a combination of their narrowband and broadband photometry. To do this we used SExtractor (Bertin & Arnouts, 1996) to detect objects and extract their corresponding photometry. We used aper-

ture photometry measurements (FLUX_APER) from SExtractor, in a 3″ diameter aperture. Objects were extracted from the central 1.44 deg^2 of our narrowband survey, avoiding some of the shallower edges of our survey.

We extract fluxes for all objects detected in the narrowband image by running SExtractor in dual-image mode. In dual-image mode, our narrowband image was the 'detection' image and a second image, either the narrowband, u^* or g' image, was 'the measurement' image. The 'detection' image determines where objects are found, the 'measurement' image is used to measure fluxes at those locations. In order to run SExtractor in dual image mode, both images must have the same pixel scale. To make this possible, we registered the u^* and g' images to the narrowband image with the IRAF tasks WCSMAP and GEOTRAN, where WCSMAP computes a spatial transformation function from the WCS information of the images and GEOTRAN actually performs this geometric transformation. This process changes the resolution of broadband images from their native resolution of 0.15″ pixel^{-1} to the 0.45″ pixel^{-1} resolution of the narrowband image. Such a transformation means measurements can be made in the exact same pixels from image to image. The NASA/IPAC COSMOS archive also includes maps of image RMS for all of our broadbands, so we used these as WEIGHT_IMAGES in SExtractor with the SExtractor parameter WEIGHT_TYPE set to MAP_RMS. We created weight maps for our narrowband image using the CHECK_IMAGE feature of SExtractor with the CHECKIMAGE_TYPE parameter set to BACKGROUND_RMS.

The final set of confirmed LAEs presented in this paper is a compilation of objects from multiple LAE selections. Our earliest selection of LAEs was performed on an a preliminary reduction of our narrowband data that only included the 2007 data. Later selections were performed on reductions of the narrowband

data that contained the full 16.67 hours of data. Our selection criteria have also evolved since the preliminary extraction, as we have narrowed in on criteria more likely to yield confirmations in optical spectroscopy given our specific combination of very deep broadband images (u^*, g') and our shallower narrowband image. In addition, we re-reduced the narrowband data multiple times to try to improve the quality of the final product. Essentially, our basic LAE selection criteria are:

$$\frac{f_{NB}}{\delta f_{NB}} \geq 5 \text{ and } \frac{f_g}{\delta f_g} \geq 3 \tag{3.1}$$

$$\frac{f_{NB}}{f_g} \geq 2 \tag{3.2}$$

$$\frac{f_{NB} - f_g}{\sqrt{\delta f_{NB}^2 + \delta f_g^2}} \geq 4 \tag{3.3}$$

$$f_u \leq 10^{-4/5} f_g + 2\delta f_u \tag{3.4}$$

where f_u is flux in the u^* band, f_g is flux in the g^+ band, f_{NB} is flux in the narrowband band, δf_u is flux error in the u^* band, δf_g is flux error in the g^+ band, and δf_{NB} is flux error in the narrowband. In other words, to be an LAE candidate, an object must (1) be detected at the 5σ level in the narrowband and at the 3σ level in the g band, (2) have an excess of flux density in the narrowband compared to the g band (corresponding to rest-frame equivalent width $\geq$ 15.7 Å) (3) that flux excess must be significant at the 4σ level, and (4) the flux blueward of the Lyα line must be attenuated in a manner congruent with expected Lyα forest absorption. These criteria are based on those developed by Rhoads & Malhotra (2001). We note that the requirement of a detection in the g' band is not a requirement that there be continuum detection, as the presence of the Lyα line would be sufficient to cause a detection in the g' band at this level. 12 of the objects in sample presented in this paper were initially selected with these criteria (labeled

as selection 1 in Table 3.1). Three additional (unique) objects in the sample were selected with a less stringent fourth criterion, i.e. $f_u \leq 10^{-4/5} f_g + 3\delta f_u$ (selection 2). 14 more (unique) LAEs in the sample were selected with an also less stringent fourth criterion, $m_u - m_g > 0.5$ (selection 3). Because the u* band data are so much deeper than our narrowband data we found these less stringent requirements on the suppression of the u band flux to be useful.

In addition to the traditional narrowband selection criteria detailed above, we also experimented with finding LAEs using a broadband detection as the initial requirement. This was possible again because the publicly available broadband data were so much deeper than our narrowband survey. Three of the objects in our current sample were selected this way (selection 4). The criteria in this case are as follows:

$$\frac{f_g}{\delta f_g} \geq 5 \tag{3.5}$$

$$\frac{f_{NB}}{f_g} \geq 1.445 \tag{3.6}$$

$$\frac{f_{NB} - f_g}{\sqrt{\delta f_{NB}^2 + \delta f_g^2}} \geq 2 \tag{3.7}$$

$$\frac{f_u}{f_g} < 10^{-2/5} \tag{3.8}$$

In other words, the first requirement is a g′ detection, not a narrowband detection as is the case for our narrowband detection criteria. In addition, the g′ detection is required at a higher significance (5σ) than the g′ requirements in the narrowband criteria above. Because we are requiring a g′ detection as the preliminary criterion for these objects, we re-ran SExtractor, still in dual-image mode, but now with the g′ image as the 'detection' image, and either the g′, u*, or

narrowband image as the 'measurement' image. We are able to require a secure g′ detection because the g′ image is significantly deeper than our narrowband image. Meaning that strong emission line objects from the narrowband should be well detected in the g′ that encompasses the narrowband. The second criterion still requires that an excess of flux be present in the narrowband compared to the g-band, but the minimum magnitude of this excess is lowered, and the significance of the excess is also lowered (from 4σ to 2σ). Essentially, this only requires an equivalent width of ≥ 26 Å. Finally the u* flux must still be less than the g′ flux, but the difference need not be as large, given the depth of the u* band.

While the sample of LAEs discussed in this paper comes from a compilation of objects selected from multiple data reductions and different selection iterations, we emphasize that each LAE discussed here has been confirmed spectroscopically (as discussed in Section 3.3.4). The compilation of multiple extractions is simply a result of the long-term nature of this project and an interest in improving our selection process and results.

3.3.4 Optical spectroscopy

We obtained optical spectroscopy of our LAE candidates using the Hectospec multi-fiber spectrograph (Fabricant et al., 2005) at the 6.5m MMT Observatory (a joint facility of the Smithsonian Astrophysical Observatory and the University of Arizona) in 2009 and 2011. Hectospec has 300 optical fibers, a 1 deg^2 field of view, and spectral coverage from 3650 - 9200 Å. We used the 270 lines per mm grating for our observations. This setup has a blaze wavelength of $\sim$ 5200 Å and dispersion of 1.21 Å pixel^{-1}. The resolution of the instrument is $\sim$ 6 Å. Optical spectroscopy allows us the confirm the presence of the Lyα line in the candidate's spectrum, thereby assuring us the object is indeed an LAE at z $\sim$ 3.1.

Object	Flux_{NB}	Flux_{g}	Flux_{u}	EW (rest-frame)	Selection
LAE_J100049.56+021647.1	1.4e-29 ± 2.8e-30	6.2e-30 ± 5.2e-31	1.6e-30 ± 2.8e-31	19. ± 7.	4
LAE_J095859.33+014522.0	7.1e-30 ± 1.5e-30	3.7e-30 ± 4.9e-31	1.3e-30 ± 4.7e-31	14. ± 7.	4
LAE_J100212.99+020137.7	1.6e-29 ± 2.3e-30	2.9e-30 ± 5.0e-31	1.4e-30 ± 3.7e-31	78. ± 23.	3
LAE_J095929.41+020323.5 (LAE6559)	1.5e-29 ± 2.3e-30	2.1e-30 ± 4.3e-31	6.7e-31 ± 4.3e-31	121. ± 43.	1,2,3
LAE_J095944.02+015618.8	1.3e-29 ± 2.0e-30	2.1e-30 ± 5.3e-31	2.9e-31 ± 6.7e-31	89. ± 35.	3
LAE_J095930.52+015611.0 (LAE7745)	3.4e-29 ± 2.0e-30	5.0e-30 ± 4.7e-31	1.2e-30 ± 4.5e-31	111. ± 17.	1,3
LAE_J100217.05+015531.7	1.4e-29 ± 2.2e-30	4.0e-30 ± 6.2e-31	2.1e-30 ± 3.9e-31	37. ± 11.	3
LAE_J100157.87+021450.0	1.3e-29 ± 2.3e-30	1.8e-30 ± 5.9e-31	1.8e-31 ± 7.9e-31	131. ± 70.	3
LAE_J100124.36+021920.8 (LAE40844)	6.8e-29 ± 3.7e-30	1.3e-29 ± 7.3e-31	2.2e-30 ± 7.4e-31	78. ± 8.	1,2
LAE_J095847.81+021218.2	1.7e-29 ± 2.6e-30	4.0e-30 ± 1.9e-31	9.5e-31 ± 5.4e-31	55. ± 11.	1
LAE_J095904.93+015355.4	9.9e-30 ± 1.4e-30	1.4e-30 ± 1.1e-31	2.5e-31 ± 6.9e-31	121. ± 26.	1
LAE_J095910.90+020631.6 (LAE14310)	3.4e-29 ± 3.8e-30	5.8e-30 ± 7.3e-31	2.4e-30 ± 7.2e-31	89. ± 20.	1,2
LAE_J095921.06+022143.4	1.1e-29 ± 1.6e-30	2.5e-30 ± 1.5e-31	7.4e-31 ± 5.2e-31	57. ± 11.	1
LAE_J095948.47+022420.8	1.1e-29 ± 1.5e-30	1.6e-30 ± 1.1e-31	2.5e-72 ± 1.0e-32	114. ± 22.	1,2
LAE_J100019.07+022523.9 (LAE27878)	1.7e-29 ± 2.5e-30	2.4e-30 ± 4.6e-31	8.8e-31 ± 5.1e-31	118. ± 40.	1,2
LAE_J100100.35+022834.7	2.5e-29 ± 2.5e-30	4.6e-30 ± 1.4e-31	8.9e-31 ± 6.6e-31	76. ± 10.	1
LAE_J100146.04+022949.0	9.0e-30 ± 1.4e-30	1.6e-30 ± 1.1e-31	7.0e-31 ± 4.1e-31	79. ± 17.	1
LAE_J095843.11+020312.3	1.7e-29 ± 2.2e-30	3.6e-30 ± 1.4e-31	1.3e-30 ± 3.9e-31	63. ± 11.	1
LAE_J100128.11+015804.7	1.4e-29 ± 2.1e-30	3.1e-30 ± 4.0e-31	1.6e-31 ± 1.3e-30	58. ± 15.	2
LAE_J100017.84+022506.1 (LAE27910)	1.6e-29 ± 2.2e-30	3.0e-30 ± 4.2e-31	9.4e-31 ± 4.5e-31	73. ± 19.	2
LAE_J095839.92+023531.3	1.5e-29 ± 2.5e-30	4.3e-30 ± 1.7e-31	1.6e-30 ± 5.3e-31	40. ± 9.	1
LAE_J095838.90+015858.2	1.1e-29 ± 1.8e-30	7.7e-31 ± 9.3e-32	3.5e-31 ± 4.8e-31	452. ± 198.	1,2
LAE_J100020.70+022927.0	1.1e-29 ± 2.2e-30	1.8e-30 ± 4.1e-31	1.4e-30 ± 4.0e-31	98. ± 39.	2
LAE_J095812.33+014737.6	1.1e-29 ± 1.8e-30	5.9e-30 ± 4.8e-31	2.2e-30 ± 5.7e-31	13. ± 5.	4
LAE_J095920.42+013917.1	1.1e-29 ± 1.6e-30	5.8e-30 ± 5.4e-31	2.0e-30 ± 5.6e-31	13. ± 4.	4
LAE_J095846.72+013706.1	1.2e-29 ± 1.8e-30	2.4e-30 ± 7.2e-31	4.1e-31 ± 1.1e-30	66. ± 29.	3
LAE_J095923.79+013045.6	1.4e-29 ± 2.0e-30	1.6e-30 ± 6.1e-31	2.5e-31 ± 1.3e-30	154. ± 94.	3
LAE_J100213.17+013226.8	1.2e-29 ± 2.3e-30	1.8e-30 ± 6.2e-31	4.1e-31 ± 8.7e-31	105. ± 57.	3
LAE_J095838.94+014107.9	1.0e-29 ± 1.7e-30	2.1e-30 ± 4.5e-31	7.2e-31 ± 7.5e-31	69. ± 25.	3
LAE_J095834.43+013845.6	2.0e-29 ± 1.9e-30	2.2e-30 ± 4.6e-31	9.2e-31 ± 6.3e-31	182. ± 67.	3
LAE_J100302.10+022406.7	3.9e-29 ± 3.9e-30	3.9e-30 ± 4.6e-31	2.0e-30 ± 5.2e-31	206. ± 50.	3
LAE_J100157.45+013556.2	2.1e-29 ± 1.9e-30	3.9e-30 ± 7.8e-31	1.7e-30 ± 6.8e-31	75. ± 22.	3
LAE_J100152.14+013533.2	1.4e-29 ± 1.9e-30	4.1e-30 ± 7.7e-31	1.4e-30 ± 6.8e-31	36. ± 11.	3

Table 3.1 SExtractor photometry of confirmed LAEs - Flux_{NB} is flux in [O III] Narrowband, Flux_{g} flux in g′, and Flux_{u} is flux in u*, All fluxes are in units erg s^{-1} cm^{-2} Hz^{-1}. Rest-frame equivalent width has units Å.

For instance, we rule out [O II] emitters at z $\sim$ 0.34 and [O III] emitters at z $\sim$ 0 by looking for other optical lines that would be present in such cases. Also, the presence of high ionization lines, such as CIV, also help us distinguish between starforming galaxies at z $\sim$ 3 and spectra that are likely AGN. Our initial Hectospec data was obtained on UT February 16 and 21 and April 26 and 27, 2009 (PI Malhotra). Our reductions for the 2009 data combine 120 minutes of observations per object. Our newest LAE candidates were observed on March 25th and 26th, 2011 (PI McLinden). Our reductions for the 2011 data combine either 150 or 330 minutes of observations for each object.

3.3.4.1 Reduction of Optical Spectra

We reduced the optical spectra of our LAE candidates observed in 2011 using HSRED, an IDL-based reduction package written by Richard Cool.[3] HSRED is mostly based on SPECROAD, SAO's Hectospec reduction package. The reduction process bias corrects and flatfields the fibers and removes cosmic rays. Traces of the 300 fibers are made from the domeflats and a wavelength solution is derived from a HeNeAr arc lamp exposure using a 5th order Legendre polynomial. Accurate sky models are determined from dedicated sky fibers included in each observation. Sky subtracted 1-D spectra are extracted. The average residual from wavelength calibration is $\sim$ 0.2 Å. Median combined spectra are created by combining multiple observations that have the same instrument/fiber setup. See Papovich et al. (2006) for more detail on each of these steps.

We chose to flux calibrate our optical spectra outside the reduction pipeline. We scaled a G8III spectral type Pickles model (Pickles, 1998) spectrum to match the V $\sim$ 5.36 magnitude of our observed G8III spectral type standard star. Before

[3] http://astro.princton.edu/ rcool/hsred.

scaling, the Pickles model has zero magnitude in Vega magnitudes. We divided the scaled down Pickles spectrum by the standard star's spectrum in counts to create a sensitivity curve. We then multiplied each reduced, uncalibrated optical spectrum (in counts) by this sensitivity curve to get a flux calibrated spectrum in ergs/s/cm^2/Å. We present 18 objects in our sample that were observed, reduced and confirmed in 2011.

The LAEs observed with Hectospec in 2009 were previously reduced with the External SPECROAD[4] pipeline developed by Juan Cabanela, as mentioned previously in McLinden et al. (2011). ESPECROAD applies bias, dark and flat field corrections and wavelength calibration (using He-Ne-Ar arc lamps).

Our 2009 data was not flux calibrated, but we were able to use LAEs that were observed both in 2011 and 2009 to go back and flux calibrate the 2009 data. Four objects were observed in both years, and we chose to use the two brightest objects, with the highest signal to noise ratios, to derive a scale factor that would appropriately calibrate the 2009 data. To derive this scale factor we compared the Lyα line flux in these two bright LAEs, in the flux calibrated (2011) data and the non-flux calibrated (2009) data. The line flux in the uncalibrated case is in units of counts $\cdot$ Å. The line flux in the calibrated spectra are in units erg s^{-1} cm^{-2}. The scale factor is then this calibrated line flux divided by the uncalibrated line flux, yielding a constant with units erg s^{-1} cm^{-2} Å^{-1} counts^{-1}. Therefore, when this constant is multiplied by an uncalibrated spectrum with units counts, the result is an appropriately scaled spectrum with units erg s^{-1} cm^{-2} Å^{-1}. The constants from the brightest two LAEs, derived as described above, were averaged. The averaged value was then used to flux calibrate the rest of the 2009 data. This procedure

[4]http://iparrizar.mnstate.edu/∼juan/research/ESPECROAD/index.php

was used to flux calibrate a total of 15 LAEs from 2009, amongst our larger sample of 33 confirmed LAEs.

3.3.5 Construction of the final sample

Combining the object selection methods and spectroscopic confirmations discussed above, we have at our disposal a sample of 33 LAEs. The photometry (from SExtractor) for these 33 confirmed LAEs is shown in Table 3.1. This total does not include two Lyα-emitting objects (LAE25972, LAE42795) that were removed because they are likely AGN (see Section3.4.3). The AGN are excluded from discussion of our SED fitting results (Section 3.5) as their physical characteristics cannot be derived from comparison to star-forming SED models. We note that eight of our 33 LAEs have poor agreement between measured spectroscopic and photometric Lyα line fluxes; they are not removed from the sample but are labeled as such in Table 3.2. An additional five of these 33 LAEs are determined to have possible multiple components and/or morphology indicative of possible interacting sources(Malhotra et al., 2012). This was determined by finding objects that had multiple matches within $2''$ in the COSMOS ACS Catalog (Leauthaud et al., 2007). We confirmed the multi-component morphology with visual inspection of the corresponding HST ACS F814W images (Koekemoer et al., 2007; Massey et al., 2010). Note that fitting SED models to photometry that may be from multiple sources can certainly affect what characteristics are derived from SED fitting results. These five objects are also labeled in Table 3.2.

3.3.6 New NIR spectroscopy

We observed five additional, unique $z \sim 3.1$ Lyα emitting objects from our sample of LAEs in the near-infrared (NIR). We made our NIR observations using

LUCIFER (LBT NIR Spectrograph Utility with Camera and Integral-Field Unit for Extragalactic Research) on the 8.4m LBT (Seifert et al., 2003; Ageorges et al., 2010) and using NIRSPEC on the 10m Keck II telescope (McLean et al., 1998). These observations are in addition to the three LAEs previously observed in the NIR with LUCIFER, as detailed in McLinden et al (2011, henceforth Mc11). The previously observed LAEs in Mc11 were LAE40844, LAE27878, and LAE14310. LAE40844 and LAE27878 yielded detections of the [O III] line. Of the five new observations, two yielded [O III] detections, but one of these [O III]-detected objects was one of the objects removed as likely an AGN (see Section 3.4.3). The other new detection, henceforth LAE7745, appears to be a typical star-forming LAE, and will be discussed in more detail below. No emission lines were detected in the other three observed objects, henceforth LAE25972, LAE6559 and LAE27910.

3.3.7 New LUICFER data

We used the longslit mode of LUCIFER for two of our newest observations in the same manner as our previous LUCIFER observations - with a 1″ slit utilizing the H+K grating with 200 lines/mm and the N1.8 camera. The image scale of the N1.8 camera is 0.25″/pixel. LAE25972 was observed over ten 120-second frames. LAE7745 and LAE6559 were observed over seven 240-second frames.

3.3.7.1 2D Reduction of NIR LUCIFER spectra

We reduced the 2-D LUCIFER spectra using NIRSPEC_REDUCE, a package of IDL scripts written by Becker et al. (2006). NIRSPEC_REDUCE follows the methodology of Kelson (2003) for optimal sky subtraction. In this technique the

sky subtraction is performed by sub-sampling the raw (distortion uncorrected) spectra thereby improving the sky-subtraction significantly. We customized the scripts to accommodate LUCIFER data. The first three scripts in the reduction process, NIRSPEC_SLITGRID, NIRSPEC_WAVEGRID and NIRSPEC _FLAT-FIXER were all modified to deal with LUCIFER's 2048 x 2048 pixel array as opposed to NIRSPEC's 1024 x 1024 pixel array. NIRSPEC_SLITGRID transforms x and y-coordinates to coordinates of slit position and NIR- SPEC_WAVEGRID transforms x and y-coordinates to coordinates of uncalibrated wavelength. NIR-SPEC_FLATFIXER creates a median combined normalized flat and a separate file containing the variance in the median combined normalized flat. We used three 5 second Halo2 flats for each reduction. Before reduction with these three scripts, all LUCIFER spectra were rotated by 270 degrees using the IMROT task in IRAF so that dispersion was in the y-direction and wavelength increased with increasing y.

The final script in the process, the one that actually performs the sky subtraction, LONGSLIT_REDUCE, wasn't directly modified. Parameters for a specific instrument can be supplied to this script via an external LONGSLIT _REDUCE.inc file. Therefore, appropriate values for LUCIFER for information such as array size, gain, slit width, observatory location etc. can be easily supplied without modifying the actual script. As noted in the README file supplied with the NIRSPEC_REDUCE package, to subtract an accurate sky model this program processes a raw frame, locates and masks objects, iteratively fits the sky in a single frame to get sky levels and iteratively fits the sky in a differenced frame and then subtracts the fit. The program can also provide wavelength calibration and extract a 1-D spectrum but we only used this package to produce reduced sky-subtracted 2-D frames.

Finally, individual frames for each object, output from NIRSPEC_REDUCE, were median combined with IRAF task IMCOMBINE. Nods along the slit were removed by providing integer pixel offsets in the spatial direction using the 'offsets' parameter in IMCOMBINE to bring all the frames to the position of the first frame. For LAE25972, ten 120-second frames were median combined. For LAE7745 and LAE6559, the seven 240-second frames were median combined.

Only one object, LAE7745, shows a detection in the reduced 2-D image. The detection corresponds to the expected spatial-direction location of the LAE based on its distance from the bright continuum object. The detection also corresponds to the approximate expected dispersion-direction location of an [O III] detection based on the Lyα redshift of z $\sim$ 3.1. Given that this detection appears at both the expected spatial *and* dispersion locations gives strong credibility to this being a real detection of [O III] and not an errant cosmic ray. In addition, while the detection can't be seen in a single exposure, it can be seen faintly when a single exposure is subtracted from a nodded subsequent exposure. This detection is shown in the top panel of Figure 3.2. The other two objects show no detections and are shown in the bottom panel of Figure 3.2. Possible reasons for non-detections are insufficient integration time for faint lines and emission lines located under OH skylines. We argue in Section that insufficient integration time is a likely culprit for these two nondetections.

3.3.7.2 1D Reduction of LUCIFER spectra

The 1D spectra were created following a similar reduction process to that outlined in Mc11. We utilized the DOSLIT routine in IRAF (Valdes, 1993). A bright (R $\sim$ 12–18) continuum source shared the slit with each LAE so we were able to create a trace for extraction from the bright object. The trace was then shifted along

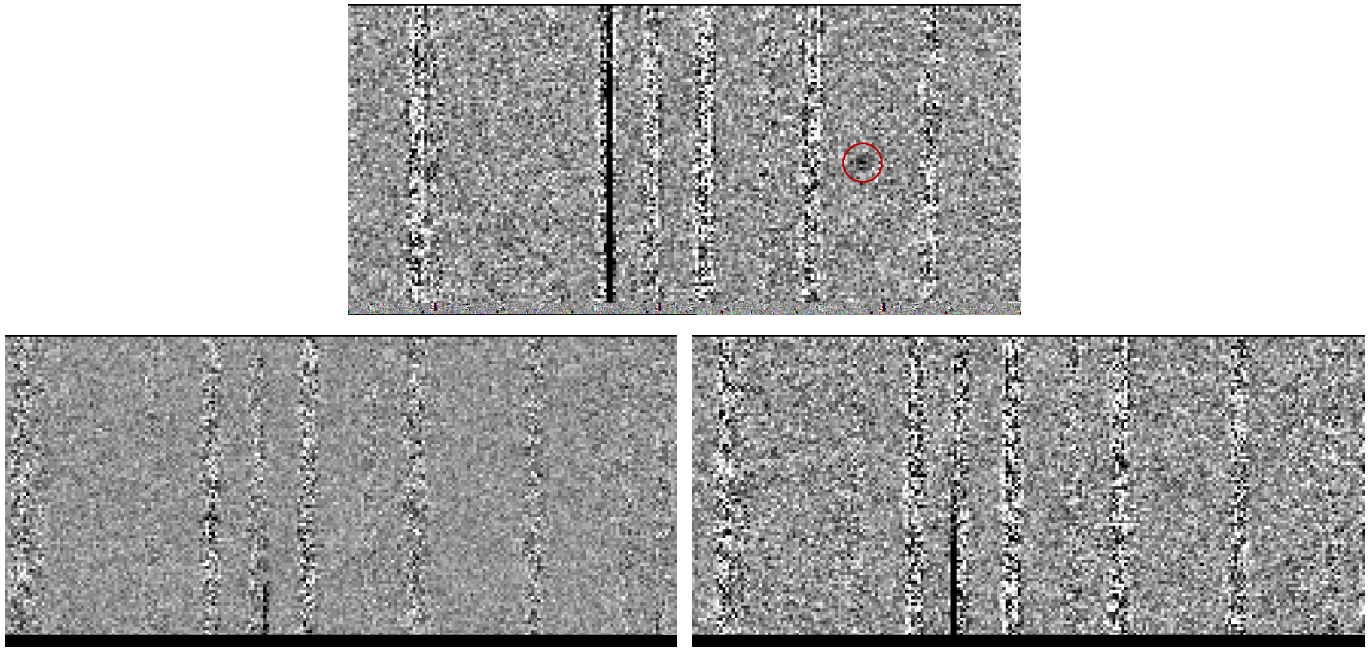

Figure 3.2 Top panel: 2D spectrum of LAE7745 with detection of the [O III] 5008.240 Å line shown in the red circle. Bottom panel: 2D spectra of LAE25972 (left) and LAE6559 (right). Wavelength increases from left to right from $\sim$ 19771 Å to $\sim$ 20728 Å, a bad column in the detector is seen just left of center in each frame.

the spatial axis to extract the LAE spectrum, whose continuum emission is undetectably faint in individual exposures and therefore cannot be traced. DOSLIT was performed on the median combined, sky subtracted 2D spectra from NIRSPEC_REDUCE. Wavelength calibration was done using night sky OH lines. The average RMS uncertainty from wavelength calibration for LAE7745 $\sim$ 0.66 Å. Residual bright night sky lines were interpolated over using the SKYINTERP task from the WMKONSPEC package originally designed for Keck NIRSPEC reduction[5].

Flux calibration proceeded, as in MC11, using the bright continuum sources that shared the slit with our LAEs. LAE7745 was calibrated using SDSS J095930.35+015646.6. We flux calibrated the spectrum of the bright continuum star spectrum using an appropriate Pickles model spectrum (Pickles, 1998), scaled in flux to match the apparent V magnitude of the object that shared the slit. We determined the appropriate Pickles model spectrum to use by determining the star's spectral type from SDSS u-g and g-r colors (Fukugita et al., 2003). The SDSS u, g and r magnitudes for this determination come from SDSS DR7. The V magnitude of the observed of the calibration star was determined from its SDSS colors and the Lupton 2005 color transformation from SDSS g-r color to V magnitude[6]. The sensitivity curve for calibration comes from dividing the scaled-down Pickles model by the bright continuum star's stellar spectrum in counts. The raw LAE spectrum was multiplied by the sensitivity curve to produce a final flux-calibrated NIR LAE spectrum. This method ought to account for slit losses automatically, provided that slit losses are the same for both the on-slit continuum source and the LAE.

[5]http://www2.keck.hawaii.edu/inst/nirspec/wmkonspec.html

[6]http://www.sdss.org/dr6/algorithms/sdssUBVRITransform.html

3.3.8 NIRSPEC data and reduction

Two of our five additional NIR observations were made at the Keck II telescope using NIRSPEC. Observations were made on January 30, 2010 and February 1, 2010. We used the 42x0.76 arcsecond slit and the low-resolution mode of NIRSPEC for these observations. For LAE42795 we obtained nine 360-second frames of K band spectroscopy, using the blocking filter NIRSPEC-7 and seven 600-second frames of H band spectroscopy, using the blocking filter NIRSPEC-5. The K band spectra show a very broad [O III] emission line. In Section 3.4.3 we discuss our interpretation of this broad line as evidence of AGN activity. For LAE27190 we obtained five 360-second frames of K band spectroscopy using the NIRSPEC-7 filter. We saw no evidence of [O III] or any other optical emission lines in LAE27910. In addition, LAE6559 was observed with NIRSPEC in addition to LUCIFER, but yielded no detections with either instrument. The Keck observations for LAE6559 consisted of five 360-second frames of K band spectroscopy using the NIRSPEC-7 filter.

We reduced the NIRSPEC data again using the NIRSPEC reduction package Becker et al. (2006). For this reduction, the spectra were first flat-fielded, and then corrected for dark current using a constant value. The sky was then subtracted again using the optimal sky-subtraction technique of Kelson (2003).

In order to correct for the distortion in both the x & y direction, we use the IRAF tasks XDISTCOR and YDISTCOR in the WMKONSPEC package specifically developed for the NIRSPEC data reduction. All pixels affected by cosmic rays are identified using the IRAF task CRMEDIAN, and these affected pixels are replaced by average counts calculated from neighboring pixels. We then average combine each individual spectra using IRAF task imcombine, for each of

the sources. We detected no optical emission lines in any object except the likely AGN (LAE42795).

3.4 Results from Optical and NIR Spectroscopy

3.4.1 Lyα line fluxes and asymmetries

We are able to measure Lyα line fluxes in our sample by fitting an asymmetric Gaussian to each line, as detected in our optical spectroscopy data. A more detailed description of this process is found in Mc11. To summarize, each Lyα line is fit with an asymmetric Gaussian using a modified version of the ARM_ASYMGAUSSFIT IDL routine developed by Andrew Marble[7]. The purpose of using a fitting routine that allows for, but does not require, an asymmetric solution is that it allows the red and blue sides of the Lyα line to be fit with different sigmas. In cases where the red-wing of the Lyα is elongated and/or the blue-side of the line is sharply truncated, this asymmetric fitting procedure will find a good fit that captures these characteristics. Asymmetric line profiles are predicted for high-z LAEs (Rhoads et al., 2003; Dawson et al., 2004; Kashikawa et al., 2006) because the blue side of the line will be preferentially absorbed by intervening neutral hydrogen. In addition, it has been shown that asymmetric Lyα lines can also be produced by Lyα radiative transfer through expanding shells, a model meant to represent outflows from star-bursting galaxies (e.g., Verhamme et al., 2006, 2008). The Lyα line flux is determined from the area under the asymmetric Gaussian. The average Lyα line flux of our entire confirmed sample is 17.4 ± 0.9 $\times 10^{-17}$ erg s^{-1} cm^{-2}. We quantify the asymmetry of the fitted Lyα lines as a_{rb}, which comes directly from our asymmetric fitting process; where a_{rb} is the ratio

[7] http://hubble.as.arizona.edu/idl/arm/

of the red-side best-fit sigma to the blue side best-fit sigma, or $a_{rb} = \sigma_{red}/\sigma_{blue}$. From this definition, when a_{rb} is > 1.0, the line is considered asymmetric in the expected direction for Lyα, i.e. with a larger red-side sigma. When a_{rb} is < 1.0 the line is also asymmetric but with a larger blue-side sigma, and when $a_{rb} = 0$ the line is symmetric. The average asymmetry, using this measure, of our entire confirmed sample of LAEs is 1.4 ± 0.1, indicating that, as a whole, our sample of LAEs does have asymmetric Lyα lines.

3.4.2 New [O III] detection

As mentioned above, this paper presents one new [O III] detection in a $z \sim 3.1$ LAE, excluding an [O III] detection in a likely AGN. Our new measurement was made in the same manner as the [O III] line flux measurements in Mc11. Namely, we fit the [O III] line with a symmetric Gaussian + constant, using the IDL routine MPFITEXPR. The area under the best-fit Gaussian determines the line flux of the [O III] line, the central wavelength of the fit determines the the systemic redshift of the galaxy, and the constant term is the continuum level. We report an error on these measured quantities determined from 1000 Monte-Carlo simulations. In these simulations, the actual 1D spectrum was modified at each point by a Gaussian random amount $\propto$ the error at that point, and then a Gaussian was fit to this modified data and this was repeated 1000 times. The standard deviation of the 1000 iterations for each quantity represents 1σ. The errors we report are three times this. Following this procedure, LAE7745 has an [O III] line flux of $13.7 \pm 1.8 \times 10^{-17}$ erg s^{-1} cm^{-2}. This is in addition to the our two previous detections reported in Mc11, where line fluxes of $7.0 \pm 0.3 \times 10^{-17}$ and $35.5 \pm 1.2 \times 10^{-17}$ erg s^{-1} cm^{-2} were reported for LAE27878 and LAE40844, respectively. The other characteristics of the best-fit Gaussian for LAE7745 are a

central wavelength of 20636.7 ± 1.3 Åand a constant term of $9.2 \pm 0.13 \times 10^{-19}$ erg s^{-1} cm^{-2} $Å^{-1}$, meaning the continuum, within the error bars, is essentially zero. We do not detect the second [O III] line at rest-frame 4960 Å in LAE7745.

3.4.3 AGN in the sample

LAE25972 was not well fit with any of our star-forming SED models (reduced $\chi^2 \sim 31$, see Section 3.5) , leading to consideration that this object may instead be a Lyα-selected AGN, especially since this object also had the largest Lyα line flux in our sample. This object does not have an X-ray counterpart in the Chandra COSMOS Survey Point Source Catalog (Elvis et al., 2009) but the catalog may be too shallow to rule out a faint X-ray counterpart (limiting depth $= 5.7 \times 10^{-16}$ erg s^{-1} cm^{-2}, corresponding to X-ray luminosity of 4.9×10^{43} ergs s^{-1} at $z = 3.1$, assuming a X-ray photon index $\Gamma = 2.0$). This object does, however, have a number of other AGN signatures based on the strength of its Lyα line. For example, the Lyα line flux of 7.8×10^{-16} erg s^{-1} cm^{-2} corresponds to a Lyα luminosity of 6.75×10^{43} erg s^{-1}. This Lyα luminosity is larger than five of the six Lyα-selected AGN at $z = 3.1 - 3.7$ discussed in Ouchi et al. (2008). A similar comparison to Zheng et al. (2010) yields a similar conclusion - namely Zheng et al. (2010) found that all Lyα detected objects with Lyα luminosity $\geq$ 1.8×10^{43} were AGN. They investigated seven Lyα-selected AGN from $z = 3.1 - 4.5$ to reach this conclusion. The Lyα luminosity of LAE25972 is well above this threshold. Finally, the velocity-width of the Lyα line for this object is very large at 1344 km s^{-1}. From the large velocity-width of the line combined with the diagnostics from Ouchi et al. (2008); Zheng et al. (2010) we conclude that this object is likely an AGN.

LAE42795 also does not have an X-ray counterpart in the Chandra COSMOS Survey Point Source Catalog, but it does have a strong [O III] detection. The [O III] line is, however, quite wide. We interpret this as strong evidence for AGN activity in this object. This interpretation is supported by a possible detection of the CIV 1549Å line in the MMT optical spectrum.

We exclude both of the likely AGN from our SED fitting results below, and they are excluded anywhere average characteristics of the LAEs are reported, so that these averages only reflect the characteristics of (33) typical star-forming LAEs in our sample.

3.4.4 Lyα -[O III] Velocity offsets

Using the new [O III] detection, we are also able to determine a velocity offset between the Lyα and [O III] lines as we did in Mc11. The [O III] line defines the systemic velocity of the galaxy, and the Lyα line, subject to deformation from neutral hydrogen both in the galaxy and in the IGM, is shifted redward. We find a velocity offset between [O III] and Lyα in LAE7745 of 52 ± 25.2 km s^{-1}, after correction for the earth's motion. We follow the same procedure we reported previously in Mc11 to make this new measurement; the velocity offset is determined based by comparing the central wavelength of each line - where the central wavelength is determined by the best-fit asymmetric (for Lyα) and symmetric (for [O III]) Gaussians. The offset between the [O III] and Lyα lines is illustrated in Figure 3.3 below, and the same plots are shown in Figure 2 in Mc11. The measurement reported here is in addition to the velocity offsets of 125 ± 17.3 and 342 ± 18.3 km s^{-1} we previously reported for LAE14310 and LAE40844, respectively, making the new measurement the smallest velocity offset we have seen. This result is suggestive of a wide distribution of velocity offsets in LAEs at z $\sim$

3.1 - suggesting there is not a single characteristic velocity offset but rather a distribution. This result is not surprising considering the generally diverse physical characteristics (age, mass, star formation history etc.) of the sample that we find from SED fitting in section 3.5. If these observed velocity offsets are due to star burst driven winds, one would expect galaxies with diverse characteristics to drive different winds. We also note that this result is still consistent with the various models (e.g. Verhamme et al., 2006, 2008; Steidel et al., 2010)discussed in Mc11 as possible matches to our observations. We encourage the reader to see Mc11 for more discussion of these models.

While detections of [O III] in the NIR for high-z LAEs are still novel, making this an exciting result and one that shed light on the kinematics of LAEs and Lyα escape, we would like to have a better ability to predict which LAEs will yield [O III] detections, since only three of our six observations have yielded [O III] detections so far (excluding the two AGN). A new approach that may help tackle this challenge is discussed in Section 3.5 below. In addition, more detections are needed to really understand the full distribution of these velocity offsets and how they correlate with other characteristics of LAEs. This distribution is something we can not characterize yet with only three measurements but should be approachable as more NIR instruments come on-line, particularly those with multi-object capabilities.

3.5 Constraining physical parameters with SED fitting

To constrain the physical properties of our 33 (non-AGN) LAEs we produced stellar population model spectra produced using the latest Charlot & Bruzual (2011) code (henceforth CB11). This is the latest update to the Bruzual & Charlot (2003) code. This latest version includes contributions from TP-AGB stars and al-

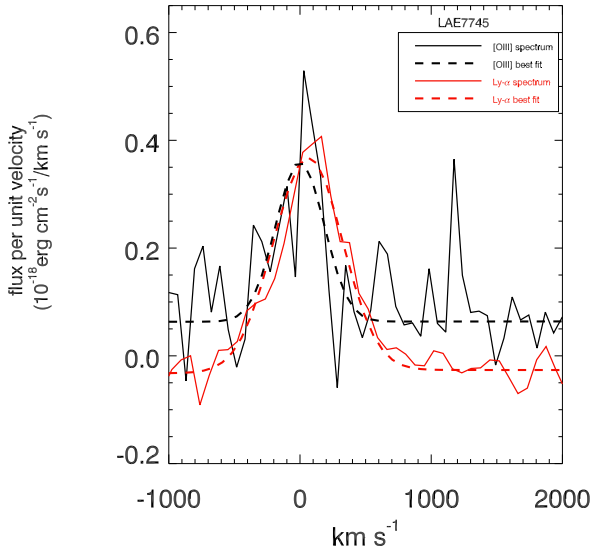

Figure 3.3 Velocity offset between [O III] and Lyα as detected in one new LAE observed in 2011 with Hectospec and LUCIFER. [O III] spectrum is in black, Lyα spectrum is in red, where Lyα line is offset from [O III] by 52 km s^{-1}. See Mc11, Figure 2, for two previously observed LAEs with velocity offsets of 342 and 125 km s^{-1}.

lows for exponentially increasing star formation histories. We use a Salpeter IMF. We created model spectra with an extensive grid of ages, metallicities, star formation histories, and dust extinction values. We also present an additional, new fitted parameter, a line flux contribution to the K_s band, which is discussed in more detail below. For $z \sim 3.1$ LAEs, the 5008.240 Å [O III] line is redshifted into the K_s filter. We report a single line flux for the [O III] line, but one can consider that this emission is really split between the two lines in the 4960.295/5008.240 Å [O III] doublet (with a ratio of $\sim$ 1 to 3 in the 4960.295 and 5008.240 lines, respectively). Technically, the 4862.683 Å Hβ line also falls in the K_s filter for a $z \sim 3.1$ galaxy, and the 3727.092/3729.875 Å [O II] lines could fall in the H filter. However, our LUCIFER observations have covered the full H and K_s wavelength range and we have only detected [O III]. Hence, we attribute all the additional line flux in the K_s band to [O III]. We note, however, that our method does not rule out that this emission comes from multiple lines and it could be divided amongst [O III] and Hβ a posteriori. Because we have not yet detected [O II] we do not alter the H band flux for this line, but this could easily be added to future analyses if future observations indicate that it is warranted. It is also worth noting that most SED results to date have indicated LAEs are relatively metal poor (e.g. Finkelstein et al., 2011a) and hence we can expect the [O III] line to be much brighter and contribute much more to the broadband flux than the [O II] lines.

Ages for our models vary on an irregular grid of 48 values, from 1.78×10^6 years to 2.099 Gyrs (approximately the age of the universe at $z = 3.1$). Dust extinction, E(B-V), is allowed to assume 31 regular values to produce 0-6.6 magnitudes of dust extinction (A_{1200}) Dust attenuation is applied to our models using the Calzetti formulation (2000). Metallicity is allowed to assume 5 values from 0.005 - 1.0 $Z_\odot$. We chose only exponential star formation rates, investigating both ex-

ponentially increasing and exponentially decreasing rates. Star formation history e-folding time, τ, can assume 6 positive values from $\tau = 0.0001$ - 4.0 Gyr. This essentially creates one template of instantaneous star formation (when $\tau = 0.0001$ Gyr which is much younger than the age of the O/B star) and one template with continuous star formation (when $\tau = 4$ Gyr which is longer than the age of the universe at z=3.1) with four templates of exponentially decaying star in between ($\tau = 0.001, 0.01, 0.1, 1$ Gyr). We add to this two negative e-folding times ($\tau =$ -0.1, -1 Gyr) to explore exponentially increasing models, bringing our total number of possible tau values to eight. Redshifts were fixed for each object, depending on the redshift of the Lyα line, as this should be close to the correct redshift depending on the possible velocity offset of Lyα from systemic (even with our largest detected offset of 342 km s^{-1}in MC11, δz between Lyα and [O III] is < 0.005). Our full grid contains 1.116×10^6 models, probing a very large parameter space.

3.5.0.1 Photometry for χ^2 minimization

For our SED fits we used model and observed photometry in the B, V, g′, r′, i′ z′, J, H and Ks bands and IRAC 3.6 μm bands. We don't use the u* filter because this is the dropout band for z $\sim$ 3.1 LAEs. We use photometry from the COSMOS Intermediate and Broad Band Photometry Catalog catalog (Capak et al., 2007) for the B, V, g′, r′, i′ z′ bands (3″aperture photometry). The IRAC 3.6 μm data comes from the S-COSMOS IRAC 4-channel Photometry Catalog[8] available on the NASA/IPAC archive. We use the 2.9″aperture fluxes from this catalog (Sanders et al., 2007). Six LAEs have IRAC 3.6 μm detections in this catalog. For uncrowded objects with no IRAC 3.6 μm detection, we use the 3σ depth (5.4 $\times 10^{-30}$ erg/s/cm^2/Hz) of the IRAC 3.6 μm image as an upper limit. This is the

[8]http://irsa.ipac.caltech.edu/data/COSMOS/tables/scosmos/

case for 15 LAEs. In the 12 cases where neither a detection nor an upper limit could be used, the χ^2 minimization process does not use IRAC 3.6 μm. 29 of the LAEs in our sample are covered by the deep UltraVISTA Survey in the COSMOS field (McCracken et al., 2012) and we used these new J, H, and K_s images for our NIR photometry. The photometry for each object was measured using SExtractor. SExtractor detections were forced at the desired coordinates (coordinates taken from the COSMOS catalog) by creating images with bright, fake sources at the correct coordinates and running SExtractor in dual-image mode with these fake images as the detection images and the J/H/K_s images as the detection images, thereby recovering photometry (in a 2″) aperture of each object at the correct location in the correct filter. For the four LAEs not covered by UltraVISTA, we extracted J, H and K_s photometry from earlier publicly available COSMOS images. We used the CFHT H and K_s band images (McCracken et al. , 2010) and for J we used the UKIRT J images (Capak et al., 2007). Again, SExtractor detections were forced at the desired coordinates as described above, in 3″ apertures.

3.5.0.2 Accounting for Lyα line

The Lyα line for a z $\sim$ 3.1 galaxy lies within both the g′ and V filters. Since we have optical spectra and hence we have spectroscopic Lyα line fluxes for each object we can remove this line from the g′ and V bands before fitting (since the CB11 models to which the observed g′ and V photometry will be compared don't include Lyα). We remove Lyα by converting Lyα line flux to its appropriate flux density in the g′ and V bands. The transmission in the g′ band at the location of Lyα is $\sim$ 100% so we subtract this entire Lyα flux density from the observed flux density in the g band. The transmission in the V band at the location of Lyα is

only $\sim$ 63% so the Lyα flux density in the v band is multiplied by a factor of 0.63 before it is subtracted from the observed V band flux density. The Lyα line flux is determined as described in Section 3.4.1.

3.5.1 SED models

The CB11 code creates model spectra in units $L_{\odot}\, A^{-1}$ for 91 - 3.6$\times$ 10^8 Å. This output was converted to flux density (F_ν) using the following two conversions (Papovich et al., 2001; Kaleida & Scowen, 2010):

$$L_\nu = \frac{10^8 \lambda_0^2 l_\lambda L_\odot}{c M_{gal}} 10^{-0.4[E(B-V)k'(\lambda)]} \tag{3.9}$$

$$F_\nu = \frac{(1+z)L_\nu}{4\pi d_L^2} e^{-\tau_{IGM}} \tag{3.10}$$

l_λ is the CB11 output in units $L_\odot A^{-1}$, 10^8 converts from Å to μm, [E(B-V)$k'(\lambda)$] is wavelength dependent and calculated from Calzetti (2000), λ_0^2 is wavelength in the galaxies rest-frame, M_{gal} is the total mass in the stellar population at a given age, z is the redshift of the model, fixed to z = 3.1, τ_{IGM} is wavelength-dependent IGM absorption from Madau (1995) and d_L is the luminosity distance for z = 3.1. After application of Equation3.10 and convolution of the flux through each filter, we have an individual flux density value for each filter (b, v, g, r, i, z, g, h, k, IRAC 3.6 μm). These flux densities are all normalized to 1 $M_\odot$ until one solves for mass.

It is at this point that we add our new parameter, [O III] line flux. We modify (amplify) the flux in the K_s band to mimic how [O III] can contribute flux in this filter. The modification looks like:

$$f_{total} = f_k + f_{[O\,iii]} \tag{3.11}$$

where f_k is the unmodified model flux density in the K_s band. $f_{[O\,iii]}$ is the [O III] line flux in the band, and f_{tot} is the total flux density in the K_s band after those of two fluxes are combined. $f_{[O\,iii]}$ is defined as

$$f_{[O\,iii]} = x f_k \tag{3.12}$$

where x takes on 15 uniform values from 0 - 1.5, meaning there are 15 possible possible [O III] fluxes that could be fit. When x=0 this means there is no additional line flux from [O III] added to K_s band, and this result is chosen as the best fit for some of our LAES (see 3.2). This method essentially allows for additional line flux in the K_s band, but allows the underlying spectrum to still be a younger/less massive galaxy, which would not necessarily be the case if an artificially large K_s band flux forced an older and more massive solution to be fit. Schaerer & de Barros (2009) pointed out the importance of including some treatment of nebular emission lines when fitting starbursting galaxies, when they found that ages in a sample of $z \sim 6$ galaxies could be overestimated by as much as four times and mass by as much 1.5 times when nebular emission lines were not accounted for. Some treatment of nebular emission lines is certainly warranted, but we advocate a simpler methodology (Equation 3.11) for accounting for nebular emission. This methodology only requires that a single additional parameter be added to our fitting process, avoiding a complex recipe of adding a large number of lines to our spectra - and this single parameter can be accounted for across all possible star formation histories and metallicities. As Nilsson et al. (2011) and Nakajima et al. (2012) have noted, accounting for such detailed nebular emission line recipes across multiple star formation histories and metallicities can be too complex, limiting the parameter space that can be probed. We avoid this by dealing with only a single parameter that is matched to what we have actually observed - i.e. we have

observed some of these LAEs in the NIR and only detected [O III], so this is the only line/parameter we are adding. We can directly compare our NIR observations to the predictions from our model fitting process (3.7.1).

Finally, mass is a fitted parameter, calculated from minimizing the χ^2 in Equation3.13 for each model. This means that for each model there is a single best-fit mass solution found by minimizing χ^2 with respect to mass:

$$\chi^2 = \sum_i [\frac{f_{\nu,i}^{obs} - M f_{\nu,i}}{\sigma_i}]^2 \tag{3.13}$$

Here the subscript 'i' represents each filter where the model and observed photometry are compared.

3.5.2 Allowed fits

Some of our LAEs are best fit, strictly via χ^2 minimization, with old stellar populations. These fits require careful consideration because older stellar populations may not be able to produce enough ionizing photons to produce the Lyα lines we have measured (with optical spectroscopy) in these objects. We therefore consider some additional constraints on these objects to see if these old best-fit solutions are, in fact, realistic, physically-motivated solutions or if they ought to be ruled out in favor of younger, dustier solutions.

The CB11 code produces a parameter, NLyα, that is the log rate of ionizing photons (s^{-1}) produced at each age of the model for a given metallicity. Assuming case B recombination, where two of every three of these photons produces a Lyα photon, we can turn this production rate into a Lyα line strength at each model age. This allows us to test if the best fit age for a given object is able to produce, at a minimum, the Lyα line we have measured for that object with spectroscopy. We do not subject this Lyα line to attenuation by dust and/or

the IGM, as we are simply testing if, at a minimum, the model stellar population could intrinsically produce enough ionizing photons to begin with, before any attenuation.

The actual mechanism for this calculation is as follows:

$$\text{Ly}\alpha \text{ line flux} = \frac{2}{3}\frac{10^{\text{NLy}\alpha}[h\nu_{Ly\alpha}]}{4\pi d_L^2}\frac{\text{M}_m}{M_{gal}} \tag{3.14}$$

where $\frac{2}{3}$ is the coefficient for Lyα for case B recombination, NLyα is the log production rate of ionizing photons, h$\nu_{\text{Ly}\alpha}$ is the energy of a Lyα photon, and d_L is the luminosity distance at z = 3.1 (Wright, 2006). M_{gal} is the total mass in the stellar population at a given age and M_m is the best fit mass (in $\text{M}_\odot$) for the model under consideration, so that the final term $\frac{\text{M}_m}{M_{gal}}$ scales the model stellar population from its normalized, $< 1\text{M}_\odot$mass, to the appropriate galactic size stellar mass.

Only models (i.e combinations of metallicity, age, star formation history, dust, and mass) that can produce, at a minimum, enough ionizing photons to power the Lyα line we observe are considered 'allowed' fits. With this information, we find the model with the smallest χ^2 from amongst only these 'allowed' possibilities. Henceforth, we'll refer to this as the best allowed-fit for each object.

An example of this calculation, for LAE40844, is shown in Figure 3.4. Figure 3.4 shows the strength of the Lyα line (solid curve) as function of stellar populations of increasing age for constant mass, metallicity, and τ. This particular figure is constructed using the best allowed-fit model for LAE40844, where metallicity is 0.2 $\text{Z}_\odot$, τ is 0.001 Gyrs, and mass is 2.9×10^9 $\text{M}_\odot$. The maximum age this combination of mass, metallicity, and τ can have and still produce the amount of Lyα flux we have observed is shown as a black vertical line. The best allowed-fit age is shown as a red vertical line. This diagnostic shows why this combination of mass, tau, metallicity, and age is an allowed solution for LAE40844 - namely

that that the model age is to the left (younger) than the maximum age allowed that could still produce the number of Lyα photons we have observed from this object. The observed Lyα line strength is shown as a dashed line.

Finkelstein et al. (2007, 2009) directly added the Lyα line to their BC03 models, using a similar calculation and the appropriate information from the *.3color and *.4color files. The Lyα line flux then becomes an additional fitted and minimized parameter in their work. Our related approach is to rule out models after the fact instead of adding an additional fitted parameter - but both methods should produce similar results and are meant to help break the degeneracy between old, dust-free and young, dusty solutions, and make sure that the solution chosen as the best-fit makes physical sense and can actually produce sufficient Lyα flux.

3.6 Results from SED Fitting

Model spectra are shown below in Figure 3.8 – Figure 3.14 for all 33 LAEs. Observed magnitudes are shown as red diamonds and error bars on observed photometry are also shown. Red diamonds with a downward arrow instead of error bars indicates that an observed point was fainter than the 3σ depth of the image. Magnitudes from the model spectra are shown as blue diamonds. For objects where the model included [O III] line flux in the Ks band, you will note that both the red and blue diamonds lie above the black model spectrum. This is expected as it means that an artificially large Ks band flux from [O III] line flux pollution in this band is not dominating/skewing the best fit results. Results for fitted parameters for each object are shown in Table 3.2.

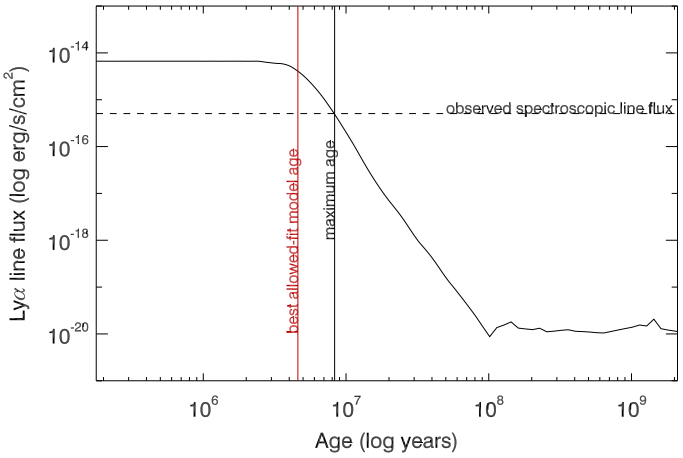

Figure 3.4 Model Lyα line flux (solid curve - from Equation 3.14) that can be produced by stellar populations of increasing age, for a fixed mass, metallicity and star formation history. This is the best allowed-fit model for LAE40844, where metallicity is $1Z_{\odot}$, tau is 0.01 Gyrs, and mass is 2.17×10^{9} $M_{\odot}$. The horizontal dashed line shows the observed spectroscopic Lyα line flux for LAE40844, the age of the best allowed-fit model is the red vertical line, and only models younger than the black vertical line can produce the observed Lyα line flux.

3.6.1 Goodness of fits

Our average reduced χ^2 is 7.9. The best fit object has a reduced χ^2 of 1.3 and the worst fit object has a reduced χ^2 of 22.9. We remind the reader that the model chosen as the best fit is not always the smallest χ^2 solution for each LAE, but rather, the model with smallest χ^2 from amongst those models that can produce enough ionizing photons (best allowed-fit). For objects with IRAC 3.6 μm photometry (meaning either a detection or the limit was used) there are four degrees of freedom. For objects with no IRAC 3.6 μm data, there are three degrees of freedom. These values comes from leveraging 10 bands (B, V, g, r, i, z, J, H, Ks, IRAC 3.6 μm) or nine bands when no data is available for the IRAC 3.6 μm band, against six fitted parameters (age, mass, metallicity, dust, tau, and [O III] line flux).

We demonstrated how well constrained the fits are for each LAE with Monte Carlo (MC) simulations of each individual object. We ran 1000 MC simulations for each object. In each of the 1000 iterations, we modified the observed fluxes in each band by a Gaussian random amount $\propto$ the error bar in that band and then we determined the best allowed-fit model for the altered photometry in the same manner as described above. Density plots showing the distribution of MC solutions around the best fit are shown in Figure 3.8 – Figure 3.14 for age, predicted [O III] line flux, and dust. Additional plots for other parameters are included in Appendix B. Contours encompassing approximately 68% and 95% lie of the MC results are also shown on each plot. In addition, Table 3.2 includes a 68% confidence range for each fitted parameter. This range was calculated by sorting (from smallest to largest) the 1000 MC solutions for a given parameter, and finding the spread given by the central 680 solutions in the sorted array.

3.6.2 Star formation history results

While some recent literature (Maraston et al., 2010; Finlator et al., 2011; Papovich et al., 2011) has suggested that high-z star-forming galaxies may be better fit with exponentially increasing star formation rates, in fitting 33 individual LAEs we find that only seven galaxies in our sample (21%) are best fit with an exponentially increasing star formation rate. Instead, we find that the majority of the sample is best fit with a single instantaneous burst (36%, $\tau = 0.0001$ Gyr) or exponentially decreasing star formation rates (33%, $\tau = 0.001$ – 1.0 Gyr). In addition, three LAEs are best fit with constant star formation rates ($\tau = 4$ Gyr).

3.6.3 Age results

We report star formation weighted ages, age_{SFR}, for each galaxy both here and in Table 3.2 (Raichoor et al., 2012). Star formation weighted ages better represent the age of the bulk of the stars and are therefore more informative than directly quoting the ages of the models. Equation 3.15 shows the derivation of this weighted age for exponentially decreasing star formation rates (Raichoor et al., 2012).

$$\langle age \rangle_{\mathrm{SFR}} = \frac{\int_0^t (t-t')e^{-t'/\tau}\mathrm{d}t'}{\int_0^t e^{-t'/\tau}\mathrm{d}t'} = \frac{\tau e^{-\frac{t}{\tau}} - \tau + t}{1 - e^{-\frac{t}{\tau}}} \tag{3.15}$$

where t is the age output from the model (i.e. time since star formation began) and tau is the e-folding time of the star formation rate as output from the model. We also derived the same type of star formation weighted age for the case of exponentially increasing star formation, with the expression shown in Equation 3.16:

$$\langle age \rangle_{\mathrm{SFR}} = \frac{\int_0^t (t-t')e^{t'/\tau}\mathrm{d}t'}{\int_0^t e^{t'/\tau}\mathrm{d}t'} = \frac{\tau - \tau e^{\frac{-t}{\tau}} - t e^{\frac{-t}{\tau}}}{1 - e^{\frac{-t}{\tau}}} \tag{3.16}$$

Our median age$_{SFR}$ is 4.5 $\times$ 10^8 years, with age$_{SFR}$ spanning 1.6 $\times$ 10^6 – 6 $\times$ 10^8 year. The median size of the 68% confidence ranges calculated for each object is 3.3 $\times$ 10^6 years, making age one of the best constrained parameters. A majority of our sample, (76%) have age$_{SFR}$ $<$ 100 Myrs. Hence our sample of 33 galaxies fits with previously reported results (e.g. Gawiser et al. 2007, Pirzkal et al. 2007, Finkelstein 2009, Finkelstein 2011, Cowie et al. 2011) that LAEs have largely young to intermediate ages.

3.6.4 Mass results

The median stellar mass in our sample is 1.5 $\times$ 10^9 M$_\odot$. The most massive solution in our sample is 6 $\times$ 10^{10} M$_\odot$ and the smallest solution is 8.7 $\times$ 10^7 M$_\odot$. The median mass we report here is significantly larger than the characteristic masses derived from stacked z $\sim$ 3.1 LAEs (Acquaviva et al., 2012; Gawiser et al., 2006, 2007; Nilsson et al., 2007; Ono et al., 2010). significantly larger than the characteristic masses derived from stacked z $\sim$ 3.1 LAEs (Acquaviva et al., 2012; Gawiser et al., 2006, 2007; Nilsson et al., 2007; Ono et al., 2010). This difference is a result of the wide-field and therefore shallower nature of our survey, meaning we have selected LAEs from the brighter and more massive end of z $\sim$ 3.1 LAE population compared to the samples mentioned above. We discuss this further in Section 3.7.3.

3.6.5 Dust results

The average E(B-V) value in our sample is 0.14, with a median value of 0.1, both corresponding to less than a magnitude of extinction. The largest E(B-V) value in the sample is 0.8. Only two objects are fit with absolutely no dust extinction, but an additional six objects have 68% confidence ranges that include

E(B-V) = 0. We also note that a total of 27% of the sample has the smallest non-zero E(B-V) solution, where E(B-V) = 0.05. These trends seem to indicate that overall, we are looking at a sample of galaxies that do not contain much dust.

3.6.6 [O III] line fluxes results

The main feature that distinguishes this work from previous SED fitting work with LAEs is the inclusion of an additional fitted parameter to account for [O III] line flux in the Ks band (where the [O III] 5008.240 Å line is redshifted for z ∼ 3.1 galaxies). We chose to add this single line as this is the only rest-frame optical emission line we have detected in z ∼ 3.1 LAEs via NIR spectroscopy. This puts us in a unique position to compare [O III] predictions from our models for these three objects with actual measurements in the same objects. We also have three LAEs in which we did not detect [O III] for comparison. As for overall results of our [O III] fitting approach, we find that 70% of our sample is best fit with an [O III] line flux > 0. This means that 10 LAEs are best fit with no additional flux from the [O III] line contributing to the K_s band. The average best-fit [O III] line flux in our sample is 2.8×10^{-17} erg s^{-1} cm^{-2}.

3.7 Discussion

3.7.1 Comparison of predicted to observed [O III] line flux

We have observed six non-AGN objects with NIR spectroscopy to look for [O III] and other rest-frame optical nebular emission lines. As discussed previously, we have [O III] detections for three of these objects. Comparing [O III] line flux from our model predictions for these galaxies to the the actually observed line flux we find that all three of the galaxies with observed [O III] lines

Object	Mass (log)	68% CR	Tau	68% CR	Age_{SFR} (log)	68% CR	Metal	68% CR	E(B-V)	68% CR	[O III][c]	68% CR	χ_r^2
LAE_J100049.56+021647.1[b]	9.89	9.88-9.96	1.0e-01	1.0e-01-1.0e+00	8.12	8.12-8.13	0.020	0.020-0.020	0.00	0.00-0.05	0.00	0.00-0.00	12.1
LAE_J095859.33+014522.0	9.55	9.52-9.77	1.0e-02	1.0e-04-1.0e-02	6.33	6.09-6.47	1.000	1.000-1.000	0.30	0.30-0.35	0.94	0.51-1.10	21.6
LAE_J100212.99+020137.7[a]	9.24	9.18-9.27	1.0e-04	1.0e-04-1.0e-04	6.21	6.09-6.40	1.000	1.000-1.000	0.25	0.25-0.25	0.00	0.00-0.00	14.7
LAE_J095929.41+020323.5 (LAE6559)	8.53	8.52-8.88	1.0e-04	1.0e-04-1.0e-03	6.21	6.09-6.77	1.000	0.005-1.000	0.15	0.15-0.20	0.18	0.00-0.26	11.3
LAE_J095944.02+015618.8	9.66	9.38-9.75	4.0e+00	1.0e-04-4.0e+00	8.47	7.95-8.66	0.005	0.005-0.200	0.05	0.00-0.10	0.00	0.00-0.07	2.6
LAE_J095930.52+015611.0 (LAE7745)	9.41	9.40-9.86	-1.0e+00	-1.0e+00-1.0e-01	7.85	7.85-8.78	0.200	0.005-0.400	0.05	0.00-0.05	1.55	1.37-1.59	7.0
LAE_J100217.05+015531.7[b]	10.12	8.97-10.17	-1.0e+00	1.0e-04-1.0e+00	8.41	6.59-8.49	1.000	0.200-1.000	0.05	0.05-0.15	0.00	0.00-0.44	22.9
LAE_J100157.87+021450.0[a]	8.74	8.60-9.02	1.0e-04	1.0e-04-1.0e-03	6.96	6.40-7.02	1.000	0.200-1.000	0.05	0.05-0.15	0.28	0.11-0.49	3.4
LAE_J100124.36+021920.8 (LAE40844)	9.29	9.27-9.32	1.0e-03	1.0e-04-1.0e-03	6.56	6.56-6.70	0.200	0.200-0.200	0.15	0.10-0.15	3.70	3.57-4.09	10.5
LAE_J095847.81+021218.2	8.65	8.46-8.86	-1.0e-01	-1.0e-01-1.0e-02	6.30	6.28-6.60	1.000	1.000-1.000	0.10	0.05-0.10	0.81	0.53-0.87	5.9
LAE_J095904.93+015355.4	8.39	8.18-8.76	1.0e-03	1.0e-04-1.0e-03	6.70	6.40-6.83	0.005	0.005-0.020	0.15	0.10-0.20	0.00	0.00-0.00	4.6
LAE_J095910.90+020631.6[b] (LAE14310)	9.17	8.31-9.49	-1.0e-01	-1.0e-01-1.0e-01	8.00	6.49-8.02	1.000	0.005-1.000	0.05	0.05-0.15	0.06	0.00-0.28	5.7

Table 3.2 Best allowed-fit parameters from SED fitting for each object in our sample, excluding AGN. Mass is in $M_\odot$, Tau is e-folding time for star formation, in Gyr, Age_{SFR} is the star formation weighted age, in years, Metal is metallicity in $Z_\odot$, E(B-V) is standard color excess from dust attenuation, [O III] is predicted [O III] line flux in erg s^{-1} cm^{-2}, χ_r is reduced chi square of the best allowed-fit model. 68% confidence ranges (CR) are also given for each parameter.

[a] Poor agreement between spectroscopic and photometric Lyα line flux measurements

[b] Possible multiple components in HST ACS image

[c] Predicted [O III] line flux, Units are 10^{-16} erg s^{-1} cm^{-2}

Object	Mass (log)	68% CR	Tau	68% CR	Age$_{SFR}$ (log)	68% CR	Metal	68% CR	E(B-V)	68% CR	[O III][c]	68% CR	χ^2_r
LAE_J095921.06+022143.4	9.90	8.94-9.93	1.0e-02	1.0e-04-1.0e-02	7.58	6.65-7.58	0.005	0.005-0.400	0.20	0.20-0.25	0.27	0.00-0.51	1.7
LAE_J095948.47+022420.8	8.31	8.06-8.44	1.0e-04	1.0e-04-1.0e-03	6.65	6.59-6.65	0.005	0.005-0.005	0.15	0.10-0.20	0.61	0.44-0.69	6.5
LAE_J100019.07+022523.9 (LAE27878)	9.44	8.60-9.50	-1.0e+00	-1.0e-01-1.0e+00	7.99	6.46-8.01	0.020	0.005-0.020	0.10	0.10-0.20	0.07	0.00-0.28	4.7
LAE_J100100.35+022834.7	8.83	8.62-8.86	-1.0e+00	-1.0e-01-4.0e+00	6.42	6.42-6.65	0.005	0.005-0.005	0.15	0.10-0.15	1.10	0.94-1.15	4.4
LAE_J100146.04+022949.0	10.78	10.70-10.78	1.0e-01	1.0e-01-1.0e-01	8.49	8.49-8.49	1.000	0.400-1.000	0.10	0.10-0.10	0.52	0.51-1.01	3.5
LAE_J095843.11+020312.3[b]	8.30	8.29-8.55	1.0e-04	1.0e-04-1.0e-03	6.59	6.56-6.65	0.200	0.200-0.200	0.05	0.05-0.10	0.00	0.00-0.00	11.2
LAE_J100128.11+015804.7	8.98	8.86-9.10	1.0e-01	-1.0e-01-1.0e-02	6.60	6.42-6.77	0.400	0.005-1.000	0.20	0.15-0.25	1.27	1.16-1.38	14.8
LAE_J100017.84+022506.1 (LAE27910)	8.44	8.25-8.65	1.0e-03	1.0e-04-1.0e-02	6.63	6.46-6.65	0.005	0.005-0.005	0.10	0.05-0.15	0.53	0.31-0.71	2.3
LAE_J095839.92+023531.3	9.05	8.82-9.13	1.0e-04	1.0e-04-1.0e-04	6.21	5.42-6.40	0.005	0.005-1.000	0.20	0.15-0.20	0.00	0.00-0.14	13.2
LAE_J095838.90+015858.2	7.94	7.88-8.27	1.0e-04	1.0e-04-1.0e-04	6.59	6.59-6.59	0.005	0.005-0.005	0.15	0.15-0.25	0.29	0.09-0.39	5.7
LAE_J100020.70+022927.0[b]	8.06	8.03-8.27	1.0e-04	1.0e-04-1.0e-03	6.59	6.53-6.59	0.005	0.005-0.005	0.05	0.05-0.10	0.23	0.05-0.43	8.3

Table 3.3 Continuation of Table 3.2.

Object	Mass (log)	68% CR	Tau	68% CR	Age_{SFR} (log)	68% CR	Metal	68% CR	E(B-V)	68% CR	[O III][c]	68% CR	χ^2_r
LAE_J095812.33+014737.6[a]	9.41	9.40-10.02	1.0e-04	1.0e-04-1.0e-02	6.65	6.65-7.58	0.200	0.200-0.200	0.20	0.15-0.20	0.84	0.84-1.47	3.9
LAE_J095920.42+013917.1	8.95	8.88-9.13	1.0e-03	1.0e-04-1.0e-03	6.63	6.63-6.83	1.000	0.200-1.000	0.10	0.10-0.10	1.23	0.74-1.39	4.5
LAE_J095846.72+013706.1	8.67	8.61-9.05	1.0e-04	1.0e-04-1.0e-04	6.40	6.09-6.53	1.000	0.005-1.000	0.15	0.10-0.20	0.25	0.00-0.53	4.5
LAE_J095923.79+013045.6	10.58	10.93-11.28	1.0e-01	1.0e-04-1.0e+00	6.73	6.24-9.21	1.000	0.020-1.000	0.70	0.00-0.90	0.00	2.32-4.13	2.2
LAE_J100213.17+013226.8	10.06	8.08-9.78	4.0e+00	1.0e-04-1.0e+00	8.78	6.59-8.66	1.000	0.020-1.000	0.05	0.00-0.10	0.00	0.00-0.26	3.3
LAE_J095838.94+014107.9	8.15	8.13-9.73	1.0e-04	1.0e-04-4.0e+00	6.59	6.59-8.78	0.005	0.005-0.005	0.05	0.00-0.05	0.95	0.70-0.99	1.3
LAE_J095834.43+013845.6	9.71	8.45-9.82	4.0e+00	-1.0e+00-1.0e-01	8.16	6.53-8.28	0.005	0.005-0.200	0.15	0.15-0.20	1.10	0.86-1.24	9.6
LAE_J100302.10+022406.7	9.79	9.48-9.79	1.0e-04	1.0e-04-1.0e-04	6.28	6.21-6.47	1.000	1.000-1.000	0.30	0.25-0.30	0.00	0.00-0.27	15.1
LAE_J100157.45+013556.2	8.72	8.76-9.98	1.0e-02	1.0e-04-4.0e+00	6.65	6.48-8.31	1.000	0.005-1.000	0.10	0.00-0.15	1.01	0.31-1.32	4.6
LAE_J100152.14+013533.2	9.98	9.65-9.86	-1.0e+00	1.0e-04-4.0e+00	8.78	7.68-8.47	0.400	0.005-0.400	0.00	0.00-0.10	2.18	1.76-1.92	13.0

Table 3.4 Continuation of Table 3.2.

select models with [O III] lines. Our best prediction is for LAE40844, in which we observed a line flux of 3.6×10^{-16} erg s^{-1} cm^{-2} and our model predicted 3.7 $\times 10^{-16}$ erg s^{-1} cm^{-2}; a percent error between the model and prediction of less than 3%. This prediction also lies within the 1σ error bar on the observed [O III] line. In LAE7745, the perecent difference between the observed line flux (2.1×10^{-16} erg s^{-1} cm^{-2}) and the predicted [O III] line flux (1.5×10^{-16} erg s^{-1} cm^{-2}) is $\sim$ 29%. The model prediction for LAE27878 provides the worst agreement. The model prediction is only 6.7×10^{-18}, while the observed line flux in this object is 7×10^{-17}. The agreement is not good, but it is worth noting that LAE27878 has the smallest [O III] line flux of the three line fluxes we have measured to date, and the model correspondingly assigns the smallest predicted line flux of the three to this object as well.

As for the three LAEs in which we detected no [O III] line flux (LAE14310, LAE6559, and LAE27910), our models predict very little [O III] emission (5.6×10^{-18}, 1.8×10^{-17}, 5.3×10^{-17}erg s^{-1} cm^{-2}, respectively). While these objects did not have [O III] detections in our LUCIFER or NIRSPEC data, we note that the predicted line fluxes are extremely modest. In addition, the predicted fluxes for LAE14310 and LAE6559 are the faintest and third faintest predicted line fluxes among the 23 models with predicted line flux $\neq 0$. We derive a 3σ line flux limit from the 28 minute LUCIFER spectrum of LAE6559 of $\sim 1.4 \times 10^{-16}$ erg s^{-1} cm^{-2}. So the predicted model line flux of 1.8×10^{-17} erg s^{-1} cm^{-2}is well below what we would have been able to observe in this object. Given that this same object was also observed with NIRSPEC using a similar 30 minute integration which also yielded no detection, we argue that this upper limit should also approximate the upper limit for LAE27910, which was also observed for 30 minutes with NIRSPEC and which also yielded no detection. Comparison of the model

prediction for LAE27910 (5.3×10^{-17} erg s^{-1} cm^{-2}) and this approximate upper limit (1.4×10^{-16} erg s^{-1} cm^{-2}) once again shows that even if the galaxy produced that [O III] flux we would see it as a nondetection given our modest integration time. For LAE14310, which had a noisier NIR spectrum, we derive a 3σ upper limit of $\sim 2.8 \times 10^{-16}$ erg s^{-1} cm^{-2}, again well above the line flux predicted for this object of 5.6×10^{-18}. Most importantly these upper limits tell us there is really no big disagreement between our observed nondetections and our model predictions of a very faint [O III] line.

To compute the 3σ line flux upper limits quoted above, we added a mock Gaussian emission line to the spectra to represent [O III], similar to the procedure in Finkelstein (Finkelstein et al., 2011b). The sigma of the Gaussian was fixed to 5.52Å, or the σ from our faintest [O III] detection (from LAE27878). We used the error array from the unmodified reduced spectrum. We then measured the mock line by fitting a symmetric Gaussian using MPFITEXPR, as we would for an actual [O III] detection. The noise on the measurement was determined from 1000 Monte Carlo iterations, where the flux was modified each time by a random amount proportional to the error bars (using RANDOMN in IDL). We repeated this measurement with decreasing line fluxes until the signal to noise ratio (SNR) dropped below 5σ. From the line flux where the SNR crossed below the 5σ threshold we were able to determine σ and therefore a 3σ line flux detection limit. However, because it is impossible to know a priori exactly how much the Lyα line is offset from the [O III] line, we had to repeat this calculation, fixing the mock line at different wavelengths to recreate different velocity offsets. We found the 3σ line flux detection limit as describe above at 11 different wavelengths for each object, corresponding to velocity offsets of 0-500 km s^{-1}, in increments of 50 km s^{-1}. This range of velocity offsets was chosen to encompass the magnitude of

Lyα - [O III] velocity offsets we have observed of 52 - 342 km s^{-1}. The 3σ line flux detection limits at each of these 11 locations were then averaged to give an approximate limit for the entire wavelength range.

We contend that in light of the discussion put forth above, the SED modeling discussed in this paper has done a reasonable job of matching our observations, but there is still room for improvement. It is possible that attributing some of the model line flux to the Hβ line, instead of solely to the [O III] would provide an even better match between the observed line fluxes and observed [O III] line fluxes. This can be explored in future work and is beyond the scope of this paper. We also assert that additional spectroscopic observations of LAEs in the NIR are needed, yielding both detections and nondetections, to better quantify exactly how successful this approach can be, beyond what we can say with a sample of only six LAEs. Perhaps most importantly, the predictions of [O III] flux that we have made from the new SED fitting approach in this paper should allow us to select the LAEs that are mostly likely to yield [O III] in future NIR spectroscopic observations. Based on our comparisons of our predicted [O III] line fluxes to the observed line fluxes in the three objects that had [O III] detections - it seems likely that objects with strong [O III] line fluxes predicted would be our best bet for NIR followup observations. This is a testable hypothesis and should allow us to more efficiently use telescope time and more carefully plan appropriate integration times for each object.

3.7.2 Effects of including [O III] emission

As has been pointed out by Schaerer & de Barros (2009) and others, inclusion or exclusion of nebular emission lines during SED fitting can significantly alter the results obtained, specifically masses and ages. To investigate how our

additional [O III] parameter affects our best fit solutions, we compare the best allowed-fit solutions with and without [O III] emission. We focus on the three objects for which we have [O III] measurements, and repeat the same fitting procedure described above, but with the [O III] line flux contribution to the K_s fixed to 0. Unsurprisingly, the object most affected by removing the [O III] parameter is LAE40844. This is unsurprising as this was the LAE with the largest of the three observed [O III] fluxes, and was also fit with largest [O III] flux solution amongst the entire LAE sample. For LAE40844, the best allowed-fit age increases from 4.6 $\times$ 10^6 years with [O III] accounted for, to 6.9 $\times$ 10^6 years when no [O III] contribution to the K_s is allowed (here we are comparing model ages, not star formation weighted ages which are dependent on tau). In other words, failure to properly account for [O III] emission leads to an increase in age of 1.5 times. In addition, the best allowed-fit mass increases from 1.9 $\times$ 10^9 $M_\odot$ ([O III] included) to 3.5 $\times$ 10^9 $M_\odot$when [O III] emission is not included. So the best allowed-fit mass solution in this object increases 1.8 times when [O III] is not properly accounted for. Perhaps most tellingly, the reduced χ^2 value increases from 10.5 to 77.0 when the [O III] contribution is removed, indicating that the fit without an [O III] contribution is quite poor. These increases in mass and age are in excellent agreement with those reported in Schaerer & de Barros (2009). Figure 3.5 illustrates the difference between the models when [O III] flux is and is not included.

LAE27878 and LAE7745 are the other two objects with measured [O III] fluxes, but their results with and without [O III] are not quite as clear cut. Both LAE7745 and LAE27878 have negative best allowed-fit tau parameters when [O III] flux is considered. How age and mass solutions behave when you exclude nebular emisison in objects fit with negative tau values has not been previously investigated. In these objects, we find that when [O III] flux is fixed to zero, both

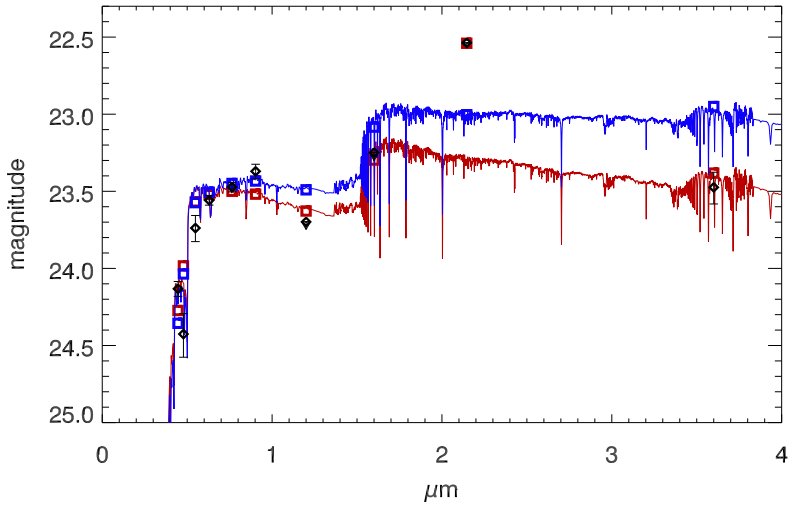

Figure 3.5 Observed magnitudes are in black. The best allowed-fit solution with an [O III] contribution is shown with red spectrum and red squares, the best fit solution with with no [O III] line flux is shown with blue spectrum and blue squares. In addition to yielding an older and more massive solution, the blue spectrum is a much poorer fit.

objects instead find positive best allowed-fit tau solutions. Subsequently, the best allowed-fit ages and masses in both these objects decrease, rather than increase. But, in spite of these increases, the reduced χ^2 value also increases for both objects, when [O III] is excluded. For LAE7745, the reduced χ^2 increases by only $\sim$ 1%, for LAE7745, the percent difference is larger at $\sim$ 88%.

We present the overall trends for the changes in age, mass and reduced χ^2 for the entire sample of LAEs in Figure 3.6 when [O III] flux is and is not included in the fitting process. The histograms in Figure 3.6 present the percent difference between the solution with [O III] and the solution without [O III]. In all three histograms a positive percent difference means the solution without [O III] was larger, a negative percent difference means the solution with [O III] was larger. The two most definitive trends are seen in the histograms for mass and reduced χ^2. Overall, the solutions without [O III] are more massive, as seen by the fact that most of the percent differences in this panel are positive. 18 solutions become more massive, 8 stay the same, and only 7 get let massive. The reduced χ^2 results are even clearer, every χ^2 value gets bigger or stays the same, none get smaller. More precisely, 25 solutions get bigger and 8 stay the same. The trend in the age results is not quite as definitive, 15 solutions don't change, while 9 get older and 9 get younger. So overall we can say that when [O III] contributions to the K_s band are not included, the sample becomes more massive and less well fit, even when increasing star formation histories are allowed. The magnitude of these effects, however, can vary significantly from object to object within a sample. Some less definitive changes in ages can be expected as well.

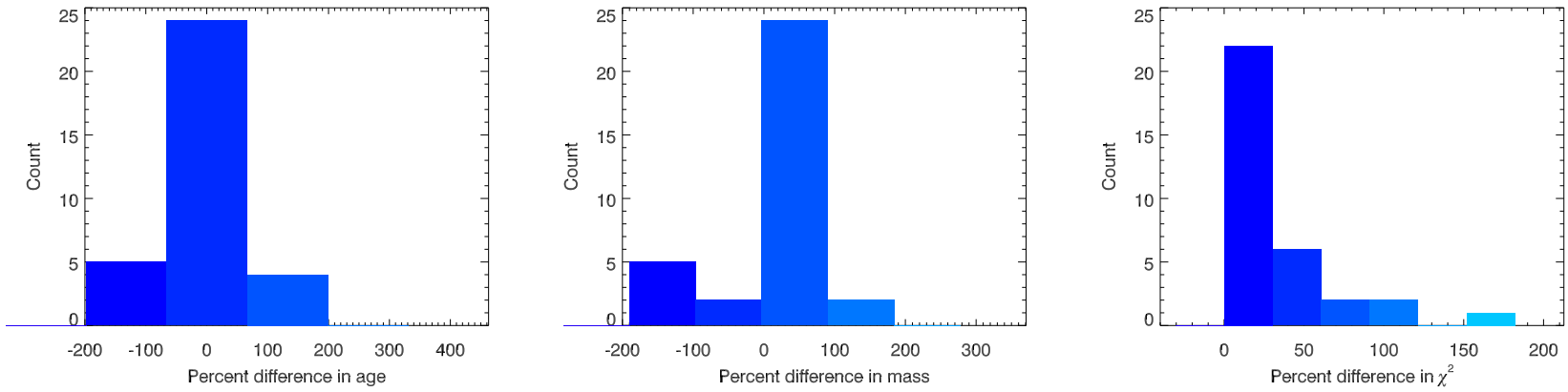

Figure 3.6 Percent difference between best allowed-fit solutions in full LAE sample, when [O III] line flux contributions are and are not included in the fitting process. A positive percent difference means the solution without [O III] was larger, a negative percent difference means the solution with [O III] was larger. Overall, when [O III] contributions to the K_s band are not included, the sample becomes more massive and less well fit, even when increasing star formation histories are allowed with some less definitive changes in ages be expected as well - see text for further details.

3.7.3 Comparison of physical characteristics to other samples

Table 3.5 shows best-fit age and mass results from the majority of recent papers on SED fitting of LAEs from z $\sim$ 0.3 – 6.6, including the results of this paper. The majority of papers to which we can compare our current results don't account for nebular emission lines, although the most current papers due consider contributions from these lines and this is likely becoming the standard. We note which models were used in each paper, but the reader should also consider that star formation histories and metallicities are sometimes treated differently from paper to paper (i.e. in some cases these are fixed parameters, in others they are free).

Focusing specifically on the z $\sim$ 3.1 samples detailed in Table 3.5, we find the results vary substantially from sample to sample. We find that our sample of 33 individually fit LAEs has a systematically more massive solution than all the stacked samples at z $\sim$ 3.1, even in the samples where nebular emission lines were not treated during the fitting process. Our median mass from individually fit LAEs is larger than the stacked results from other authors, but it's possible stacked analyses may not be capturing this true diversity we see in our sample.

In addition, there are a number of systematic differences between the samples that may indicate that our results do not necessarily contradict the other works to which we are comparing, but rather we may be probing different subsamples of LAEs. (1) As we alluded to earlier, given the wide-field and correspondingly shallow nature of our narrowband survey, we have selected a subset of bright LAEs, brighter than many surveys to which we can compare in Table 3.5. L^* for z $\sim$ 3.1 LAEs is $\sim 5.75 \times 10^{42}$ erg s^{-1} (Ciardullo et al., 2012). The majority of our sample is above this luminosity, as illustrated in Figure 3.7, where our average

$L_{Ly\alpha}$ luminosity is $\sim 1.53 \times 10^{43}$ erg s^{-1}. This is in contrast, for instance, to the z $\sim$ 2.1 and 3.1 LAEs selected from the deep MUSYC survey (Gawiser et al., 2007; Lai et al., 2008; Guaita et al., 2011) where the area surveyed was much smaller but the 5σ narrowband depth reached magnitudes of 25.4 and 25.1 for z $\sim$ 3.1 and z $\sim$ 2.1, respectively. We have analyzed the effect of $L_{Ly\alpha}$ on the SED-derived masses in Figure 3.7 in a subset of samples from z $\sim$ 0.3 – 3.1 from Table 3.5 where $L_{Ly\alpha}$ information readily available. L^* for z $\sim$ 0.3 is taken from Cowie et al. (2010), and L^* at z $\sim$ 2.1 comes from Ciardullo et al. (2012). This preliminary analysis indicates that individually fit LAEs have larger masses than the masses derived from stacked analysis. Also the stacked LAEs from the deeper MUSYC data have smaller masses than those LAEs in our wide-field survey.

We cannot make a similarly broad statement about any systematic offset when comparing our age results to the stacked age results at z $\sim$ 3.1. Acquaviva et al. (2012) and Gawiser et al. (2006, 2007) have younger solutions for their stacked samples than our average from individually fit LAEs, while Nilsson et al. (2007) find a solution eight times older than our average, with constant star formation assumed, but various metallicities allowed. The Acquaviva et al. (2012) fitting procedure assumes constant star formation, but metallicity is allowed to vary; the Gawiser et al. (2006) sample was also fit with a constant star formation but with metallicity fixed to solar. Gawiser et al. (2007) used a two-burst scenario for their star formation history, and metallicity was allowed to vary. Lai et al. (2008) on the other hand, in spite of being a stacked sample, with no treatment of nebular emission lines and assuming constant star formation and solar metallicity, finds a very similar average age of 160 Myr compared to our average of 180 Myr. We once again note, however, that our full range of age solutions (1.1-1100 Myr) does encompass the all the average ages put forth by other authors for their stacked

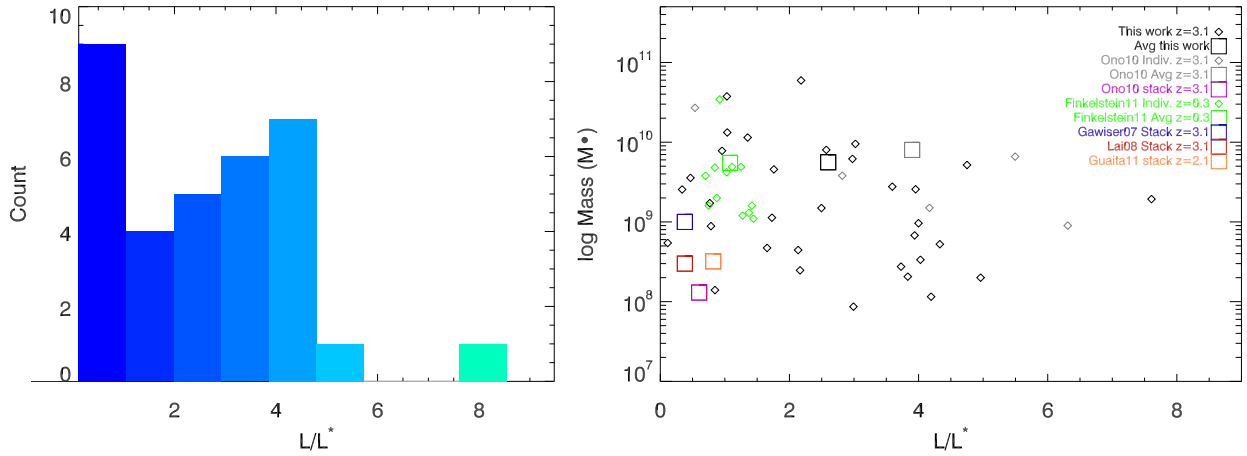

Figure 3.7 Left: Histogram of L/L^* for present sample. Right: Derived masses as a function of the ratio of L/L^*. Individual results from this paper are shown as small black diamonds, an average value from this work is indicated with a large black square, 12 individual $z \sim 0.3$ LAEs from Finkelstein et al. (2011b) are shown as green diamonds, a large green square indicates the average value from Finkelstein sample, small grey diamonds are 5 individual $z \sim 3.1$ LAEs from Ono et al. (2010) and the large grey square shows the average value of the Ono sample, large magenta square is the result from the 200 stacked $z \sim$ LAEs in Ono et al. (2010), red and blue squares are the same stack of 52 LAEs at $z \sim 3.1$ from Lai et al. (2008); Gawiser et al. (2007) fit with different star formation histories, orange square is the stack of 216 $z \sim 2.1$ LAEs from Guaita et al. (2011).

samples. We acknowledge that the variety of methods used by different authors can make direct comparison somewhat difficult, but it is worth trying to catalog the various results and compare to the extent we are able.

Ono et al. (2010) presents the only other sample of individually fit LAEs at $z \sim 3.1$, albeit in a sample of only five objects, to which we can compare. The fitting procedure of Ono et al. (2010) includes an assumed metallicity of $Z = 0.2$ $Z_{\odot}$ the star formation history can be constant or decreasing exponentially, and no treatment of nebular lines is included. In spite of these differences we find great agreement between their ranges for both mass and age and those that we have presented for our sample. They find (as we do) a large range of ages, 4.8–407 Myr (1.1-1100 Myr), and masses, 9.3×10^{8}–2.7×10^{10} $M_{\odot}$(1.1×10^{8} – 1×10^{11} $M_{\odot}$). The fact that this individually fit sample is the only one that matches our results well may lend further credence to the idea that stacked analyses may not be capturing the diversity that we have found in the LAE population at this redshift. We also note that there is broad agreement between our individually fit LAEs at $z \sim 3.1$ and the 40 individually fit LAEs of Cowie et al. (2011) at $z \sim 0.3$. The age and mass spread of the two samples is quite similar, except, of course, the fact that there are older possible ages allowed for galaxies in the $z \sim 0.3$ universe compared to the $z \sim 3.1$ universe. The Cowie et al. (2011) fitting procedure fixes metallicity to solar, but various exponentially decreasing star formation histories are considered. Such agreement between two samples far removed from one another in cosmic time may suggest that Lyα selection techniques are capturing similar objects, at similar states of evolution, regardless of the redshift sampled. The broad agreement may also be a result of the similar $L_{Ly\alpha}$ space probed by the $z \sim 0.3$ sample and our sample, as the $z \sim 0.3$ sample has a rather large average L/L^{*} value of ~ 1.6 (using L^{*} from Cowie et al. (2010)).

Author	Redshift	Sample	Models	Neb. Em.[1]	Results
Acquaviva 2011	$z \sim 2.1$	216 stacked	CB11	yes	50 Myr, 3×10^8 $M_\odot$
	$z \sim 3.1$	70 stacked	CB11	yes	1000 Myr, 1.5×10^9 $M_\odot$,
Cowie 2011	$z \sim 0.3$	40 individual	BC03	yes	10–10000 Myr, 10^7–10^{11} $M_\odot$
Finkelstein 2007	$z \sim 4.5$	98 stacked[2]	BC03	Lyα	1–40 Myr, 0.68–16.2×10^8 $M_\odot$
Finkelstein 2009	$z \sim 4.5$	14 individual	BC03	Lyα, Hα	3-500 Myr, 1.6×10^8–5.0×10^{10} $M_\odot$
Finkelstein 2011	$z \sim 0.3$	12 individual	BC07	yes	300 Myr, 4×10^9 $M_\odot$
Gawiser 2006	$z \sim 3.1$	40 stacked	BC03	no	90 Myr, 5×10^8 $M_\odot$
Gawiser 2007	$z \sim 3.1$	52 stacked	BC03	no	20 Myr, 1×10^9 $M_\odot$
Guaita 2011	$z \sim 2.1$	216 stacked	CB10	no	10 Myr, 3.2×10^8 $M_\odot$
Lai 2008	$z \sim 3.1$	76 stacked	BC03	only Lyα	160 Myr, 3×10^8 $M_\odot$
McLinden 2012 (this paper)	$z \sim 3.1$	33 individual	CB11	yes, see Sec. 3.5	1.1-1100 Myr, 1.1×10^8 – 1×10^{11} $M_\odot$
Nakajima 2012[5]	$z \sim 2.2$	304 stacked	BC03	yes	12.6 Myr, 3×10^8 $M_\odot$
	$z \sim 2.2$	55 stacked	BC03	yes	8.3 Myr, 5×10^8 $M_\odot$
Nilsson 2007	$z \sim 3.15$	23 stacked	BC03	no	830 Myr,[3] 8×10^8 $M_\odot$
Nilsson 2011	$z \sim 2.3$	40 stacked	NisseFit[4]	yes	440 Myr, 2.5×10^{10} $M_\odot$
	$z \sim 2.3$	40 individual	NisseFit[4]	yes	1000 Myr, 1.7×10^{10} $M_\odot$
Ono 2010a	$z \sim 3.1$	200 stacked	BC03	no	65 Myr, 1.3×10^8 $M_\odot$
	$z \sim 3.1$	5 individual	BC03	no	4.8–407 Myr , 0.93–27×10^9 $M_\odot$
	$z \sim 3.7$	61 stacked	BC03	no	5.8 Myr, 3.2×10^8 $M_\odot$
	$z \sim 3.7$	6 individual	BC03	no	1.4–900 Myr, 3.9–51×10^9 $M_\odot$
Ono 2010b	$z \sim 5.7$	165 stacked	BC03	yes	3 Myr, 3×10^7 $M_\odot$
	$z \sim 6.6$	91 stacked	BC03	yes	1 Myr, 1×10^8 $M_\odot$
Pirzkal 2007	$z \sim 4$–5.7	9 individual	BC03	no	0.5 – 20 Myr, 5×10^6 – 18×10^8 $M_\odot$

Table 3.5 Comparison of SED fitting results

[1] Was nebular emission accounted for?

[2] Divided into 6 subsamples

[3] Author notes this is poorly constrained

[4] Based on BC03

[5] Two different stacks for two different fields at $z \sim 2.2$

3.8 Conclusions

We have presented one new [O III] detection in a z $\sim$ 3.1 LAE. Combining this new detection with the two we presented in Mc11, we are able to present a total of three measurements of the velocity offset between Lyα and [O III] in these LAEs, ranging from 52 – 342 km s^{-1}. This new result is still consistent with the outflow models explored in Mc11.

In addition to the new [O III] detection, we have put forth a new method to account for nebular emission in high-z starbursting galaxies. We have individually fit 33 z $\sim$ 3.1 LAEs using this powerful yet simple method to account for nebular emission contributions to SED. From these fits we find constraints on age, mass, dust content, metallicity, star formation history, and [O III] line flux. We find that our sample has quite diverse characteristics, but some generalizations can be made. For instance, a majority of the galaxies are fit with a single instantaneous burst or exponentially decreasing star formation history. As a whole, the sample has only moderate amounts of dust, and sub-solar metallicity. Mass and age solutions vary widely, but median values of 450 Myrs and 1.5 $\times$ 10^{9} M$_{\odot}$ are found. Finally, most of the galaxies are best fit with an [O III] line contributing additional flux to the K$_{s}$ band, with an average flux of 2.8 $\times$ 10^{-17} erg s^{-1} cm^{-2}.

The [O III] line strength predictions from our new SED fitting methodology have reasonably matched the observations of the [O III] line in the six objects for which we can make this comparison. These predictions gives us confidence that these results can be used to select the LAEs mostly likely to yield [O III] detections in future NIR observations. Further observations of LAEs in the NIR will allow us to fill in the distribution of velocity offsets found in LAEs at this redshift, and will allow us to further test the validity of [O III] line strength predic-

tions from our SED process. In the meantime we have, with this work, provided a comprehensive picture of LAE characteristics in a large sample of individually examined objects.

ACKNOWLEDGEMENTS

Thanks to NOAO for loaning the KPNO [O III] filter for use on the Bok Telescope. This work has been supported by NASA (Keck grant number), and by the National Science Foundation through NSF grant AST-0808165. Additional thanks to Dr. Seth Cohen for many helpful discussions.

Some of the data presented herein were obtained at the W.M. Keck Observatory, which is operated as a scientific partnership among the California Institute of Technology, the University of California and the National Aeronautics and Space Administration. The Observatory was made possible by the generous financial support of the W.M. Keck Foundation.

The authors wish to recognize and acknowledge the very significant cultural role and reverence that the summit of Mauna Kea has always had within the indigenous Hawaiian community. We are most fortunate to have the opportunity to conduct observations from this mountain.

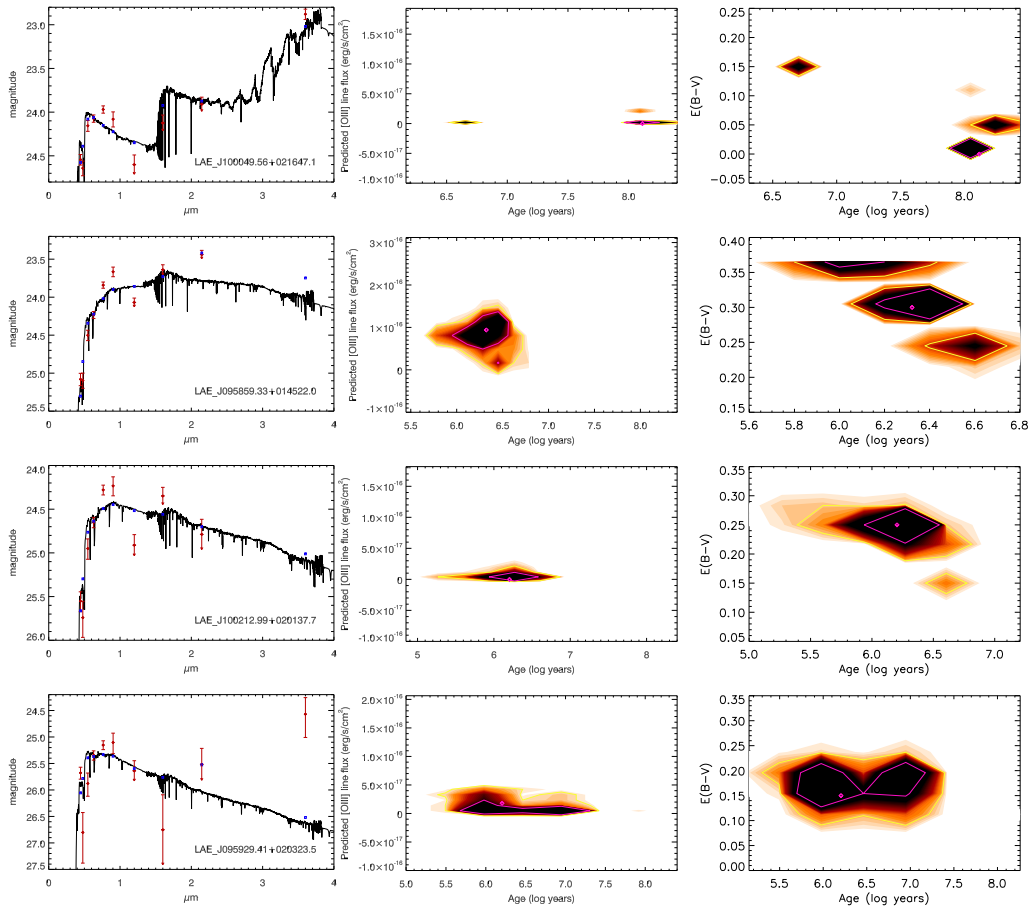

Figure 3.8 The first column contains the best allowed-fit model spectra for the first five LAEs (order of objects in Figure 3.8 - Figure 3.14 matches the order of objects in Table 3.2. Model spectra are black, model magnitudes are shown as blue squares, observed magnitudes are shown as red diamonds and red diamonds with a downward arrow instead of error bars indicates that an observed point was fainter than the 3σ depth in that band -large error bars in V and g′ bands are sometimes a consequence of subtracting the Lyα line from these filters). The second column and third columns show density plots from our MC simulations where the best allowed-fit is shown as a magenta diamond, contours encompassing $\sim$ 68% and $\sim$ 95% of the results are shown in magenta and yellow, respectively.

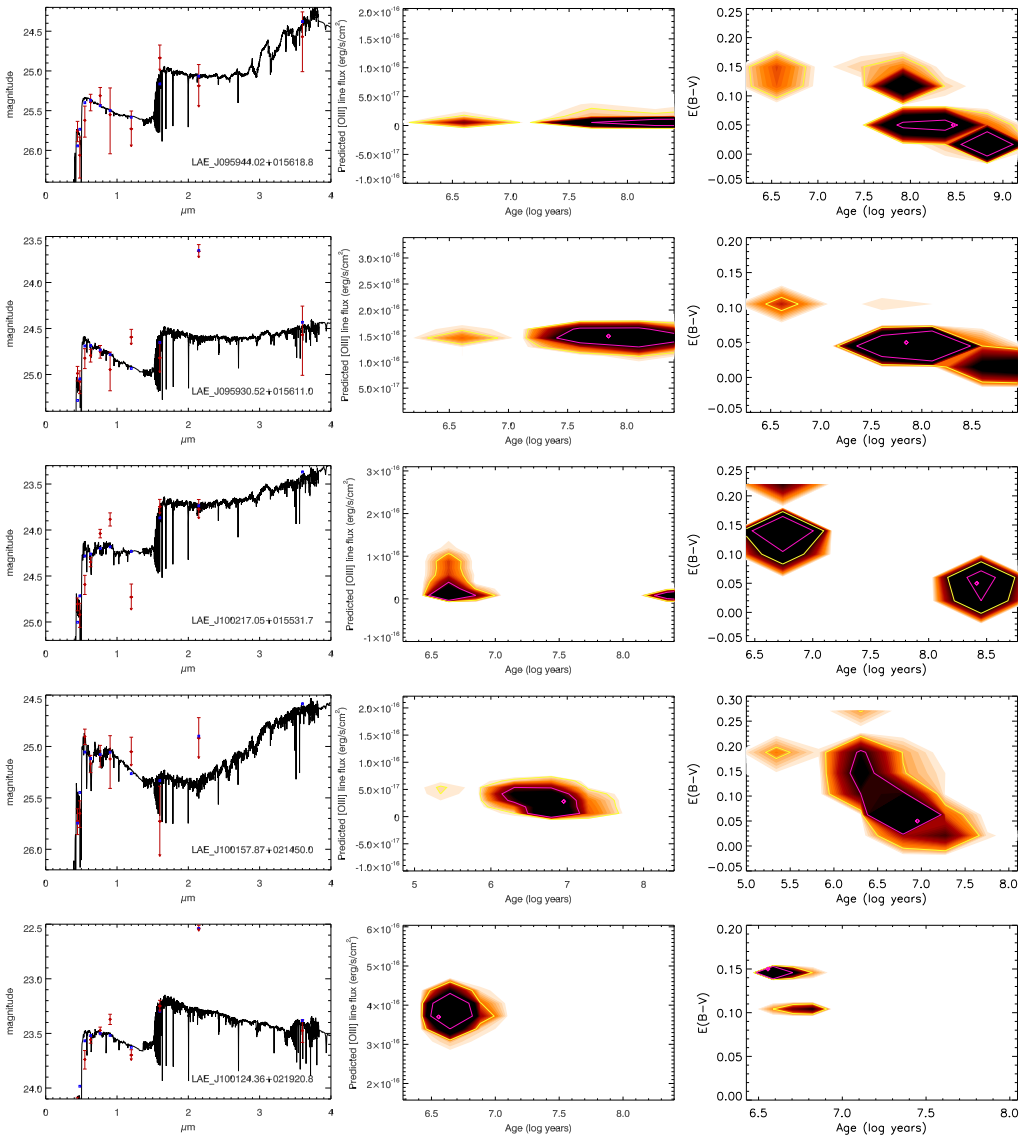

Figure 3.9 Same as Figure 3.8 for next 5 objects.

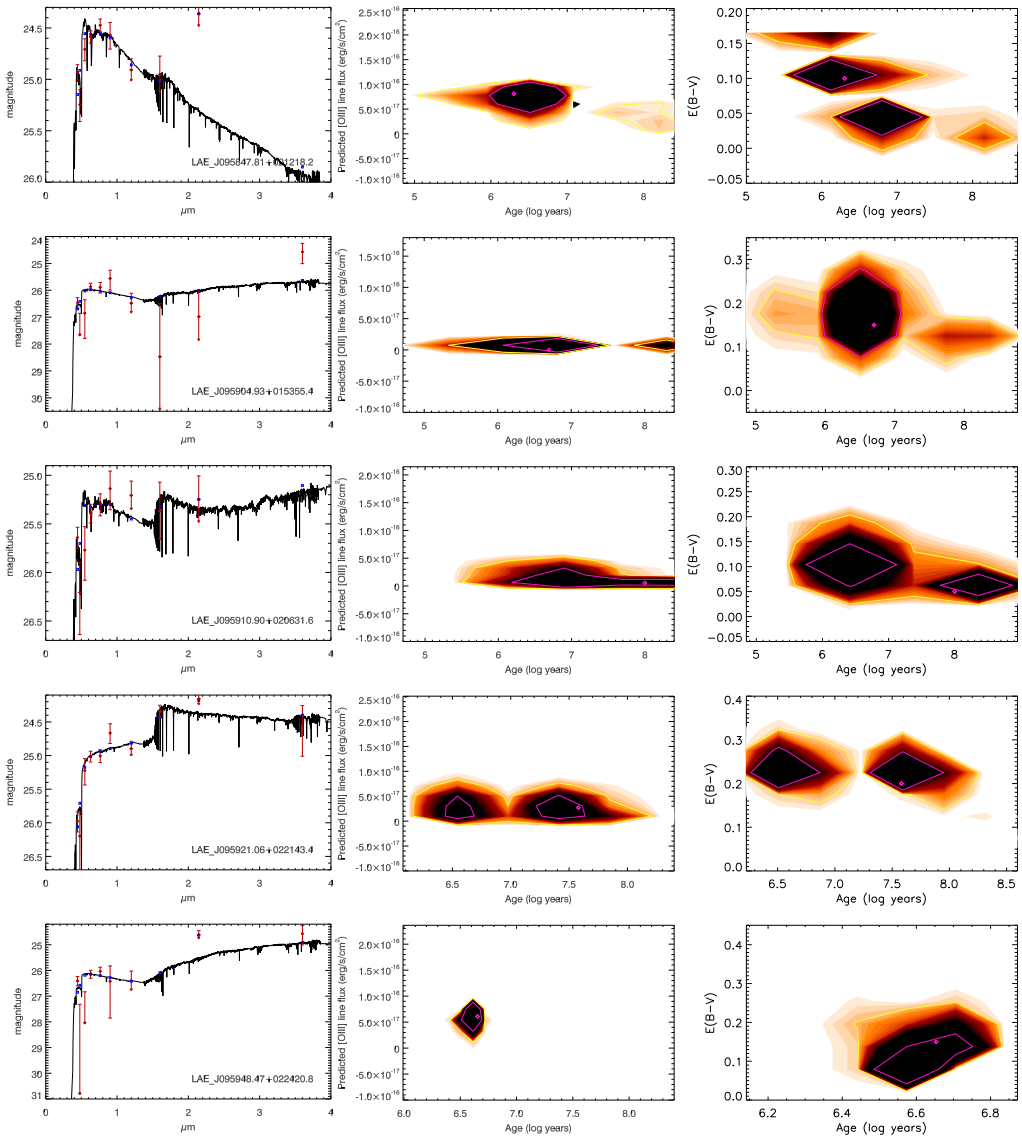

Figure 3.10 Same as Figure 3.8 for next 5 objects.

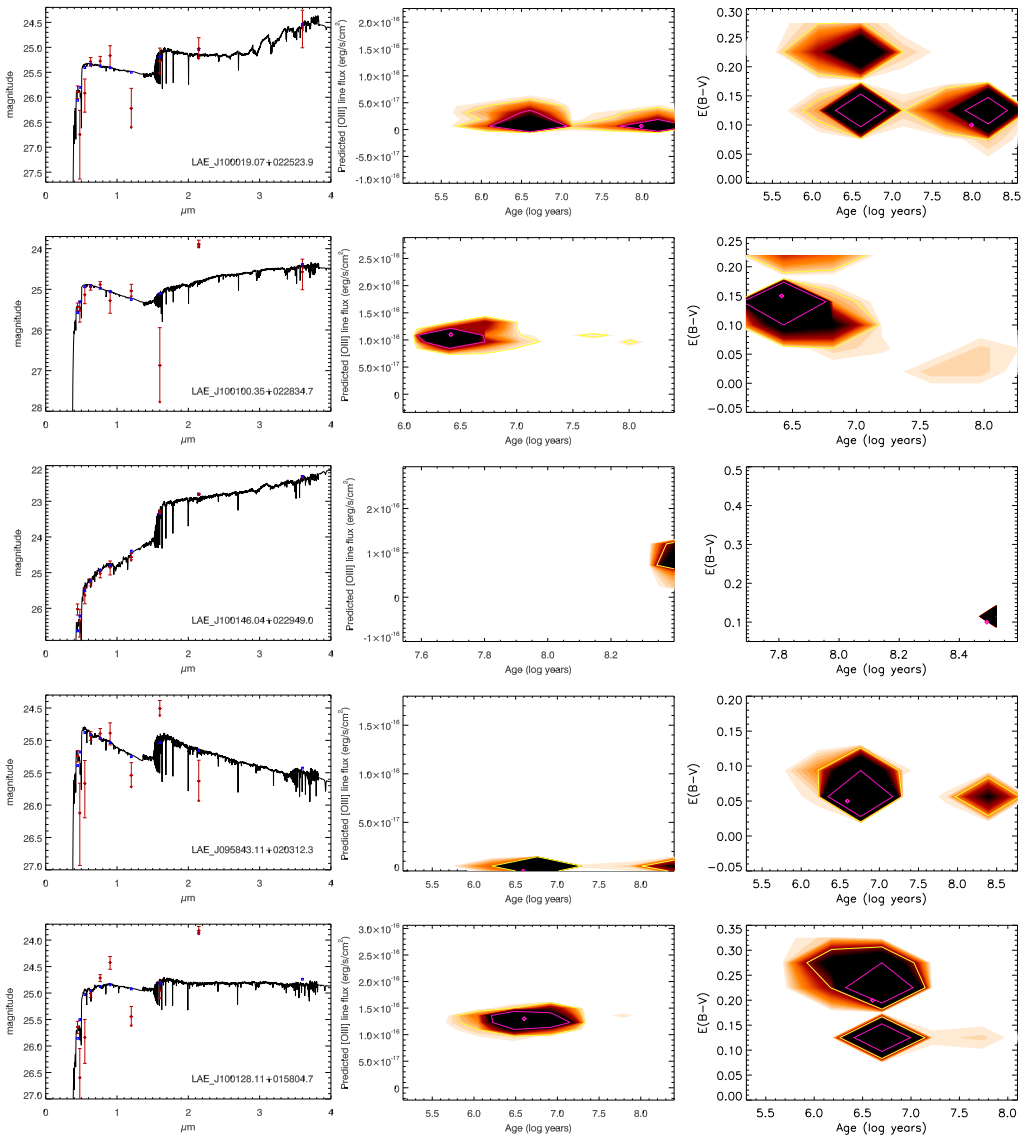

Figure 3.11 Same as Figure 3.8 for next 5 objects.

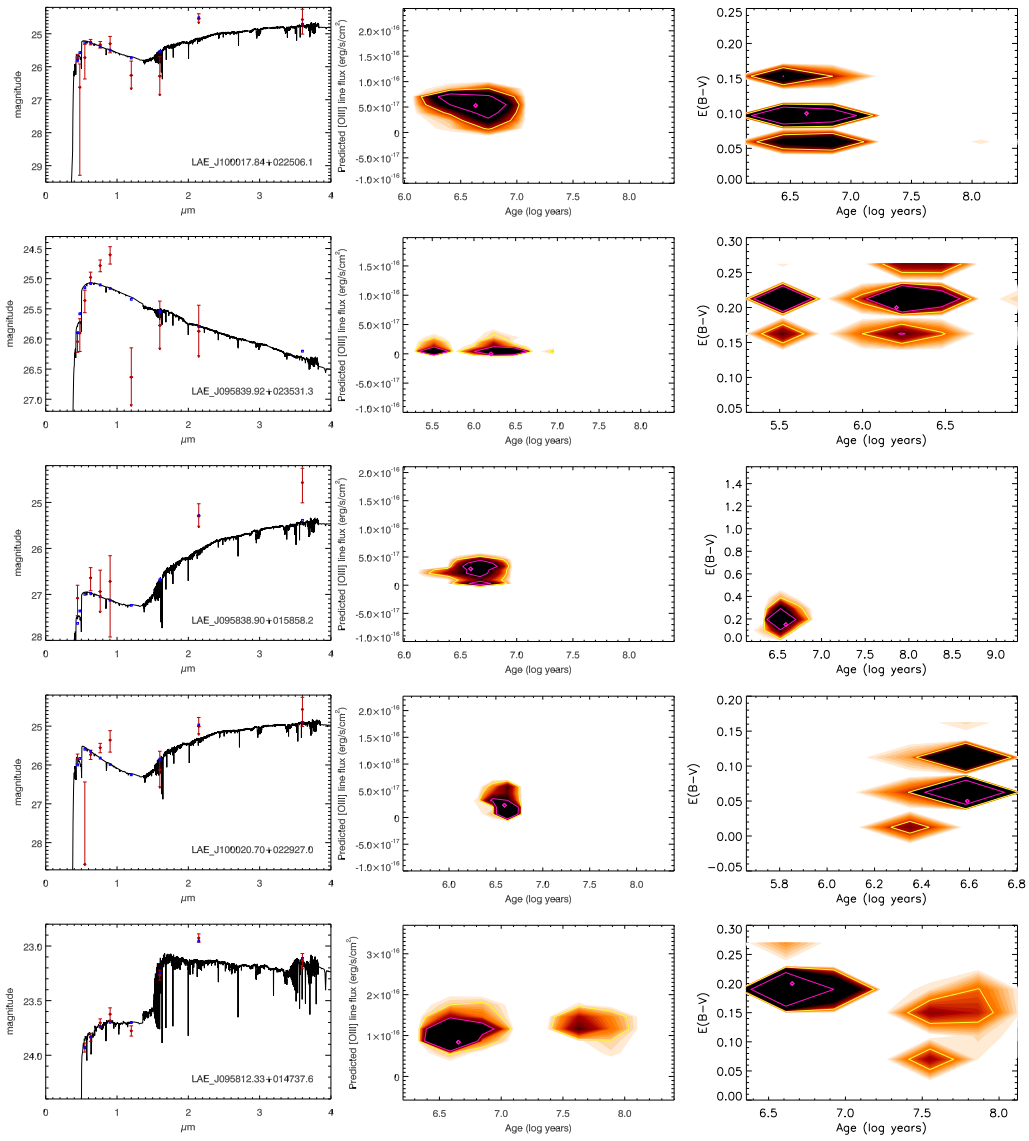

Figure 3.12 Same as Figure 3.8 for next 5 objects.

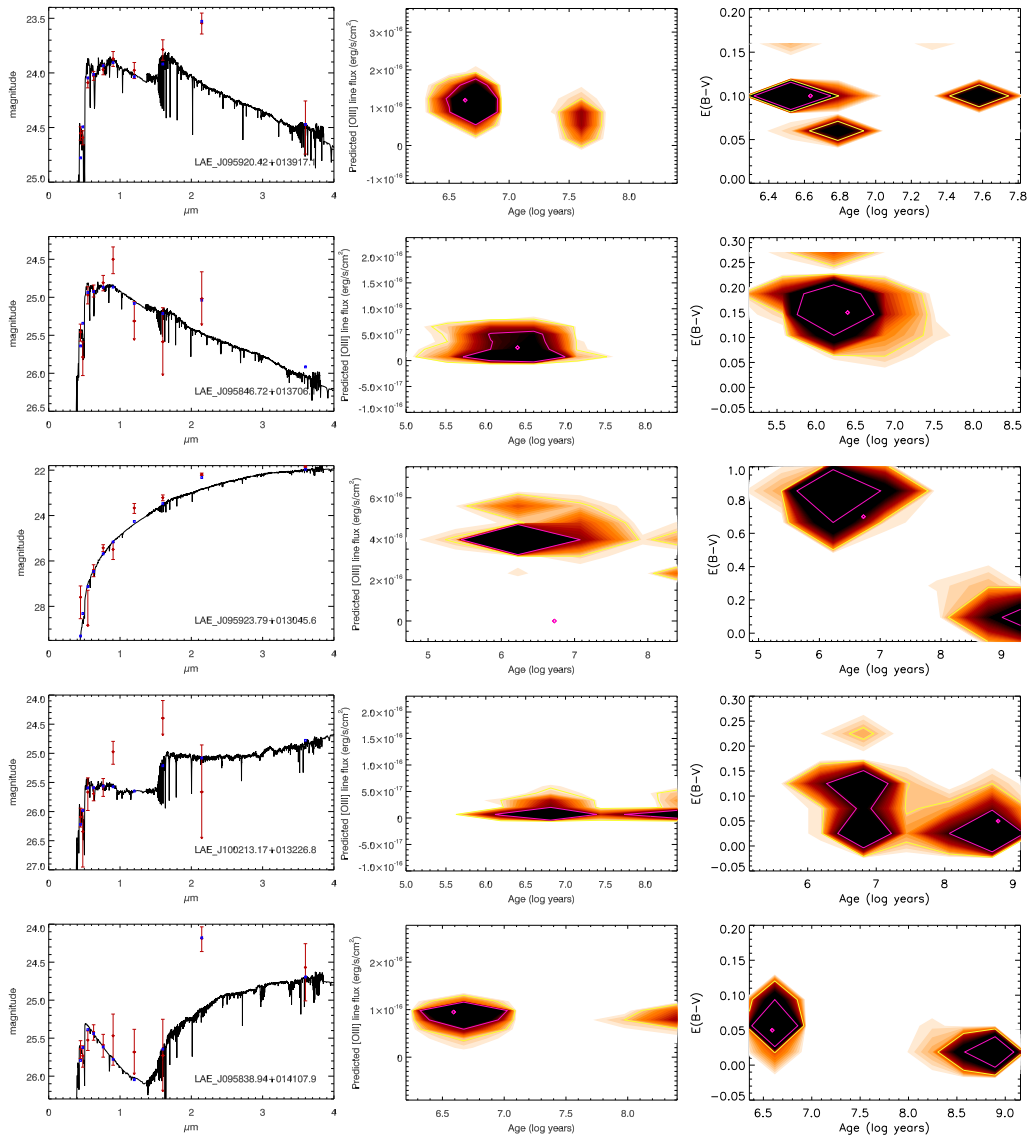

Figure 3.13 Same as Figure 3.8 for next 5 objects.

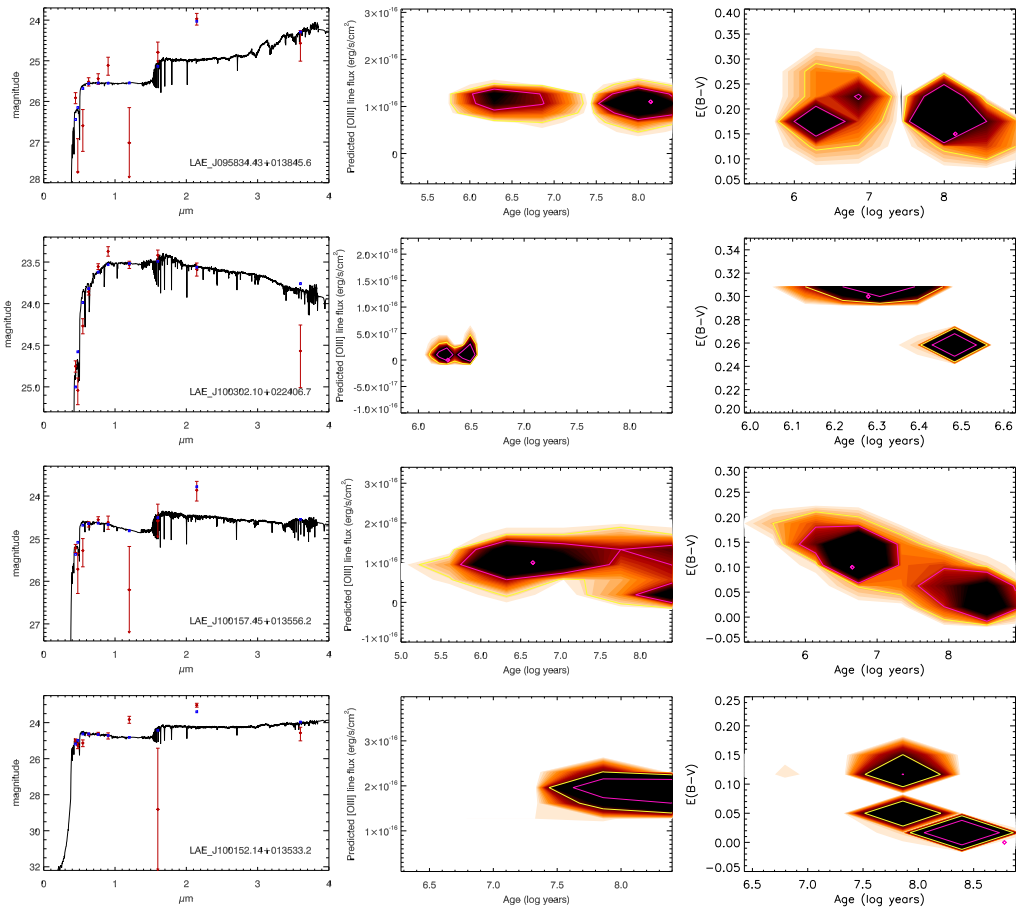

Figure 3.14 Same as Figure 3.8 for next 4 objects.

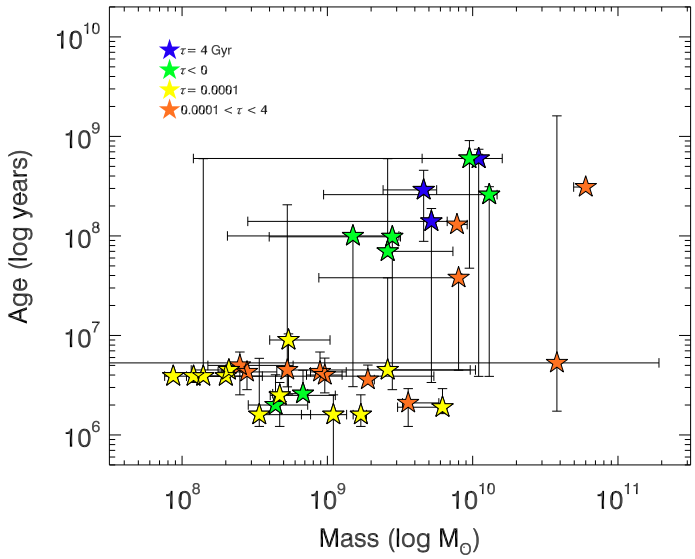

Figure 3.15 The distribution of age$_{SFR}$ versus mass fits for 33 LAEs. Blue stars are fits with continuous star formation ($\tau_{sfr} = 4$ Gyr), green stars indicate models with exponentially increasing star formation rates ($\tau < 0$), yellow stars are fits with a single instantaneous burst ($\tau_{sfr} = 0.0001$ Gyr), and orange stars are those with exponentially decaying star formation rates. Since mass and age parameters are correlated this plot is mainly meant to illustrate and confirm the distribution of τ_{sfr} with these parameters, showing that the oldest and most massive LAEs are those fit with continuous or increasing star formation rates, the youngest and least massive galaxies are fit with instantaneous star formation histories, and those LAEs with exponentially decaying star formation rates lie between those two populations.

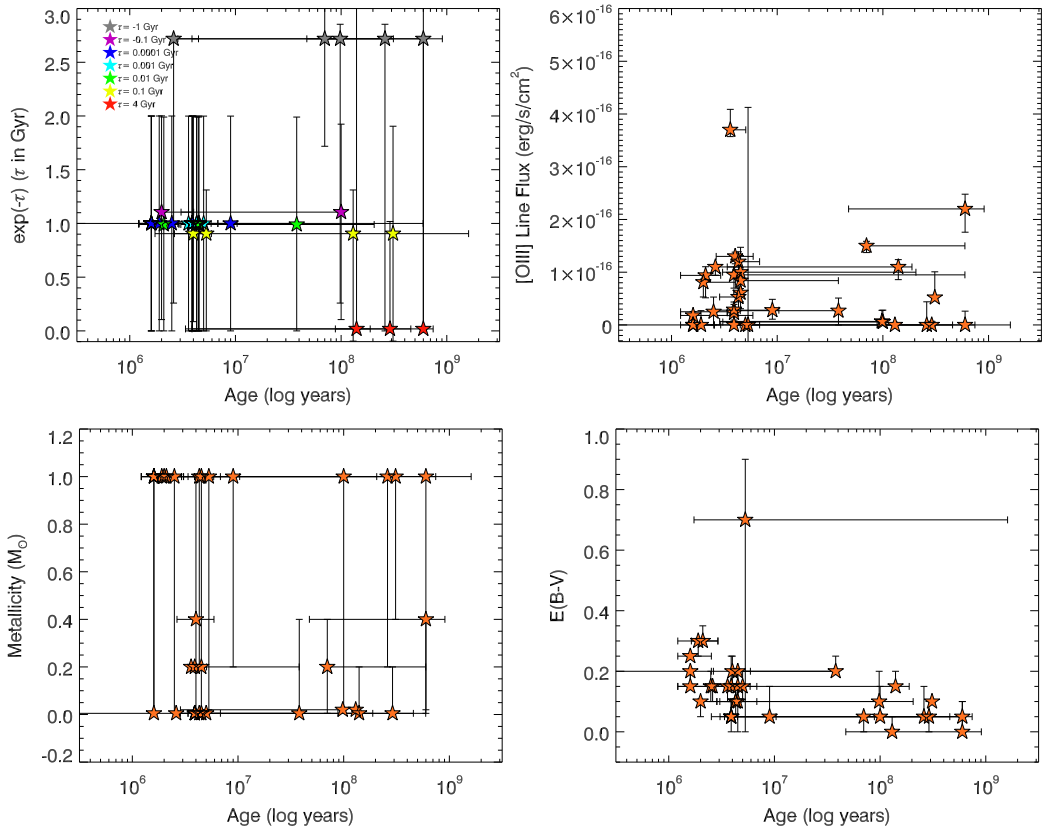

Figure 3.16 Top panel shows distribution of τ_{sfr} versus age and [O III] line flux versus age fits, from left to right. Bottom panel shows these distributions for metallicity versus age and E(B-V) versus age, from left to right. Blue stars in figure at top left are those with tau < 0, shown at their correct ages, but (arbitrarily) placed at 10^{-6}.

Chapter 4

[O III] EMISSION AND GAS KINEMATICS IN A LYMAN-ALPHA BLOB AT Z $\sim$ 3.1

4.1 Abstract

We present spectroscopic measurements of the [O III] emission line from two subregions of strong Lyα emission in a radio-quiet Lyman-alpha blob (LAB). The blob under study is LAB1 (Steidel et al., 2000) at z $\sim$ 3.1, and the [O III] detections are from the two Lyman break galaxies embedded in the blob halo. The [O III] measurements were made with LUCIFER on the 8.4m Large Binocular Telescope and NIRSPEC on 10m Keck Telescope. Comparing the redshift of the [O III] measurements to Lyα redshifts derived from the work of Weijmans (2010) allows us to study the kinematics of the gas in the blob. Using both LUCIFER and NIRSPEC we consistently find velocity offsets between the [O III] and Lyα redshifts consistent with 0 km s^{-1} in both subregions studied (ranging from -43.88 $\pm$ 69.01 – 36.58 $\pm$ 63.85 km s^{-1}). We discuss the possible implications of this result, as it could downplay the role of winds and outflows in powering the Lyα emission in this LAB, since a velocity offset between nebular emission lines and Lyα are often interpreted as evidence of large-scale outflows (McLinden et al., 2011). In addition, we present an [O III] line flux upper limit on a third region of LAB1, a region that is unassociated with any underlying galaxy. We find that the [O III] upper limit from the galaxy-unassociated region of the blob is at least 2.5 times fainter than the [O III] flux from a LBG-associated region and has an [O III]

to Lyα ratio measured at least 3.4 times smaller than the same ratio measured from one of the LBGs.

4.2 Introduction

Lyman-alpha (Lyα) first became a useful tool for observing high-z sources with the discovery of large samples of Lyα emitting galaxies (LAEs) (Cowie & Hu, 1998; Hu et al., 1998; Rhoads, 2000). The same narrowband imaging techniques that uncovered LAEs began uncovering a different set of objects that were also very bright in Lyα. These rarer, more extended, and more luminous objects are what we now call Lyα blobs (LABs) (e.g., Steidel et al., 2000; Matsuda et al., 2004; Dey et al., 2005; Nilsson et al., 2006). LABs are extremely large ($\sim$ 30–200 kpc) radio-quiet Lyα nebulae in the high redshift universe LABs are highly luminous ($L_{Ly\alpha} \sim 10^{43-44}$ ergs s^{-1}), and yet despite rigorous study in the last decade, the mechanism(s) that power this immense Lyα flux is not fully understood. This paper will focus on investigating the kinematics of and mechanisms powering such objects by investigating LAB1, a z $\sim$ 3.1 LAB first discovered by Steidel et al. (2000).

There are currently three most widely discussed scenarios to explain both the large spatial extent and powerful Lyα flux of these blobs. The first of these is that the gas in LABs is heated by photoionization from massive stars and/or AGN (Geach et al., 2009). A second scenario proposes that gas in LABs is excited by cooling flows / cold accretion (Haiman et al., 2000; Dijkstra & Loeb, 2009). Finally some authors have proposed LABs originate from overlapping supernova remnants from massive stars after a powerful starburst (Taniguchi & Shioya, 2000; Ohyama et al., 2003) producing superwinds.

Adding to the controversy, observations in recent years from different authors have led to different conclusions about which of these scenarios are responsible for said observations. Nilsson et al. (2006) have argued that their observations of a z $\sim$ 3.16 LAB were best matched by cooling flows onto a dark matter halo. This is in contrast to the conclusions of Hayes et al. (2011), who found evidence of polarized Lyα radiation in LAB1. The Hayes et al. (2011) results suggest that Lyα photons are scattered at large radii from their production sites and this observation seems to not only favor the role of scattering in outflows in LABs, but the authors contend their discovery can actually rule out most inflow models. But a similar study by Prescott et al. (2011) found no evidence of polarization in a LAB at z $\sim$ 2.656 and these authors argue their results are inconsistent with spherical outflows and Lyα scattering from nearby AGN. Yet another conclusion is reached by Yang et al. (2011) whose observations of Lyα and Hα emission in a z $\sim$ 2.3 LAB rule out simple infall models and models that rely on large outflows. This diversity of conclusions may mean that there are diverse mechanisms powering different blobs (or multiple mechanisms at play in single blobs) or it mean that truly conclusive observations have not yet been presented.

To try to provide new data to differentiate amongst the possible LAB sources we focus, as indicated above, on LAB1 (Steidel et al., 2000). LAB1 resides in SSA22, extends $\sim$ 100 kpc (Weijmans, 2010) and has a Lyα luminosity of 1.1×10^{44} erg s^{-1} (Matsuda et al., 2004). This makes LAB1 the brightest and most spatially extended LAB yet observed (Weijmans, 2010). LAB1 is comprised of five separate regions of Lyα emission known as C11, C15, R1, R2, and R3 (see Figure 1 of Weijmans et al (2010)). C11 and C15 are both Lyman break galaxies (LBGs) identified by Steidel et al. (2000). R3 has been identified as an extremely red galaxy (Geach et al., 2007) and may be associated with a bright submillime-

ter source and nearby radio source(Chapman et al., 2001, 2004; Weijmans, 2010). R1 and R2 are not identified with galaxies (Weijmans, 2010). Geach et al. (2009) also demonstrated that AGN activity is not significant in LAB1 as LAB1 is not detected in a 400 ks Chandra exposure.

In this paper we present new spectroscopic [O III] observations of LAB1. We focus on the two Lyα subregions C15 and C11, the two parts of the larger LAB1 structure in which we detected [O III]. The use of [O III] to study the kinematics of LAB1 is powerful because [O III] is not subject to resonant scattering as Lyα is. Comparing [O III] to Lyα emission allows us to characterize any systemic offsets between Lyα and [O III], and thereby detect the presence of outflows or inflows. We first demonstrated the efficacy of this method in a sample of LAEs in McLinden et al. (2011).

Our new [O III] data presented here is compared to Lyα data presented in Weijmans (2010). Weijmans (2010) measured Lyα from each of the 5 subregions in LAB1 with the integral field spectrograph SAURON over 23.5 hours (including 9 hours of SAURON data originally obtained by Bower et al. (2004)). Weijmans (2010) produced both 1D Lyα line profiles of the subregions of LAB1 and Lyα kinematic maps of the subregions, both data products that are useful for comparison to our new [O III] data from LAB1. Henceforth we refer to Weijmans (2010) as W10.

In Sections 4.3 and 4.4 we present our [O III] detections from two near-infrared (NIR) spectrographs (NIRSPEC and LUCIFER). In Section 4.5 we look for any velocity offsets between our measured [O III] redshifts and those of Lyα to look for any evidence of inflows or outflows and in Section 4.6 we discuss the implications of our results ($\Delta v \sim 0$), compare our results to other authors and explore if there are any Lyα radiative transfer models that can match our results.

Where relevant, we adopt the standard cosmological parameters $H_0 = 70$ km s^{-1} Mpc^{-1}, $\Omega_m = 0.3$, and $\Omega_\Lambda = 0.7$ (Spergel et al., 2007). We use the following vacuum wavelengths, 1215.67 Å for Lyα, 3727.092/3729.875 Å for [O II], 4862.683 Å for Hβ, and 4960.295/5008.240 for [O III] from the Atomic Line List v2.04[1].

4.3 NIRSPEC data and reduction

We initially detected [O III] emission from LAB1 using the near-infrared spectrograph NIRSPEC (McLean et al., 1998) on the 10m Keck II telescope on 6 August 2010 (UT). We used the low-resolution mode of NIRSPEC, with the 42 x 0.76″ slit and the NIRSPEC-6 filter which covers 1.558 – 2.315 μm. This filter encompasses the redshifted (z $\sim$ 3.1) [O III] doublet and technically covers redshifted Hβ as well, though we did not see this line. We completed three 500-second integrations, for a total exposure of 25 minutes. The longslit was oriented so that LAB1 regions C15 and C11, as defined by W10, both lie directly on the slit. Region R2 also has some peripheral coverage, though not directly through the location of its peak Lyα emission. Due to the short length of slit we were unable to place an additional continuum-bright object on the slit, so LAB1 was acquired via blind-acquisition from a nearby star.

[O III] detections from C15 and C11 are evident in single, raw 500-second exposures, when a second frame is subtracted from the frame of interest. We find these detections at their expected locations in the spatial direction along the slit, and find they also have the separation from one another that we expect for C11 and C15. In addition, the detections are in the wavelength range expected of each region's Lyα redshift. The dither pattern we used is also clearly visible in positive and negative detections when we perform this sort of quicklook subtraction,

[1] http://www.pa.uky.edu/~peter/atomic/index.html

providing assurance that these detections are not transient cosmic rays in a single exposure. These facts combined give us confidence that the emission we detect is, in fact, from [O III] emission from C15 and C11. See the top panel of Figure 4.1 for these detections in a skysubtracted 2D frame. The [O III] emission from C15 is strong and comes through as such through both our 2D and 1D reduction processes detailed below. The [O III] detections from C11 appear much fainter and are not as evident, though still marginally detected, throughout our 2D and 1D reduction processes.

Initial data reduction of each 500-second exposure was done using NIRSPEC_REDUCE, a set of IDL programs written by G. D. Becker specifically for reduction of NIRSPEC longslit data. We used these scripts for flat fielding and sky subtraction in each exposure. The sky subtraction process in NIRSPEC_REDUCE is based on the algorithm of D. Kelson (Kelson, 2003) which provides excellent sky subtraction of even tilted skylines, such as those in NIRSPEC longslit data. The outcome of these reduction steps are three individual, 2D, flat-fielded, sky-subtracted exposures. We also reduced an argon lamp exposure and a standard star exposure in this same way.

We then fed these exposures into IRAF procedures in the WMKONSPEC package[2]. Each frame was rectified to a horizontal-vertical grid in x- y using the tasks XDISTCOR AND YDISTCOR, which remove x and y distortion in the images, respectively. Once the exposures were rectified, we used IMCOMBINE to median combine the frames into a single exposure. We specified offsets in the IMCOMBINE procedure to remove dithers along the slit that were performed during our observations. The result, what we call our reduced 2D-spectrum, is

[2]http://www2.keck.hawaii.edu/inst/nirspec/wmkonspec.html

shown in Figure 4.1. The locations of our [O III] detections in C11 and C15 are circled.

To extract 1D spectra we used the IRAF DOSLIT procedure. We first defined an aperture trace using a bright standard star observation which can be easily traced along the entire slit. We then transferred this aperture to the correct spatial location in our science exposure to extract spectra of C15 and C11. We used this transferred aperture since neither region has continuum emission that we are able to trace for aperture creation. The spectra were dispersion calibrated with using an argon lamp. The RMS error from dispersion correction was 0.67 and 0.45 Å for C15 and C11 respectively. We used the IRAF WMKONSPEC task SKYINTERP to remove remaining residuals from sky lines. The resultant 1D spectra from C15 and C11 are shown in Figure 4.1.

4.4 LUCIFER data and reduction

We subsequently made additional NIR observations of LAB1 using LUCIFER (LBT NIR Spectrograph Utility with Camera and Integral-Field Unit for Extragalactic Research) on the 8.4m LBT (Seifert et al., 2003; Ageorges et al., 2010). We used the longslit mode of LUCIFER with a 1″ slit utilizing the H+K grating with 200 lines/mm and the N1.8 camera. We completed four 300-second integrations, for a total exposure of 20 minutes. We placed the longslit at a slightly different orientation than our NIRSPEC observations in hopes of capturing more emission from R2 and C15. For the LUCIFER setup, C15 and R2 lay directly on the slit, with part of C11 on the edge of the slit. Given the length of the LUCIFER longslit, we were able to place an object with continuum (an R $\sim$ x galaxy) on the slit as well. This aids in aperture extraction during the reduction process.

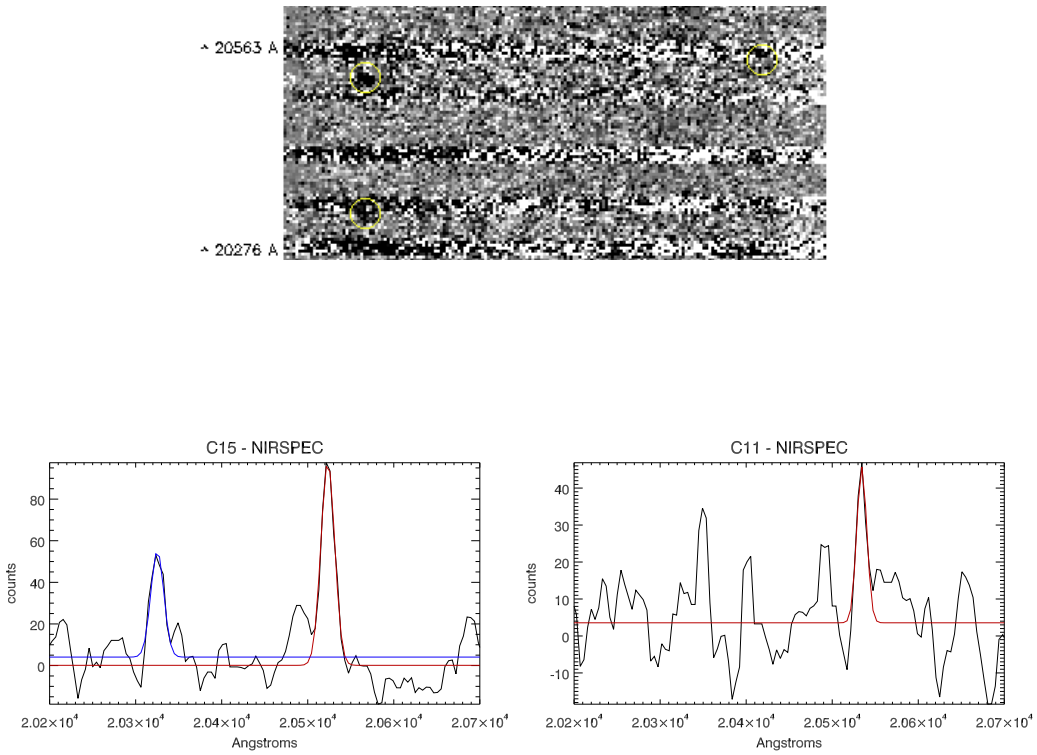

Figure 4.1 Top image is median combined, sky-subtracted, distortion corrected 2D spectrum from NIRSPEC with emission lines from C11 and C15 circled, wavelength increases from bottom to top, [O III] doublet from C15 is at left, 5008.24 Å line from C11 is at right. Bottom row contains 1D NIRSPEC spectra for C15 and C11 with best-fit Gaussians overlaid on emission lines - see Section 4.5.1, blue is 4960.295 Å line and red is 5008.24 Å line.

Figure 4.2 Third NIRSPEC frame subtracted from second NIRSPEC frame, before x-axis and y-axis distortion correction, sky subtraction where [O III] emission (5008.24 Å line) from C11 and C15 are more evident than in 4.1. Emission from C15 in cyan circles, emission from C11 in green circles, emission from second frame is black (positive), emission from third frame is white (negative). Positive-negative dither pattern is clear, showing a detection in both frames displayed here.

We reduced the LUCIFER data in a very similar manner as the NIRSPEC data, but we used a modified version of the NIRSPEC_REDUCE package to accommodate the different detector size and orientation of the LUCIFER data (see McLinden et al. 2012 for more details). After the NIRSPEC_REDUCE procedures, the individual exposures were again median combined with IMCOMBINE and offsets from dithering along the slit were accounted for. Figure 4.4 shows the combined 2D spectrum after this step. LUCIFER 2D spectra do not need x and y distortion correction. For the 1D extraction, we created an aperture trace using the continuum source that shared the slit with our science targets, instead of the standard star as in our NIRSPEC procedure. Then we shifted the aperture to the correct spatial location to extract 1D spectra for C15, C11 and R2. The spectra were again dispersion corrected with an argon lamp exposure. Figure 4.4 shows the 1D extraction of C15 from our LUCIFER data, which was the only region from which we detected [O III] in our LUCIFER observations.

4.5 Results

4.5.1 [O III] redshifts

As we did in McLinden et al. (2011, 2012) we fit detected [O III] lines with single symmetric Gaussian plus constant, using the IDL routine MPFITEXPR[3]. We fit the NIRSPEC and LUCIFER spectra independently. The central wavelength of the best fit Gaussian determines the redshift of the knot. We fit the 4960.295 Å and 5008.24 Å lines independently for C15 in NIRSPEC and we find only the 5008.24 Å line in the LUCIFER data for this knot. Given the redshift of this region from the 5008.24 Å line in LUCIFER, the 4960.295 Å line

[3] http://cow.physics.wisc.edu/ craigm/idl/down/mpfitexpr.pro

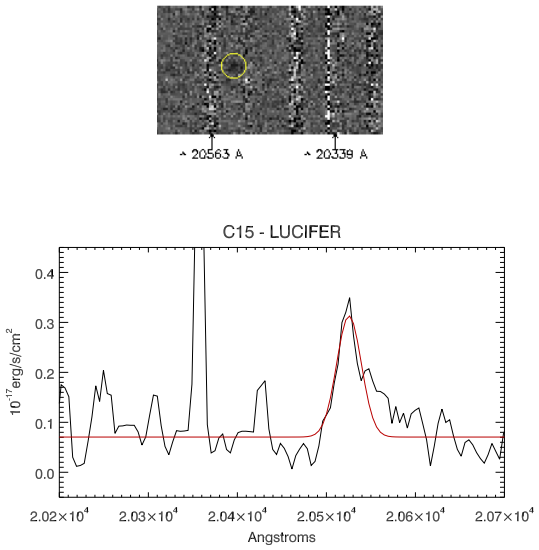

Figure 4.3 Left plot is 2D LUCIFER spectrum centered on C15 with [O III] detections circled, wavelength decreases to the right. Right plot is extracted 1D LUCIFER spectrum of C15 where the feature at ~ 20355 is a bad column. Best-fit Gaussians are overlaid on emission lines - see Section 4.5.1, blue is 4960.295 Å line and red is 5008.24 Å line.

should fall at $\sim$ 20332.25, right on the edge of the 20339.497 Å (vacuum) OH emission line (Rousselot et al., 2000). This may explain why, after sky interpolation we are unable to detect this line in the slightly lower resolution of LUCIFER. The agreement between the redshift derived from 4960.295 and 5008.24 Å lines in NIRSPEC spectrum is excellent (see Table 4.5.3). We take the average of the 4960.295 Å and 5008.24 Å redshift as the derived systemic redshift for C15 from NIRSPEC, and use the redshift of the single line for LUCIFER. These redshifts were corrected for the earth's motion using topocentric radial velocities[4] appropriate for the date and location of the observations. Only the stronger 5008.24 Å line was detected in C11, and only in the NIRSPEC spectrum, so the 5008.24 Å line alone defined the redshift for this region. As mentioned in Section 4.4 the location of longslit in the LUCIFER setup was optimized for detection of R2 and C15, so it is not surprising that we did not have a detection for C11 in the LUCIFER data. The redshift for C11 was again corrected for the Earth's motion, with a final redshift solution of 3.100 ± 0.000362. The error bars on the redshift are a compilation of the RMS for dispersion correction during data reduction, the 1 sigma error on the best-fit central wavelength from Gaussian fitting, averaging of two redshifts when applicable, and a 0.02 km s^{-1} uncertainty on the topocentric radial velocities. See Table 4.5.3 for a summary of this data.

4.5.2 Lyα redshifts

To determine the redshift of the Lyα emission line, we followed the same methodology we previously used in McLinden et al. (2011, 2012). Namely, the Lyα profiles (from W10) for C11 and C15 were fit with a single asymmetric Gaus-

[4] http://fuse.pha.jhu.edu/support/tools/vlsr.html

sian plus constant, using IDL routine ARM_ASYMGAUSSFIT[5]. The asymmetric Gaussian fitting allows for, but does not require, that the fit be asymmetric. We adopted a wavelength uncertainty of 1 Å on the fitted central wavelength to generously account for any error in transcribing the W10 data and to create an error bar on the fitting process from a spectrum without error bars. Once again, the central wavelength of the best-fit Gaussian defines the redshift, and the redshifts were corrected by the appropriate topocentric radial velocity for the date and location of the observations. This is crucial, as it puts our [O III] observations and those of W10 in the same reference frame, so that we might compare the [O III] and Lyα redshifts, which are derived from data taken at different locations on different dates. After correction we find a redshift of 3.093 $\pm$ 0.000823 for C15 and a redshift of 3.100 $\pm$ 0.00823 for C11. The uncertainties on these redshifts is a compilation of the 1 Å uncertainty we adopted in fitting data adopted from W10, and the 0.02 km s^{-1} uncertainty on the topocentric radial velocity correction. See Table 4.5.3 for a summary of this data.

4.5.3 Velocity offsets

We derive a velocity offset (Δv) between the [O III] and Lyα lines by comparing the redshifts for each line as derived from the central wavelength of the best-fit Gaussians to the two lines, where the fitting procedure is described above. This method finds an offset between [O III] and Lyα in C15 of -43.88 $\pm$ 69.01 km s^{-1} from the LUCIFER data and 036.58 $\pm$ 63.85 km s^{-1} from the NIRSPEC data. These results suggest that the velocity offset between these two lines is consistent with zero, i.e. the Lyα line is neither significantly redshifted nor significantly blueshifted when compared to the systemic as defined by [O III]. We find a simi-

[5]http://hubble.as.arizona.edu/idl/arm/arm_asymgaussfit.pro

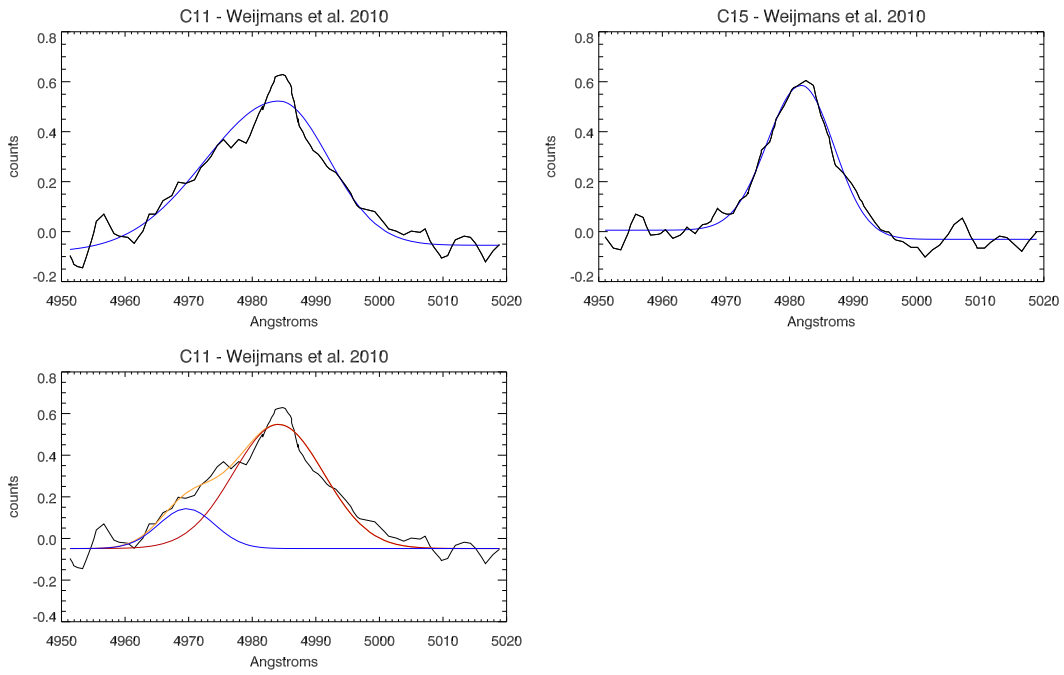

Figure 4.4 Best fit Gaussians for C11 (left panels) and C15 (top right) are shown in blue and observed Lyα spectra from W10 are shown in black. Fits in top panels are from ARM_ASYMGAUSSFIT, bottom panel is C11 fit simultaneously with a double Gaussian using MPFITEXPR - the two Gaussians are shown in blue and red, and their sum is shown in yellow.

lar result when comparing [O III] and Lyα in C11 in the NIRSPEC data, where Δv is 7.31 $\pm$ 69.58 km s^{-1}, or is again consistent with no offset. See Table 4.5.3 for a compilation of these results.

One may argue that the very broad Lyα line in C11 may be better fit with a double Gaussian profile, especially if one considers that the bump to the left of the highest peak is not noise, but in fact evidence of a second, unresolved peak. This could be a blue bump that is not fully resolved and separated from the main red peak. Or it could be the smaller red peak at v=0, as in Fig. 12 in V06. To consider these possibilities, we fit C11 a second time, simultaneously fitting two Gaussians plus a constant (see bottom panel of Figure 4.5.2). When we do this we find that the right peak yields only a modest offset, where the Lyα line is offset by 142 $\pm$ 64 km s^{-1}(NIRSPEC) and 69 $\pm$ 61 km s^{-1} (LUCIFER). (In this double Gaussian fit, the bluer Lyα peak is blueshifted with respect to [O III] by -728 $\pm$ 64 km s^{-1} (NIRSPEC) and -800 $\pm$ 61 km s^{-1} (LUCIFER). This seems a rather inexplicably large offset between the two Lyα peaks, $\sim$ 870 km s^{-1}, especially when the red peak is so mildly offset, which may disfavor this secondary interpretation of the modest bump as a blue bump.

While acknowledgement of the additional fit described above is worthwhile, the discussion stays much the same, whether we consider the velocity offset between [O III] (systemic) and Lyα to be consistent with zero or to be modest, of order 150 km s^{-1} - does this rule out outflows/superwinds as a major source of luminosity in blobs, or is there a model which remains consistent with our observations that can still indicate that outflows may be present?

	LUCIFER [O III]				NIRSPEC [O III]				Weijmans10 Lyα			
	4960.295	5008.24	z_{avg}	z_{corr}	4960.295	5008.24	z_{avg}	z_{corr}	z	z_{corr}	v_{luci} (km s^{-1})	v_{nir} (km s^{-1})
C15		3.0983		**3.0986 ± 0.0003494**	3.0976	3.0979	3.0978	**3.0975 ± 0.0002202**	3.0980	**3.0980 ± 0.0008226**	-43.88 ± 69.01	36.58 ± 63.85
C11						3.0999		**3.0999 ± 0.0003617**	3.1000	**3.1000 ± 0.0008226**		7.31 ± 69.58

Table 4.1 Comparison of [O III] and Lyα redshifts in C11 and C15 as measured with LUCIFER and NIRSPEC. z_{avg} is listed when the redshifts from 4960.295 and 5008.24 Å lines were averaged, z_{corr} is the redshift after correction for the earth's motion. Lyα redshifts are derived from profiles presented in Weijmans (2010) and v_{luci} and v_{nir} are the velocity offsets between [O III] and Lyα from LUCIFER and NIRSPEC data, respectively.

4.5.4 [O III] flux in C15 and R2

We were able to flux calibrate our LUCIFER spectra using a magnitude 6.16 (V band) A5V star that was observed in the same setup as our science observations. We scaled down a Pickles model A5V stellar spectrum (Pickles, 1998) to match the magnitude of the observed star. We created a sensitivity function with units of erg cm^{-2} Å^{-1} counts^{-1} by dividing the model spectrum by the observed stellar spectrum and multiplying by the length of the observation. This sensitivity function is then multiplied by the extracted spectra for C15 and R2 from LUCIFER, the result is divided by the integration time for each object to produce flux calibrated spectra in units of erg s^{-1} cm^{-}2 Å^{-1}. As previously described in Section 4.5.1, the [O III] line in C15 is fit with a symmetric Gaussian plus a constant. The resulting area under the Gaussian gives us a line flux measurement for C15 of 8.44 $\pm$ 1.04 $\times$ 10^{-17} erg s^{-1} cm^{-2}. We derive upper limits for [O II] and Hβ in C15 of 1.3 $\times$ 10^{-17} and 2.2 $\times$ 10^{-16} erg s^{-1} cm^{-2}. Since we do not detect an [O III] line in R2 we instead measure an [O III] line flux upper limit of 3.35 $\pm$ 1.12 $\times$ 10^{-17} erg s^{-1} cm^{-2}.

To compute the 3σ line flux upper limit for R2 quoted above, we added a mock Gaussian emission line to the spectra to represent [O III], similar to the procedure in Finkelstein et al. (2011b); McLinden et al. (2012). The sigma of the Gaussian was fixed to 5.52 Å, or the σ from our faintest [O III] detection to date (McLinden et al., 2011). The area under the mock line was measured using a symmetric Gaussian, this area determines the line flux of the mock line. Then we determined the noise on the line flux measurement from 1000 Monte Carlo iterations, where the flux array was modified each time by a random amount proportional to the error bars (using RANDOMN in IDL). We repeated this process,

each time decreasing the area under the mock Gaussian until the signal to noise ratio (SNR) dropped below 5σ. The line flux in the mock line where the SNR crossed below 5σ determines σ. However, because one cannot know, without an nebular emission line measurement for reference, exactly how much, if any the Lyα line is offset from the [O III] line, we repeat this calculation, fixing the mock line at different redshifts to mimic different velocity offsets. We found the 3σ line flux detection limit as an average of this technique from 6 different redshifts corresponding to velocity offsets of 0-500 km s^{-1}, in increments of 100 km s^{-1}. We adopted the average 1σ detection limit as the error bar on the upper limit of line flux from R2. A range of 0 - 500 km s^{-1} was chosen to mirror the magnitude of Lyα - [O III] velocity offsets we have observed of 52 - 342 km s^{-1} in three z $\sim$ 3.1 LAEs. The range of 3σ detection limits over this wavelength range was 3.12 - 3.54 $\times$ 10^{-17}. The [O II] and Hβ upper limits for C15 are found using the same procedure, except the upper limits are derived at a single fixed wavelength for each line, a wavelength defined from the [O III] redshift.

Given an [O III] line flux detection in C15 and an upper limit in R2, we can compare the nebular emission from these two subregions. This is of interest because C15 is associated with an LBG embedded within the larger LAB1 halo structure, whereas R2, in spite of its stronger Lyα emission , is not associated with any underlying galaxy (Weijmans, 2010). The ratio of Lyα luminosities C15 to R2 is 0.74 (Weijmans, 2010), or R2 is 1.4 times brighter than C15 in Lyα. We find that the ratio of [O III] in C15 to R2 is $\geq 2.5 \pm 0.9$, meaning that while R2 is brighter in Lyα C15 is brighter when looking at [O III] nebular emission. In other words, the [O III] to Lyα ratio measured in the region without an LBG is at least 3.4 times smaller than the same ratio measured in the LBG. This measurement would likely indicate that something other than star formation is powering the Lyα emission

in region R2 and that there may very well be different sources powering Lyα emission in different regions of the same blob.

Additionally, the combination of a measured [O III] line flux and upper limits on [O II], and Hβ line flux in C15 allow us to put contstraints on the metallicity of the LBG embedded in C15 using R_{23}, where R_{23} is defined as $\frac{[O\,II]+[O\,III]}{H\beta}$(Pagel et al., 1979; Kewley & Dopita, 2002). For C15, $R_{23} > 0.76$ given the line flux measurements and limits described above. From the recent work of Richardson et al. (2012), exploring R23 in the high ionization parameter regime, we can then place constraints on the metallicity (Z) and ionization parameter (q) of this LBG. The $R_{23} >$ lower limit of 0.76 for C15 indicates that the metallicity of this object is $0.2Z_\odot \lesssim Z \lesssim 0.4Z_\odot$, with $q > 4 \times 10^8$ cm s^{-1} for a continuous star formation model of a 6 Myr population. For an instantaneous star formation model with a 0 or 1 Myr population the constraints are $0.2Z_\odot \lesssim Z \lesssim 0.4Z_\odot$with $q > 4 \times 10^8$ cm s^{-1}. $Z = 1Z_\odot$ with $q > 9\times 10^8$ cm s^{-1} is also an allowed solution for the two instantaneous cases. An instantaneous star formation model with a 3 Myr population is disfavored. If this LBG plays a crucial role in illuminating at least a portion of LAB1, these fairly consistent results indicate this LBG is a low-metallicity object ($0.2Z_\odot \leq Z \leq 0.4Z_\odot$) with a high characteristic ionization parameter.

4.5.5 Asymmetry and [O III] - Lyα Offset

We have now measured the velocity offset between [O III] and Lyα in five Lyα emitting objects at $z \sim 3.1$. Amongst these objects, the regions C11 and C15 of LAB1 are the first measurements of this offset that have been consistent with zero. This is in contrast to three $z \sim 3.1$ LAEs in which we found offsets ranging from 52 – 342 km s^{-1}. Given this information, we can compare another

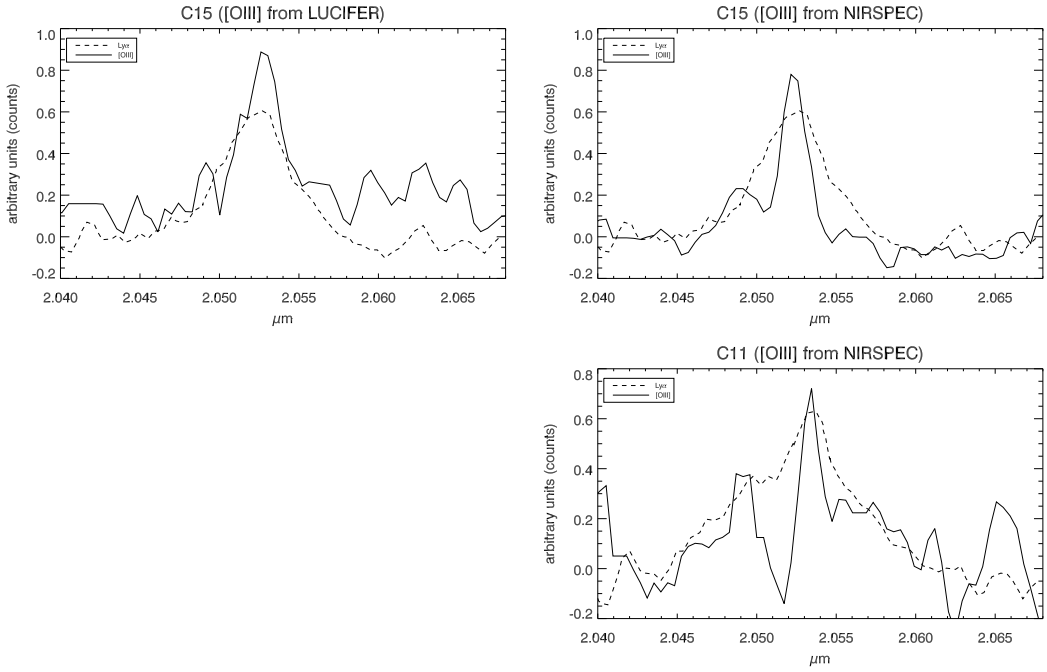

Figure 4.5 Plot of Lyα (dashed line) over [O III] (solid line) where Lyα has been shifted to [O III] frame via Ly$\alpha_{[\mathrm{O\,III}]}$. Top panel is C15, left plot shows [O III] from LUCIFER, right plot shows [O III] from NIRSPEC. Bottom panel is C11 from NIRSPEC.

signature of outflows, namely asymmetry in the Lyα profile, with the velocity offset measurements. We quantify asymmetry as $\sigma_{red}/\sigma_{blue}$ where σ_{red} is the sigma of the red side of the best-fit asymmetric Gaussian and σ_{blue} is the sigma on the blue side of the best-fit asymmetric Gaussian, where both are parameters returned by the ARM_ASYMGAUSSFIT routine. With this definition, a profile with asymmetry > 1.0 is considered asymmetric, and the asymmetry is dominated by the red-wing. Objects with asymmetry $= 1.0$ are symmetric, ≤ 1 have blue-wing dominated asymmetry. The red-wing dominated asymmetry is the expected direction of the asymmetry in the Lyα line from high-z galaxies, as the red side of the line can be enhanced in the presence of an expanding shell (Verhamme et al., 2006; Dijkstra & Wyithe, 2010) and/or by interaction with neutral Hydrogen in the IGM (Rhoads et al., 2003; Dawson et al., 2004). Measured in this way C11 has an asymmetry of ~ 0.67 and C15 has an asymmetry of ~ 0.97. In three z$\sim$ 3.1 LAEs in which we have measured a velocity offset between [O III] and Lyα we find asymmetries of 0.97 ± 0.1, 1.04 ± 0.1, and 1.65 ± 0.1 for LAE7745, LAE27878 and LAE40844, respectively. We add four additional asymmetry data points by using four z $\sim$ 2 LAEs from Hashimoto et al. (2012). Hashimoto et al. (2012) measured redshifted Lyα lines in these objects with respect to Hα lines in the same objects. They report velocity offsets of 18 – 190 km s^{-1} in their four LAEs, in good agreement with our range of 52 – 342 km s^{-1} in LAEs. We measured the asymmetry of the Lyα lines presented by Hashimoto et al. (2012) in the same manner as above, by fitting each line with asymmetric Gaussian and quantifying asymmetry as $\sigma_{red}/\sigma_{blue}$. Measured in this way the LAEs from Hashimoto et al. (2012) have asymmetries of 0.53 - 1.7. Figure 4.6 demonstrates there is a trend where asymmetry in the Lyα profile increases with increasing velocity offset. We find a moderate Pearson linear correlation coefficient of 0.430 (P=0.126)

between the velocity and asymmetry values, suggesting this trend is, in fact, real. This velocity-asymmetry correlation not an unexpected, as increasing (red-wing dominated) asymmetry in the Lyα profile is tied to increasing shell expansion velocities in Verhamme et al. (2006), when outflows are modeled with a central monochromatic source and an expanding shell. A symmetric line, as seen in C11 and C15 is not expected in models with large outflows, but could be consistent with static/nearly-static profiles - if the two symmetric peaks produced from a static slab or shell scenario (Verhamme et al., 2006) are unresolved in the C11 and C15 profiles.

4.6 Discussion

4.6.1 Discussion of Yang et al. (2011) Results

We have measured Δv between [O III] and Lyα in two subregions of LAB1 and found that Δv is consistent with 0 km s^{-1} in one subregion and consistent with 0 km s^{-1}and/or at most very small (142 km s^{-1}) in the second subregion. Interestingly, this measurement of $\Delta v \sim 0$ km s^{-1} is not the first time this phenomena has been reported in a Lyα blob, suggesting this is an important phenomena that must be understood to better understand the nature of high-z LABs. Yang et al. (2011) investigated two z $\sim$ 2.3 LABs, where one blob had $\Delta v \sim 230$ km s^{-1} and the other blob had Δv consistent with zero. The velocity offsets reported in Yang et al. (2011) were measured by comparing the redshift of Hα to that of Lyα, a very similar tactic to our comparison of [O III] to Lyα, as both [O III] and Hα are nebular emission lines and therefore probe the same regions.

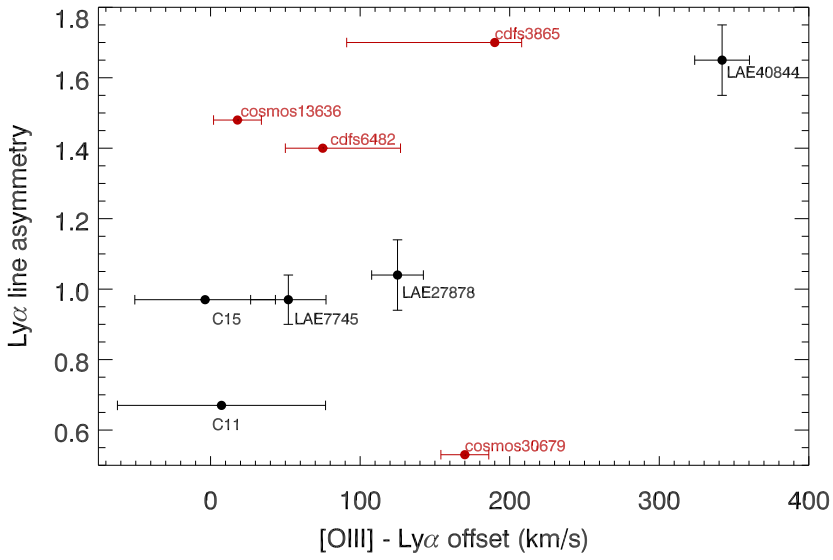

Figure 4.6 Asymmetry of the Lyα profile as a function of velocity offset in five Lyα-emitting objects at z $\sim$ 3.1 C15 and C11 are labeled at v = 0 in black, where the data point for C15 is the average of the NIRSPEC and LUCIFER results, three LAEs (in black) from McLinden et al. (2011, 2012) are labeled with the prefix 'LAE,' red points with the prefix 'cosmos' or 'cdfs' are four LAEs from Hashimoto et al. (2012). Overall, asymmetry increases with increasing velocity offset.

4.6.2 Comparison to LAEs and LBGs

Our Δv measurements, and those of Yang et al. (2011) , are significantly less than the larger velocity offsets typically seen in Lyman break galaxies (LBGs) and even Lyα emitting galaxies (LAEs), velocity offsets which are typically interpreted as clear signatures of strong winds in these galaxies. Steidel et al. (2010) report median velocity offsets between Hα and Lyα of 445 km s^{-1} in 89 z $\sim$ 2.3 LBGs. And even LAEs, whose typical velocity offsets have been found to be smaller, have Δv as large as 342 km s^{-1}(McLinden et al., 2011).

Steidel et al. (2010) also report a median velocity offset between Hα and strong interstellar absorption lines of -164 km s^{-1} in the same 89 LBGs mentioned above, which further supports interpretations of the presence of outflows in LBGs, since the blue-shifted absorption implies absorption in material moving towards the observer. Shapley et al. (2006) previously measured a redshift from low-ionization interstellar absorption (LIS) lines in the LBG C11, finding that the absorption lines are offset from the Lyα line by -380 km s^{-1}. Using the LIS redshift of 3.0962 from Shapley et al. (2006) and comparing this to the Lyα redshift we derive from Weijmans (2010) yields an offset of $\sim$ 278 km s^{-1}. Comparing our [O III] (systemic) redshift for C11 (3.0999) to the LIS redshift, we can estimate that the LIS lines in C11 are offset from [O III] by $\sim$ -270 km s^{-1}. This comparison of Lyα and [O III] redshifts to LIS absorption redshifts provides a stronger signature of an outflow than we get when comparing Lyα and [O III]. In fact, it that is particularly interesting that the magnitude of this second signature of winds (i.e. blueshifted interstellar absorption lines) is so similar when comparing the Steidel LBGs to C11, yet the magnitude of the offset between nebular emission lines (Hα or [O III]) and Lyα offset are so different. We note that the lack of

Δv between [O III] and Lyα does not have to rule out some outflows in LAB1. Rather, the lack of a Lyα-[O III] offset may just imply that outflows are not a significant mechanism for helping Lyα photons escape.

4.6.3 Previous Studies of LAB1

This phenomena, i.e. $\Delta v = \text{small and/or} = 0$ km s^{-1}, leads to the question of whether the lack of substantial velocity offset between Hα-Lyα or [O III]-Lyα in these blobs in fact rules out outflows or if there is some, yet to be understood phenomena, that damps or erases this particular wind signature. This question is particularly relevant given the recent report from Hayes et al. (2011) that there is polarized radiation emanating from LAB1, polarization that is indicative of scattering of Lyα photons at large radii with respect to their site of production. This may be a sign of outflows helping to drive the Lyα photons to these large radii, but we are not seeing the velocity offsets between nebular emission lines and Lyα that we would expect to see if this was the case, velocity offsets we have been able to see in other objects at similar redshifts believed to have strong winds. In addition, Bower et al. (2004) and Weijmans (2010) both measure a velocity shear in the Lyα emission from C11 and C15. As the authors point out, such a velocity shear could be consistent with infalling gas, outflowing gas and/or rotation of the system, and such scenarios cannot be differentiated from the Lyα data alone. While both papers use this velocity shear to argue in favor of the presence of outflows in C11 and C15, we can report no signature of such outflows when we compare the redshifts of [O III] and Lyα, a comparison that has proven to be a useful diagnostic of winds in LAEs and LBGs at similar redshifts.

4.6.4 Comparison to Radiative Transfer Models

We explored available Lyα radiative transfer models to see if there were any models that might shed light on the physical conditions that could lead to a Δv of ~ 0 km s^{-1} between [O III] (or Hα) and Lyα and match the single peaked Lyα profiles for C11 and C15, as presented by W10. In particular, we focused on the Lyα profiles produced by Verhamme et al. (2006) (henceforth V06) from their 3D Monte Carlo Lyα radiative transfer code. V06 explore a variety of physical conditions and geometric orientations to explore the variety of Lyα profiles that arise from different environments. See V06 for extensive details on these models and the model parameters. We find, however, that none of the models presented in V06 are in good agreement with our observations (or those of Yang et al. (2011)). The only models that are marginally consistent with our observations are those that have two significant Lyα peaks, where the centroid of those two peaks is at least centered at v ~ 0, and one peak is redward of v$= 0$, and the other blueward. This double -peaked, centered at v ~ 0 profile occurs when a central monochromatic source is embedded in a static slab (with or without dust, V06 Figure 3), a central monochromatic source sits in a non-expanding shell (V06 Figure 14), and when a single monochromatic source sits in an expanding shell with very small velocity gradient (Vmax $= 20$ km s^{-1}, V06 Figure 7). Even after we transform such V06 models to wavelength space to match the Lyα observations, and smooth the models to approximately match the resolution of the SAURON data (4.9 Åpixel^{-1}), the double peaked profiles remain, showing that event though the models are centered at v $= 0$ (consistent with the W10 Lyα profiles), we are unable to recover the single broad Lyα peak W10 observed (see Figure 4.6.4). In addition, there are a variety of V06 models that produce a single-peaked Lyα pro-

files (or profiles with one main peak much larger than any secondary peaks), but those profiles are either significantly redshifted (expanding shell) or blueshifted (collapsing shell) with respect to $v = 0$, both of which are inconsistent with our observation that Lyα is neither redshifted or blueshifted with respect to $v = 0$. In addition, in either scenario (expanding or infalling shell) the main peak is expected to be asymmetric, which is again inconsistent with the W10 Lyα profiles of C11 and C15. We contend that more modeling of Lyα radiative transfer with direct applications to the observations we have presented here and those observations presented in Yang et al. (2011) needs to be done, to better understand the physical conditions, geometry, and kinematics that can produce single peaked Lyα lines, with $\Delta v = 0$.

It seems a strong possibility that the Lyα profiles for C11 and C15, from W10, may in fact be a convolution of multiple Lyα profiles. This would help to explain the broadness of the profile, and even go some ways towards explaining the lack of asymmetry seen in both profiles. Some of the Lyα photons may be from the LBGs that are central to these two regions, while some of the Lyα photons may be from the surrounding gas/halos. With the possibility that multiple regions are being represented within the single Lyα line profile, it is then possible that there are different kinematics at play in these different regions. This may explain why there are no great comparisons to be made between simple expanding (or infalling) shell models and our observations. It may be that if we could separate out the Lyα line from only the LBG in C11 and/or C15, we would in fact see that line redshifted with respect to [O III] line, but then that outflow signature may be muddled by additional scatterings and kinematics at play in the extended halo of the blob. But given the measurements at hand, we do not see an offset between the two lines as expected in the presence of an outflow.

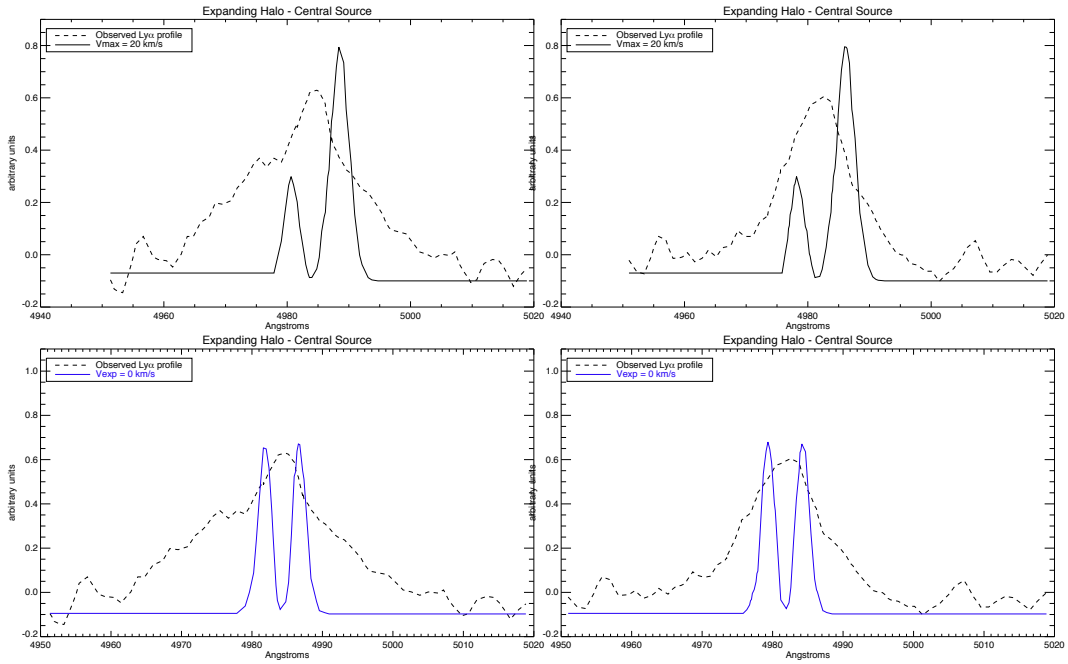

Figure 4.7 Lyα profile (dashed line) from W10 for C11 (left panels) and C15 (right panels). Top panels: smoothed model Lyα profile (solid line) adapted from Figure 7 in V06. Bottom panels: smoothe model Lyα profile (solid line) adapted from Figure 14 in V06. While these models present the closest match to the observed profiles, clearly neither is a good fit.

4.7 Conclusion

We have measured [O III] in two subregions of LAB1, C11 and C15, regions that are associated with underlying LBGs within the larger halo structure. We have quantified the velocity offset between [O III] and Lyα redshifts in these regions, finding that both measurements are consistent with zero, i.e. no velocity offset. This is an intriguing result since powerful outflows have been proposed as possible ways to explain the luminosity and large spatial extent of LABs. We cannot completely rule out the presence of strong winds and outflows in LAB1, but we can state that we do not see two typical markers of their presence. (1) The aforementioned result that we do not find a velocity offset between [O III] and Lyα in the two LAB1 subregions C15 and C11. And (2) we do not measure strong red-wing dominated asymmetries in the Lyα profiles of these objects, in contrast with $z \sim 2$ and $z \sim 3.1$ LAEs where the asymmetry of the Lyα line appears to increase with increasing velocity offset between [O III] (or Hα) and Lyα. If outflows are present in LAB1, they do not appear to be a crucial mechanism driving Lyα escape.

In addition to the conclusion above, we have placed an upper limit on [O III] line flux from region R2, a subregion of LAB1 unassociated with any known galaxy and compared this to the [O III] flux from subregion C15, which is associated with an LBG. We find that in spite of the strong Lyα emission present in R2, the [O III] flux from C15 is stronger than that of R2 by at least 2.5 times. This measurement may indicate that diverse sources of Lyα emission may be responsible for powering different regions even within the same blob.

4.8 Acknowledgements

The LBT is an international collaboration among institutions in the United States, Italy and Germany. LBT Corporation partners are: The University of Arizona on behalf of the Arizona university system; Instituto Nazionale di Astrofisica, Italy; LBT Beteiligungsgesellschaft, Germany, representing the Max-Planck Society, the Astrophysical Institute Potsdam, and Heidelberg University; The Ohio State University, and The Research Corporation, on behalf of The University of Notre Dame, University of Minnesota and University of Virginia.

This work was supported by a NASA Keck PI Data Award (award number is 1408709), administered by the NASA Exoplanet Science Institute. Data presented herein were obtained at the W. M. Keck Observatory from telescope time allocated to the National Aeronautics and Space Administration through the agency's scientific partnership with the California Institute of Technology and the University of California. The Observatory was made possible by the generous financial support of the W. M. Keck Foundation. The authors wish to recognize and acknowledge the very significant cultural role and reverence that the summit of Mauna Kea has always had within the indigenous Hawaiian community. We are most fortunate to have the opportunity to conduct observations from this mountain.

NSF grant AST-0808165 also provided funding for this work, thanks to Mark Richardson for various helpful conversations.

Chapter 5

CONCLUSION

We have explored and characterized Lyα emitting objects in the z $\sim$ 3.1 universe. We have presented three related observational studies and analyses of Lyman-alpha emitting galaxies and Lyman-alpha blobs, with the goal of providing the most comprehensive picture of these objects to date. We have sought to further understanding of LAEs and LABs by studying the gas kinematics and how this effects the detectability of Lyα emission. Additionally we aimed to provide a simple but powerful improvement to how the stellar populations of LAEs are modeled. Together, these goals allow us to investigate the physical processes occurring in these objects in the early universe.

In the initial study in Chapter 2, we presented the first detections of [O III] emission from Lyα-selected field galaxies. These first [O III] detections opened a new avenue for study of high-redshift Lyα emitting objects, an avenue that we further explored in Chapters 3 and 4. The goal in Chapter 2 was to compare the redshifts measured from the [O III] line in these two objects, with the redshifts measured from Lyα in these same two objects. Comparison of these two redshifts can provide evidence of the presence or absence of outflows in these systems. This comparison works because [O III] is a nebular emission line that is not subject to deformation and/or interaction with other materials during its journey from the source to us. As such, [O III] retains information on the actual systemic redshift of the source. Lyα on the other hand, is subject to resonant scattering and complex radiative transfer effects, so the profile and redshift of the Lyα line,

when compared to the undisturbed [O III] line, contains information about any outflows it encountered.

In both LAEs in Chapter 2 we measured a velocity offset between the redshifts of Lyα and [O III]. These velocity offsets ranged from 125 – 342 km s^{-1}. We find that these velocity offsets and the features of the Lyα line profile both indicate that our measurements were a result of Lyα emission emerging in the presence of a galactic outflow. We acknowledge that with a sample of only two galaxies to start with, we can not yet characterize the expected range of velocity offsets in LAEs, or make statements about a characteristic value of this offset for LAEs in general, but we have demonstrated the efficacy of a new method for measuring this wind signature and as more measurements are made, a clearer picture will emerge.

In Chapter 3 we presented the observation and analysis of one new [O III] detection in a z $\sim$ 3.1 LAE. This additional data point was still consistent with our interpretation that outflows are present and are important features of LAEs. The additional measurement also broadened our range of velocity offsets to 52 – 342 km s^{-1}, a range that we plan to add many data points to in coming years as we continue observing LAEs in the NIR.

Aside from the additional [O III] detection, the main focus of Chapter 3 was really to improve SED fitting of LAEs. The quality of SED fitting has suffered in the past because nebular emission lines were not always accounted for, and most analyses were done by stacking individual LAEs and deriving a single average for each physical characteristic. We have put forth improvements on both of these counts, by individually fitting 33 LAEs and by developing a new and simple way to account for nebular emission in the fitting process. Our sample of 33 LAEs is one of the largest sample of individually fit LAEs to date and we argue that

careful fitting of individual LAEs provides a more accurate look at the physical characteristics, and diversity of physical characteristics, of these LAEs.

From these fits we find constraints on age, mass, dust content, metallicity, star formation history, and [O III] line flux. We find that while our sample has quite diverse characteristics, some generalizations can be made. Namely, a majority of the galaxies are fit with a single instantaneous burst or exponentially decreasing star formation history and the sample as a whole has only moderate amounts of dust, and sub-solar metallicity. Median values for ages and masses are 450 Myrs and 1.5×10^9 $M_\odot$ are found. Finally, most of the galaxies are best fit with an [O III] line contributing additional flux to the K_s band, with an average flux of 2.8×10^{-17} erg s^{-1} cm^{-2}. One of the strengths of our new SED fitting approach is that the [O III] line flux predictions from our models can be compared to the actual [O III] detections (and nondetections) we have from our NIR observations of LAEs. We find that overall our predictions and observations are in good agreement, providing proof that our new approach is useful. Physical characteristics, as derived from SED fitting, together with velocity offset measurements presented in Chapters 2 and 3, provide a comprehensive view of the physical characteristics and processes occurring in LAEs at $z \sim 3.1$. The measurements presented here can be compared to work previously done at other redshifts and work that will be improved at other redshifts, to track the evolution of these characteristics across various epochs.

Chapter 4 illustrated how we transferred our methodology - searching for nebular emission lines for comparison with Lyα profiles - to a Lyman-alpha blob at $z \sim 3.1$. This chapter presents the first measurements of [O III] in the LAB. In contrast to the findings presented in Chapters 2 and 3, we found no evidence for a velocity offset between the redshifts of [O III] and Lyα in two subregions

of the object. This is somewhat surprising, as powerful outflows have been proposed as one of the leading possible power sources for the intense Lyα emission from LABs. It is also interesting in that Lyα emission is often considered a marker of intense star formation, and one often expects outflows to accompany intense star-formation. This result also prompts an interesting discussion about whether a lack of velocity offset can truly rule out the presence of winds and intense star formation in blobs. Or perhaps the emergent Lyα profile we have for comparison is a convolution of multiple processes occurring in the blob and thereby smearing out the usual signature of an offset that we can use to identify outflows. While we have been able to present new and interesting results regarding this object, I contend that additional Lyα measurements are needed to clarify the picture. We need carefully and narrowly targeted Lyα observations of smaller regions of the blob for comparison with our [O III] lines. This should help decipher whether winds are truly absent, or whether the signal is simply not apparent in the currently available Lyα data. If outflows are indeed not detected in this LAB, that could help effectively rule out one of the main proposed power sources for LABs.

Taken together, our studies have shown that so far, winds appear to be ubiquitous in LAEs - as each [O III] detection in an LAE has yielded a measurable velocity offset from Lyα. On the other hand, winds are thus far undetected in LABs when we use the same methodology. This is an interesting result in that two objects identified by the same emission at the same redshift have different signatures with regard to outflows. This result is also somewhat confounding since outflows seem to play a crucial role in boosting the detectability of Lyα from LAEs - how then is it possible that one sees such powerful and extended Lyα emission from LABs if outflows are not present and/or crucial in these objects? I think answering this question will come from a two-pronged approach. Namely,

(1) outflows may be present in LABs, but the current Lyα data available muddles the outflow signature. If this is the case, more narrowly targeted slit spectroscopy will uncover this signature. Or (2) collaborations I plan to undertake with Lyα radiative transfer modelers will shed light on the geometry and kinematics that could make $\Delta v \sim 0$ between the Lyα and [O III] lines possible.

In addition to measuring the kinematics of gas in these objects with [O III], we have used our [O III] measurements in an attempt to better model the physical characteristics of LAEs. Together with the outflow information, we have created a comprehensive picture of these objects and laid the foundation for future study of more LAEs with these methods. In particular, my work has shown that a simplified approach to handling nebular emission lines in SED fitting is possible and successfully reproduces observed data.

I look forward to continuing similar investigations as a postdoc, where I will have access to an expected $\sim 10^6$ LAEs at $z \sim 2$ from the HETDEX project over the next three years. HETDEX will provide an unprecedentedly large sample with which to study the kinematics of LAEs. This should provide an even more comprehensive view of the role of outflows in these objects and a real understanding of the overall distribution of velocity offsets seen in LAEs.

BIBLIOGRAPHY

Acauaviva, V., Vargas, C., Gawiser, E., Guaita, L. 2012, ApJL, 751, 26

Adelberger, K. L., Steidel, C. C.,Pettini, M., Shapley, A. E., Reddy, N. A. & Erb, D. K. 2005, ApJ, 619, 697

Ageorges, N. et al. 2010, "LUCIFER1 commissioning at the LBT", SPIE Proc. Vol. 7735-56

Ahn, S-H., Lee, H-W. & Lee H. M. 2003, MNRAS, 340, 863

Becker, G. D., Sargent, W. L. W., Rauch, M. & Simcoe, R. A. 2006, ApJ, 640, 69

Bertin, E. & Arnouts, S. 1996, A&AS, 117, 393

Bianchi, S. & Ferrara, A. 2005, MNRAS, 358, 379

Bond, N. A., Gawiser, E., Gronwall, C., Ciardullo, R., Altmann, M. & Schawinski, K. 2009, ApJ, 705, 639

Bond, N. A., Feldmeier, J. J., Matkovich, A., Gronwall, C., Ciardullo, R., & Gawiser, E. 2010, ApJ, accepted

Boulade, O., et al. 2003, Proc. SPIE, 4841, 72

Bower R. G. et al., 2004, MNRAS, 351, 63

Bremer, M. N. & Johnstone, R. M. 1995, MNRAS, 277, L51

Bruzual, G. & Charlot, S. 2003, MNRAS, 344, 1000B

Capak, P. et al. 2007, ApJS, 172, 99

Cassata, P. et al. 2010, submitted to A&A

Chapman S. C., Lewis G. F., Scott D., et al. 2001, 548, 17

Chapman S. C., Scott D., Windhorst R. A., et al. 2004, ApJ, 606, 85

Ciardullo, R., Gronwall, C., Wolf, C., McCathran, E., Bond, N. A., et al. 2012, ApJ, 744, 110

Cowie, L. L., & Hu, E. M. 1998, AJ, 115, 1319

Cowie, L., Barger, A. J. & Hu, E. M. 2010, ApJ, 711, 928

Cowie, L., Barger, A. J. & Hu, E. M. 2011, ApJ, 738, 136

Dawson, S., Spinrad, H., Stern, D., Dey, A., van Breugel, W., de Bries, W. & Reuland, M., 2002, ApJ, 570, 92

Dawson, S., Rhoads, J. E., Malhotra, S., Stern, D., Dey, A., Spinrad, H., Jannuzi, B. T., Wang, J. X. & Landes, E. 2004, ApJ, 617, 707

Dayal, P., Maselli, A. & Ferrara A. 2010 submitted to MNRAS

Dey, A., et al. 2005, ApJ, 629, 654

Dijkstra M. & Loeb A., 2009, MNRAS, 400, 110

Dijkstra, M. & Wyithe, J. S. B. 2010 MNRAS, 408, 352

Dow-Hygelund, C. C. et al. 2007, ApJ, 660, 47

Elvis, M., Civano, F., Vignali, C., et al. 2009, ApJS, 184, 158

Eyles, L. P. et al. 2007, MNRAS, 374, 910

Fabricant, D., et al. 2005, PASP, 117, 1411

Fan, X. et al. 2006, AJ, 132, 117

Ferrara, A., Ferrini, F., Barsella, B. & Franco, J. 1991, ApJ, 381, 137

Finkelstein, S. L., Rhoads, J. E., Malhotra, S., Pirzkal, N. & Wang, J. X. 2007, ApJ, 660, 1023

Finkelstein, S. L., Rhoads, J. E., Malhotra, S., Grogin, N. & Wang, J. X. 2008, ApJ, 678, 655

Finkelstein, S. L., Rhoads, J. E., Malhotra, S., & Grogin, N. 2009 ApJ, 691, 465

Finkelstein, S. L. et al. 2009, ApJ, 700, 376

Finkelstein, S. L., Hill, G. J., Gebhardt, K., Adams, J., Blanc, G. A., et al. 2011, ApJ, 729, 140

Finkelstein, S. L., Cohen, S. H., Moustakas, J., Malhotra, S., Rhoads, J. E., & Papovich, C. 2011 ApJ, 733, 117

Finlator, K., Oppenheier, B. D., Davé, R. 2011, MNRAS, 410, 1730

Fosbury, R. A. E., et al. 2003, ApJ, 596, 797

Fukugita, M., Yasuda, M., Doi, M., Gunn, J. E. & York, D. G. 2010, submitted to AJ

Garel, T., Blaizot, J., Guiderdoni, B., Schaerer, D., Verhamme, A. & Hayes, M. 2012, MNRAS,

Gawiser, E. et al. 2006, ApJ, 642, L13

Gawiser, E. et al. 2007, ApJ, 671, 278

Geach J. E., et al. 2007, ApJ, 655L, 9

Geach et al., 2009, ApJ, 700, 1

Gronwall, C., Ciardullo, R., Hickey, T., et al. 2007, ApJ, 667, 79

Guaita, L. et al., 2011, ApJ, 733,114

Haiman Z. & Spaans M., Quataert E., 2000, ApJ, 537, 5

Hansen, M. & Oh, S. P. 2006, MNRAS, 367, 979

Hashimoto, T., Ouchi, M., Shimasaku, K., et al. 2012, submitted to ApJ

Hayes, M. et al. 2010, Nature, 464, 562

Hayes, M., Scarlata, C. & Siana, B. 2011, Nature, 476, 304

Heckman, T. M., Armus, L., Miley, G., K. 1990, ApJs, 74, 833

Heckman, T. M., Lehnert, M., D., Strickland, D., K., M., Armus, L. 2000, ApJs, 129, 493

Heckman, T. M., Semback, K., Meurer, G., Leitherer, C., Calzetti, D. & Martin, C. 2001, ApJ, 558, 56

Heckman, T. M. 2002, ASPCS, 254, 292

Holden, B. P., et al. 2001, AJ, 122, 629

Holwerda, B. W. 2005, astro-ph/0512139

Hu, E. M., Cowie, L. L., & McMahon, R. G. 1998, ApJ, 502, L99

Ilbert, O., Capak P., & Salvato, M. et al. 2009, ApJ, 690, 1236

Kaleida, C., & Scowen, P., A. 2010, AJ, 140, 379

Kashikawa, N. et al. 2006, ApJ, 648, 7

Kelson, D. D. 2003, PASP, 115, 688

Kewley, L. J. & Dopita, M. A. 2002, ApJS, 142, 35

Koekemoer, A. M., et al. 2007, ApJS 172, 196

Kornei, K. A., et al. 2010, ApJ, 711, 693

Kunth, D. et al., 1998, A&A, 334, 11

Lai, K., Huang, J-S. & Fazio, G., 2007, ApJ, 665, 704

Lai, K. et al. 2008, ApJ, 674, 70

Le Delliou M., Lacey C. G., Baugh C. M., Morris S. L., 2006, MNRAS, 365, 712

Leauthaud, A., et al. 2007, ApJs, 172, 219

Madau, P. 1995, ApJ, 441, 18

Malhotra, S. et al. 2010 (in prep)

Malhotra, S., Rhoads, J. E., Finkelstein, S. L. et al. 2012, ApJ, 750, 36

Malhotra, S. & Rhoads, J. E. 2004, ApJ, 617, L5

Malhotra, S. & Rhoads, J. E. 2006, ApJ, 647, L95

Maraston, C., Pforr, J., Renzini, A., Daddi, E., Dickinson, M., Cimatti, A. & Tonini, C., 2010, MNRAS, 407, 830

Massey, R., Stoughton, C., Leauthaud, A., Rhodes, J., Koekemoer, A., Ellis, R., Shaghoulian, E., 2010, MNRAS, 401, 371

Matsuda Y., et al. 2004, AJ, 128, 569

McCandliss, S. R. 2009, AIPCS, 1135, 309

McCracken, H. J., Capak, P., Salvato, M., et al. 2010, ApJ, 708, 202

McCracken, J. H., et al. 2012, submitted to A&A, arXiv:1204.6586v1

McDonald, P., Miralda-Escudé, J., Rauch, M., Sargent, W. L. W., Barlow, T. A., Cen, R., & Ostriker, J. P. 2000, ApJ 543, 1

McLean, I. S., Becklin, E. E., Bendiksen, O., et al. SPIE, 1998, 3354, 566

McLinden, E. et al. 2011, ApJ, 730, 136

McLinden et al. 2012, in prep

Miyazaki, S. et al. 2002, PASJ, 54, 833

Nakajima, K. et al. 2012, ApJ, 745, 12

Neufeld, D. A. 1991, ApJ, 370L, 85

Nilsson, K. K.; Fynbo, J. P. U.; Møller, P.; Sommer-Larsen, J.; Ledoux, C. 2006, A&A, 452, L23

Nilsson, K. K. et al. 2007, A&A, 471, 71

Nilsson K. K., Östlin, G., Møller, P., et al. 2011, A&A, 529, 9

Ohyama Y., et al., 2003, ApJ, 591, 9

Ono, Y. et al. 2010, MNRAS, 402, 1580

Ono, Y. et al. 2010, ApJ, 724, 1524

Ouchi, M., et al. 2003, ApJ, 582, 60

Ouchi, M. et al. 2008, ApJS, 176, 301

Pagel, B. E. J., Edmunds, M. G., Blackwell, D. E., et al. 1979, MNRAS, 189, 95

Papovich, C., Dickinson, M., & Ferguson, H. C. 2006, ApJ, 559, 620

Papovich, C. et al. 2006, AJ, 132, 231

Papovich, C., Finkelstein, S. L., Ferguson, H. C., Lotz, J. M., Giavalisco, M. 2011, MNRAS, 412, 1123

Partridge, R. B. & Peebles, P. J. E. 1967, ApJ, 147, 868

Pettini, M., Shapley, A. E., Steidel, C. C., Cuby, J.-G., Dickinson, M., Moorwood, A.F.M., Adelberger, K. L., Giavalisco, M. 2001, ApJ, 554, 981

Pickles, A. J. 1998, PASP, 110, 863

Pirzkal, N., Malhotra, S., Rhoads, J. E. & Xu, C. 2007, ApJ, 667, 49

Prescott, M. K., Smith, P. S., Schmidt, G. D., Arjun, D. 2011, ApJ, 730, 25

Raichoor, A. et al. 2012, ApJ, 745, 130

Reddy, N. A. et al. 2008, ApJS, 175, 48

Rhoads, J. E. 2000, PASP, 112, 703

Rhoads, J. E. & Malhotra, S. 2001, ApJ 563, L5

Rhoads, J. E., Malhotra, S., Dey, A., Stern, D., Spinrad, H. & Jannuzi, B. T. 2000, ApJ, 545, L85

Rhoads, J. E., Dey, A., Malhotra, S., Stern, D., Spinrad, H. & Jannuzi, B. T. Dawson, S., Brown, Michael, J. I., Landes, E. 2003, AJ, 125, 1006

Rhoads, J. E. et al. 2009, ApJ, 697, 942

Richardson, M. L. A., McLinden, E., Malhotra, S. et al. 2012, submitted to MNRAS

Rousselot, P., Lidman, C., Cuby, J. G., Moreels, G., & Monnet, G. 2000, A&A, 354, 1134

Sanders, D. B., et al. 2007, ApJS, 172, 86

Santos, M.,R. 2004, MNRAS, 349, 1137

Schaerer, D. & Verhamme, A. 2008, A&A, 480, 369

Schaerer, D. & de Barros, S. 2009, A&A, 502, 423

Seifert, W., Appenzeller, I., Baumeister, H., et al. 2003, "LUCIFER: a Multi-Mode NIR Instrument for LBT", SPIE Proc. Vol. 4841 Instrument Design and Performance for Optical/Infrared Ground-Based Telescopes

Shapley, A. E., Steidel, C. C., Adelberger, K. L., Dickinson, M., Giavalisco, M. & Pettini, M. 2001, ApJ, 562, 95

Shapley, A. E., Steidel, C. C., Pettini, M. & Adelberger, K. L. 2003, ApJ, 588, 65

Shapley, A. E., Steidel, C. C., Pettini, M., Adelberger, K. L. & Erb, D. K. 2006, ApJ, 651, 688

Shimasaku, K. et al. 2006, PASJ,58, 313

Somerville, R. S. & Primack, J. R. 1999, MNRAS, 310, 1087

Spergel, D. N. et al. 2007, ApJS, 170, 377

Stark, D. P., Ellis, R. S., Chiu, K., et al. 2010, submitted to MNRAS

Steidel, C. C., Adelberger, K. L., Shapley, A. E., et al. 2000, ApJ, 532, 170

Steidel, C. C., Pettini, M., Adelberger, K. L. 2001, ApJ, 546, 665

Steidel, C. C., Erb, D. K., Shapley, A. E., et al. 2010, ApJ, 717, 289

Stern D., Yost, S. A., Eckart, M. E., et al. 2005, ApJ, 619, 12

Taniguchi Y. & Shioya Y., 2000, ApJ, 532, 13

Tapken, C., Appenzeller, I., Noll, S., et al. 2007, å, 467, 63

Tenorio-Tagle, G., Silich, S. A., Kunth, D., et al. 1999, MNRAS, 309, 332

Valdes, F., Guide to the Kitt Peak Coude Slit Reduction Task DOSLIT, Central Computer Services, NOAO, 1993

Venemans, B. P., Röttgering, H. J. A., Miley, G. K., et al. 2005, A&A, 431, 793

Verhamme, A., Schaerer, D. & Maselli, A. 2006, A&A, 460, 397

Verhamme, A., Schaerer, D., Atek, H., & Tapken, C. A&A, 491, 89

Weijmans, A-M., Bower, R. G., Geach, J. E., et al. 2010, MNRAS, 402, 2245

Williams, G. G., Olszewski, E., Lesser, M. & Burge, J. H., et al. 2004, SPIE Proc, 5492, 787

Wright, N., 2006, PASP, 118, 1711

Yang, Y., Zabludoff, A., Jahnke, K., et al. 2011, ApJ, 735, 87

Zheng, Z., Cen, R., Trac, H., Miralda-Escude, J. 2010, submitted to ApJ

Zheng, Z. Y., Wang, J. X., Finkelstein, S. L., Malhotra, S., Rhoads, J. E. & Finkelstein, K. D. 2010, ApJ, 718, 52

de Zeeuw T. et al., 2002, MNRAS, 329, 513

APPENDIX A

NOTES ON CO-AUTHORED WORKS

Chapter 2 was published in The Astrophysical Journal in 2011. I am first author on this paper, the full citation is McLinden et al., 2011, ApJ, 730, 136. I have received permission (via email) from all co-authors to include this publication in my dissertation. The co-authors are Steven L. Finkelstein, James E. Rhoads, Sangeeta Malhotra, Pascale Hibon, Mark L. A. Richardson, Giovanni Cresci, Andreas Quirrenbach, Anna Pasquali, Fuyan Bian, Xiaohui Fan, and Charles E. Woodward.

Chapter 3 is a paper in prep that will be submitted to Monthly Notices of the Royal Astronomical Society. I am first author on this paper, the co-authors are: James Rhoads, Sangeeta Malhotra, Steven Finkelstein, Mark Richardson, Brent Smith, and Vithal Tilvi. The co-authors have given permission for this work to be used in my dissertation. Figures shown in Appendix B are found in Appendix 1 in the paper-in-prep.

Chapter 4 was submitted to The Astrophysical Journal on July 20th, 2012 and is in review. I am first author on this paper, the co-authors are Sangeeta Malhotra, Pascale Hibon, and James Rhoads, and Vithal Tilvi. The co-authors have given permission for this work to be used in my dissertation.

APPENDIX B

ADDITIONAL FIGURES FOR CHAPTER THREE

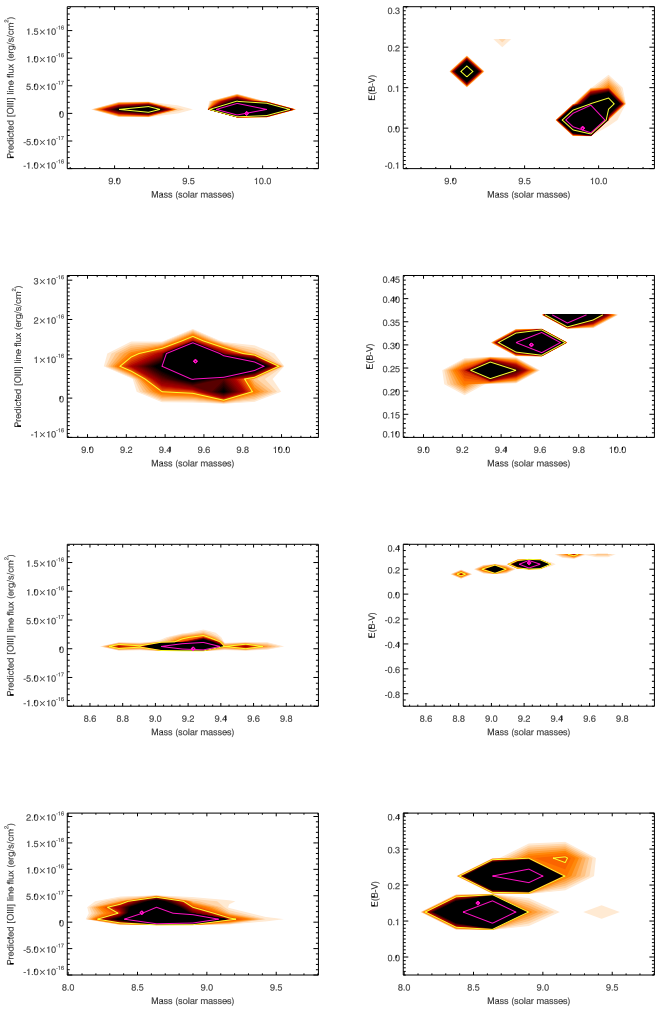

Figure B.1 Density plots from MC simulations for additional parameters - left column is predicted [O III] line flux vs. mass (log), right column is E(B-V) vs. mass (log). The best allowed-fit is shown as a magenta diamond, contours encompassing ∼ 68% and ∼ 95% of the results are shown in magenta and yellow, respectively. The order of objects in Figure B.1 - Figure B.2 matches order of objects in Table 3.2–3.4.

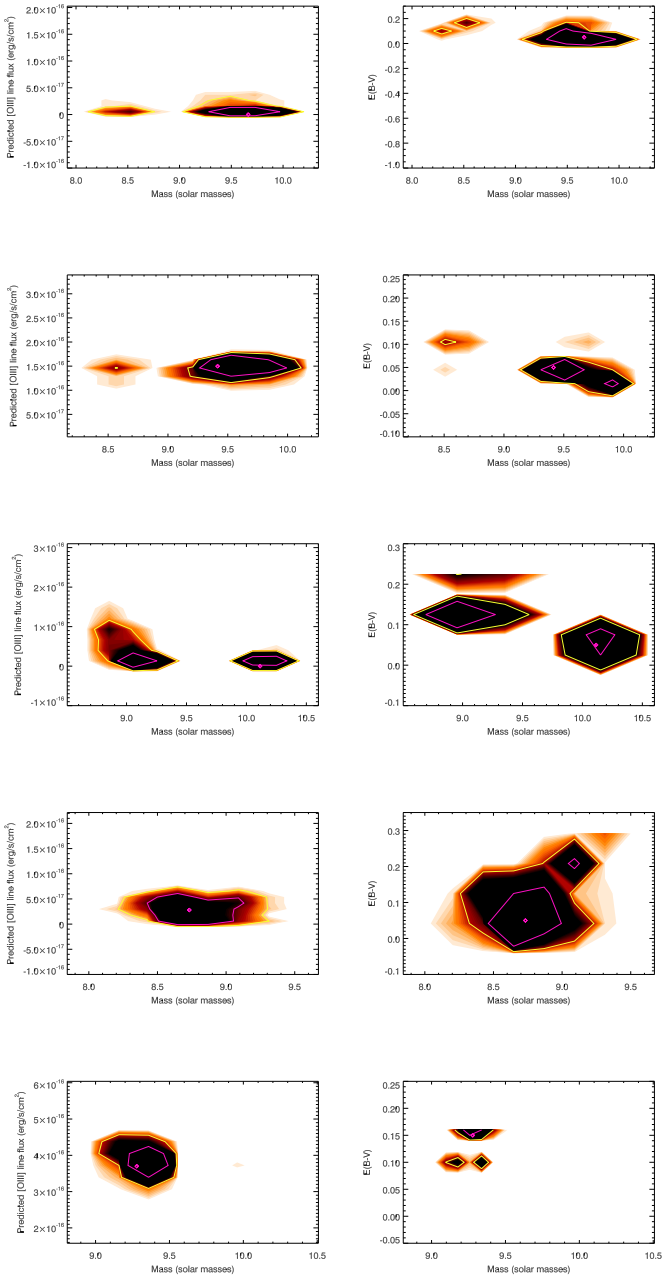

Figure B.2 Same as Figure B.1 for next 5 objects.

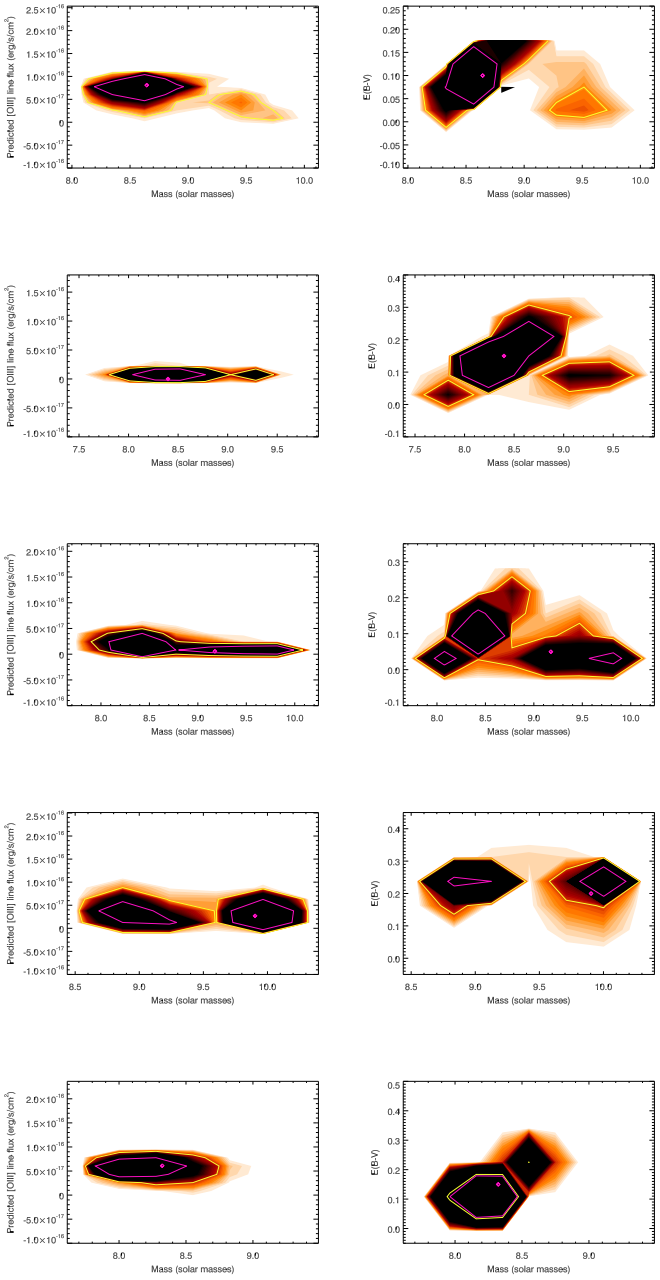

Figure B.3 Same as Figure B.1 for next 5 objects.

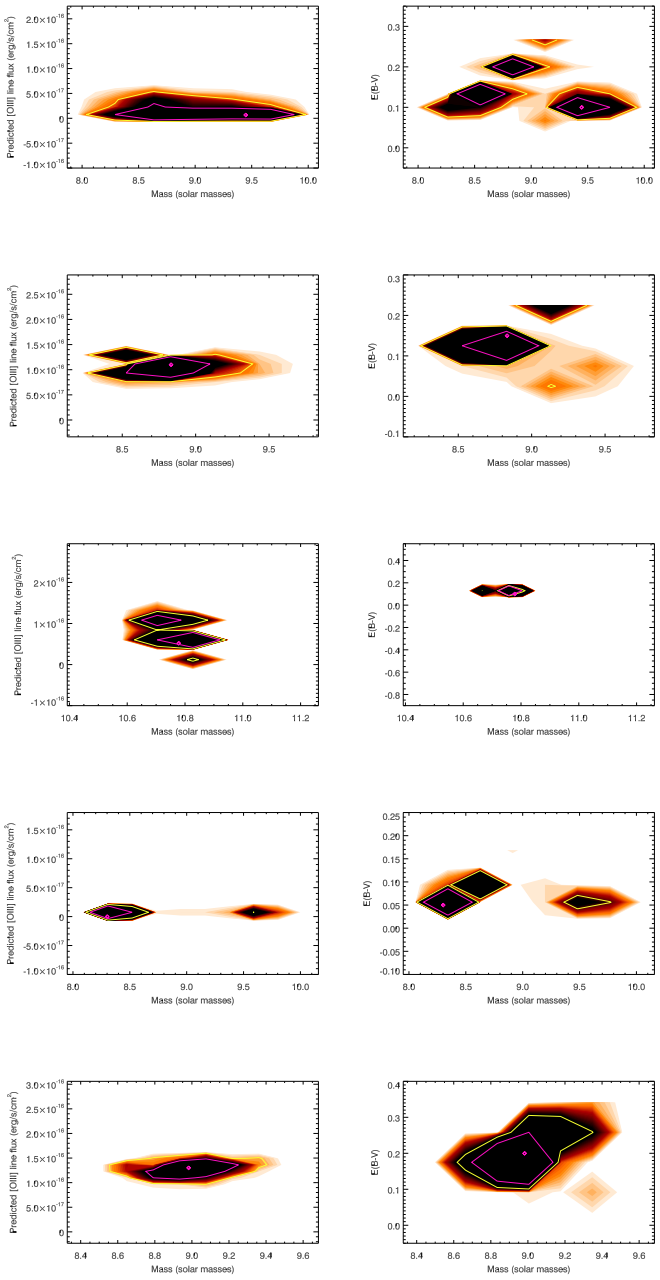

Figure B.4 Same as Figure B.1 for next 5 objects.

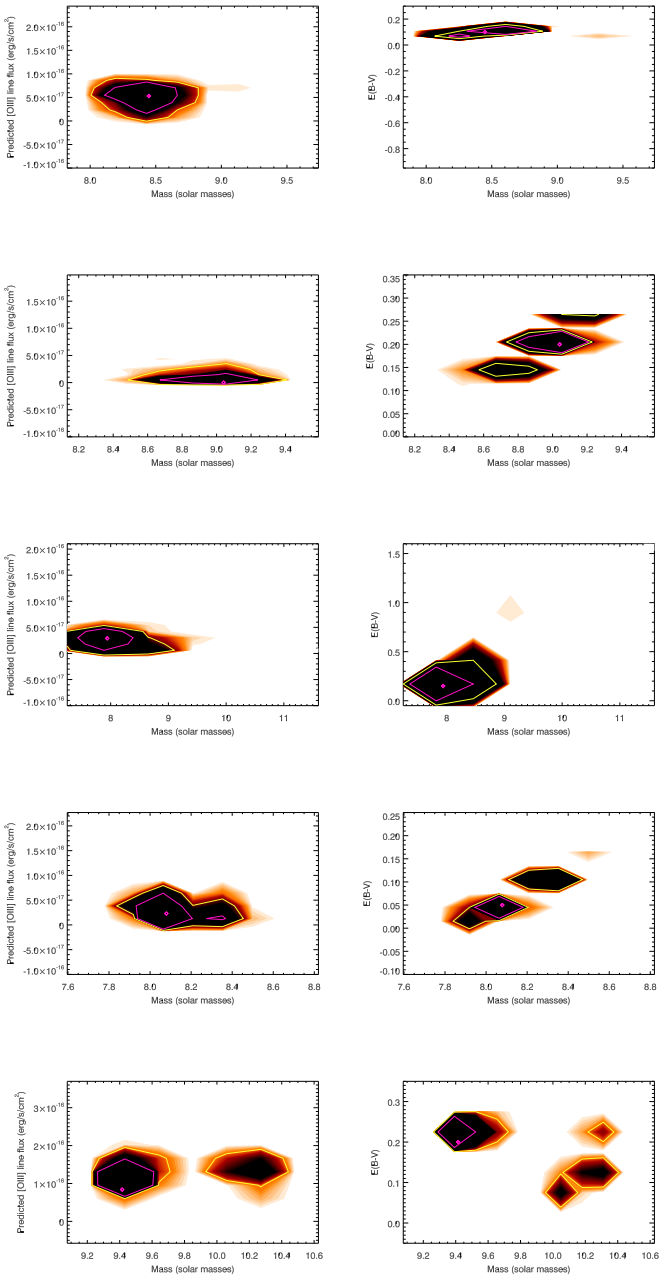

Figure B.5 Same as Figure B.1 for next 5 objects.

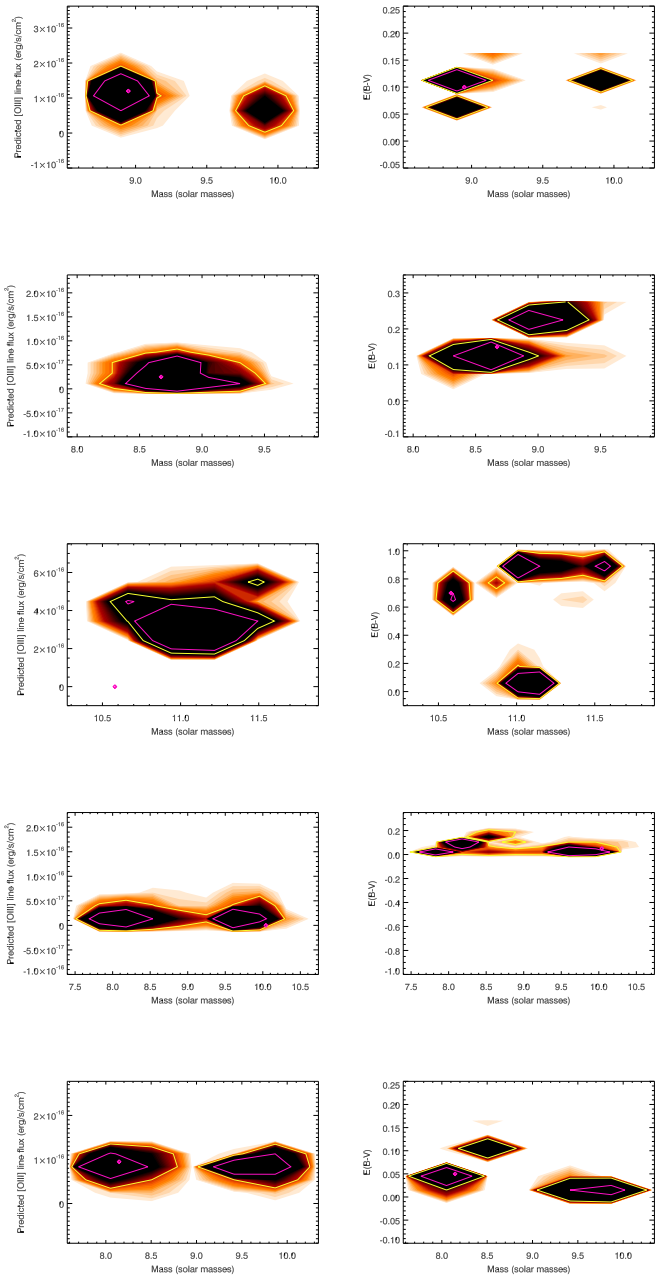

Figure B.6 Same as Figure B.1 for next 5 objects.

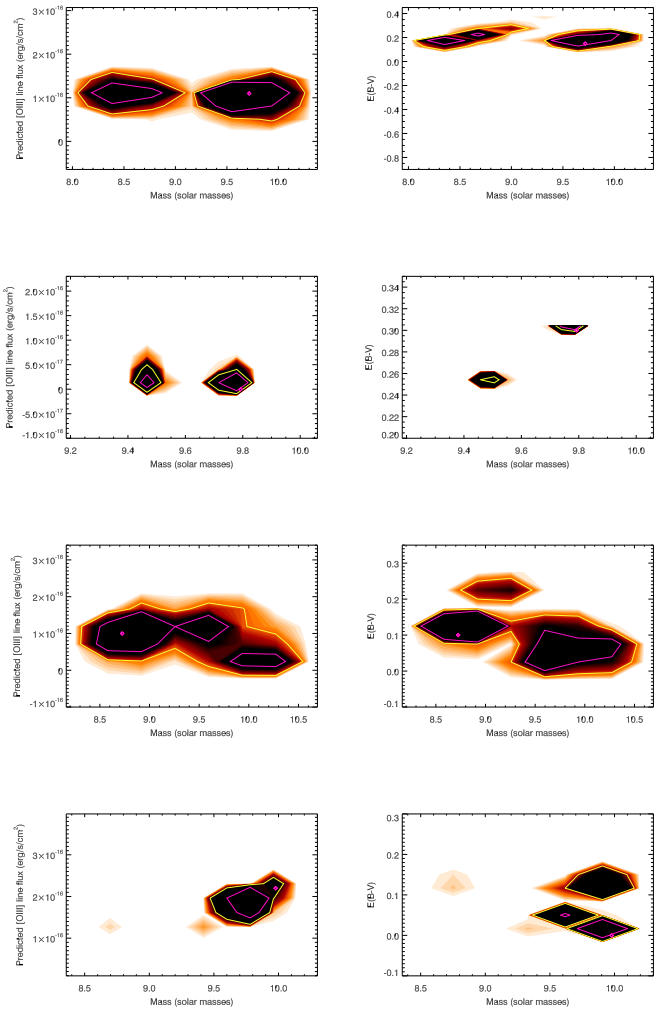

Figure B.7 Same as Figure B.1 for next 4 objects.